Aus dem
Institut für Tierpathologie
des Fachbereichs Veterinärmedizin
der Freien Universität Berlin
und dem
Max-Planck-Institut für molekulare Genetik

Analysis of the expression pattern and knock-out phenotype of Slit-like 2 (*Slitl2*) in the mouse

Inaugural-Dissertation
zur Erlangung des Grades eines
Doktors der Veterinärmedizin
an der
Freien Universität Berlin

vorgelegt von
Anja Michaela Mayer

Tierärztin aus
Mühldorf am Inn

Berlin 2009

Journal-Nr.: 3359

Gedruckt mit Genehmigung

des Fachbereichs Veterinärmedizin

der Freien Universität Berlin

Dekan:	Univ.-Prof. Dr. med. vet. Leo Brunnberg
Erster Gutachter:	Univ.-Prof. Dr. med. vet. Achim D. Gruber, Ph.D.
Zweiter Gutachter:	Univ.-Prof. Dr. Bernhard G. Herrmann
Dritter Gutachter:	Univ.-Prof. Dr. Michael Schmidt

Deskriptoren (nach CAB-Thesaurus): mice, laboratory animals, gene expression, genes, reporter [MeSH], membrane proteins, gene expression profiling [MeSH], mice, knockout [MeSH]

Tag der Promotion: 19.02.2010

Für meine Mutter,
durch die ich werden konnte, wer ich bin.

Und für Peter,
bei dem ich sein kann, wer ich bin.

Contents

Abbreviations

α-	anti-
aa	amino acid(s)
AP	alkaline phosphatase
BAC	bacterial artificial chromosome
bp	base pair(s)
BSA	bovine serum albumin
Cam	chloramphenicol
CD	cluster of differentiation
cDNA	complementary DNA
CMV	cytomegalovirus
cRNA	complementary RNA
DAPI	4',6-diamidino-2-phenylindole
ddH_2O	double-distilled H_2O
dig	digoxigenin
E	embryonic day
ES	embryonic stem
EtOH	ethanol
FBS	fetal bovine serum
FCS	fetal calf serum
g	gravity
het	heterozygous
hom	homozygous
GBM	glomerular basement membrane
GFB	glomerular filtration barrier
GFP	green fluorescent protein
h	hour(s)
H&E	hematoxylin and eosin
HEK	human embryonic kidney
Ig	immunoglobulin
IQR	interquartile range
Kan	kanamycin
kb	kilobase

kDa	kilodalton
KO	knock-out
LB	Luria Bertani
μCT	micro-computed tomography
MEFs	mouse primary embryonic fibroblasts
MetOH	methanol
MHC	major histocompatibility complex
min	minute(s)
neo	neomycin
OD	optical density
o/n	overnight
ORF	open reading frame
P	postnatal day
PAS	periodic acid-Schiff
PCR	polymerase chain reaction
PBS	phosphate-buffered saline
RBC	red blood cell(s)
rRNA	ribosomal RNA
RT	room temperature
RT-PCR	reverse transcription PCR
SD	standard deviation
SDS-PAGE	sodium dodecyl sulfate polyacrylamide gel electrophoresis
sec	second(s)
TCR	T-cell receptor
UTR	untranslated region
vol.	volume
VSMCs	vascular smooth muscle cells
v/v	volume/volume
WBC	white blood cell(s)
WISH	whole-mount *in situ* hybridization
wt	wild-type
w/v	weight/volume
YFP	yellow fluorescent protein

1 Introduction

1.1 Development of the mouse embryo

Mouse embryonic development takes 19 days on average. It begins with a single cell, namely the fertilized egg, or zygote. The zygote undergoes cleavage divisions to form blastomeres. At the 8-cell stage, the embryo has developed into a morula, and its cells start to compact, polarize, and form a blastocyst. Implantation of the blastocyst occurs around embryonic day 4.5 (E4.5), and by this stage, two distinct cell populations can be discriminated: the outer trophoblast cells and the inner cell mass (ICM). The latter comprises two cell layers, namely the hypoblast, also known as the primitive endoderm, and the epiblast. The embryo proper is formed exclusively from descendants of the epiblast. At the onset of the gastrulation process, the epiblast consists of approximately 800 cells [Snow and Bennett, 1978]. Gastrulation in the mouse embryo begins around E6.5 when the primitive streak at the future posterior end of the embryo arises. Cells from the continuous epiblast layer detach from their neighboring cells by a process known as epithelial-to-mesenchymal transition. Thus, the cells become motile and individually migrate through the streak [Burdsal et al., 1993]. One part of the ingressing cells constitutes an intermediate layer of embryonic mesoderm between the epiblast and the underlying hypoblast, while the other part gradually replaces the hypoblast cells, thereby forming the embryonic endoderm. As a result of gastrulation, the embryo becomes a trilaminar entity, with an outer layer of ectoderm, an intermediate mesoderm, and an inner layer of endoderm. In the mouse, the germ layers are initially arranged in an inverse manner with the ectoderm facing the inside and the endoderm facing the outer aspect of the U-shaped egg cylinder. Around E8.5, this inversion is reverted by the complex process of turning. The onset of organogenesis coincides with turning. During this phase, the germ layers begin to assemble the organ and tissue rudiments. Also, several transient structures emerge, e.g., the notochord, the branchial arches, and the somites. They ultimately contribute to the generation of functional organs or tissues in the adult. Distinct cell types derive from the different germ layers. The

nervous system, the epidermal cells of the skin, and most of the skeletal and connective tissue of the head, for example, arise from the ectoderm. The mesoderm is subdivided into various clusters that are organized in longitudinal stripes. The axial mesoderm along the midline of the embryo is flanked by paraxial mesoderm on both sides. The latter condenses to form somites, from which the axial skeleton, the connective tissue of the skin, and most muscles in the body are generated. The urogenital system is formed by the intermediate mesoderm, while the lateral plate mesoderm gives rise to tissues such as bones and cartilages of the limbs, the heart, and the vascular system. The endoderm, on the other hand, mainly generates the digestive tract including the liver and pancreas as well as the inner linings of the lungs. The end of organogenesis marks the beginning of the fetal period during which the organs grow and mature until gestation has reached full term. Figure 1.1 summarizes the most critical events during mouse development.

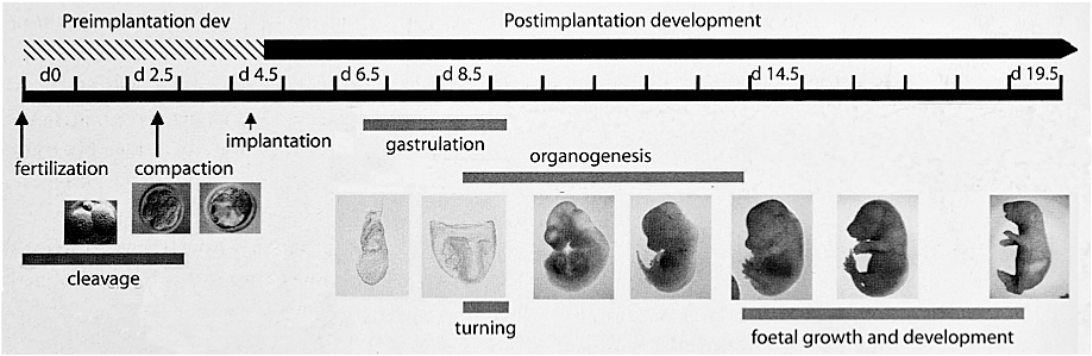

Figure 1.1 Overview of mouse development
Mouse embryonic development takes approximately 19 days. The pre- and postimplantation phases are indicated above the time line, critical events and processes are indicated below the time line. Modified after [Hedrich and Bullock, 2004]

1.2 Development of the mouse kidney

The kidney has been a classical model of organogenesis for over 50 years. Its development is characterized by three consecutive stages: the pronephros, the mesonephros, and the metanephros. While the former two are only transient structures, the latter persists as the functional kidney. The nephric duct arises from intermediate mesoderm around E8.0 of early mouse development. As it extends caudally, it induces the sequential formation of tubules in the adjacent mesenchyme. By the time the rudimentary pronephric tubules degenerate, a new array of tubules appears, namely the mesonephric tubules. In mice and rats, the mesonephros never functions as a working kidney. The nephric duct continues to elongate posteriorly, and by E10.5, the ureteric bud becomes evident at its medial aspect. The definitive kidney, the metanephros, is formed by two types of intermediate mesoderm: the ureteric bud and its surrounding metanephric mesenchyme (Figure 1.2 A). These two tissues reciprocally induce each other during this process. While the mesenchyme promotes growth and branching of the ureteric bud, the bud induces the conversion of metanephric mesenchyme into epithelium. Epithelial aggregates at the tips of the branching buds then transform into renal vesicles. The vesicles elongate into characteristic S-shaped bodies. The distal part of those bodies fuses with its inducing ureteric bud tip to generate a continuous lumen, and their proximal part is invaded by endothelial precursor cells (Figure 1.2 B). As development proceeds, mature nephrons are formed by both types of cells. Endothelial cells constitute capillary loops, whereas epithelial cells differentiate into podocytes, i.e., visceral epithelial cells, parietal epithelial cells lining the Bowman's capsule, and the tubular components (the proximal tubule, the loop of Henle, and the distal tubule). The distal tubules connect to the collecting duct, which are derived from the ureteric bud (Figure 1.2 C). To generate a mature kidney, this process is reiterated as newly forming branches of the ureteric bud induce the formation of new nephrons in the periphery of the developing organ, namely in the nephrogenic zone. In the mouse, nephrogenesis continues for about one week after birth [Davies and Bard, 1996]. The adult kidney is composed of two major compartments: the peripheral cortex and the central medulla. The collecting ducts reach from the cortex through the medullary region into the papilla, where they drain into the ureter. The nephrons, on the other hand, are located only in the cortical region (Figure 1.2 D).

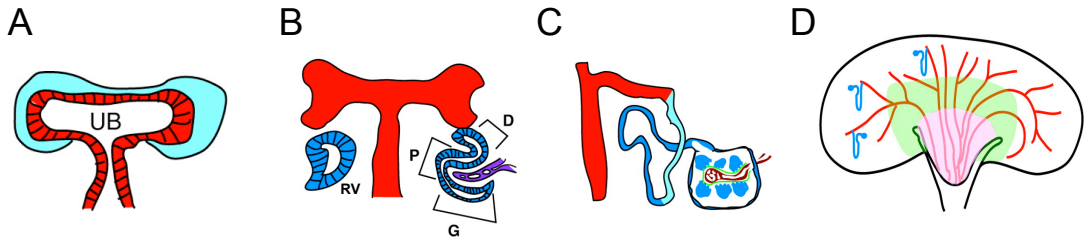

Figure 1.2 Schematic of kidney development
A. Cross section of an E11.5 mouse embryonic kidney at induction. Mesenchyme (blue) condenses around the two branches of the ureteric bud (UB, red). **B**. The renal vesicle (RV) undergoes segmentation to form the nephron, which consists of the glomerulus (G), the proximal tubule (P), the loop of Henle (not shown), and the distale tubule (D). The latter connects to the ureteric bud, which itself transforms into the collecting ducts. **C**. A mature nephron with capillary loops (red) inside the glomerulus and the glomerular basement membrane (green) between podocytes (blue) and the capillaries. The distal segment of the nephron (light blue) connects to the collecting duct (red). **D**. Cross section of a mature kidney. Nephrons are located in the cortex (unshaded), whereas collecting ducts extend into the medulla (green) and medullary papilla (pink). Modified after [Quaggin and Kreidberg, 2008]

1.3 Glomeruli at a glance

The nephrons are the basic functional units of the kidney. Each nephron comprises a renal corpuscle and a renal tubule. The renal corpuscle consists of a glomerulus and a surrounding Bowman's capsule. In the corpuscle, blood plasma is filtered to produce the primary urine. Blood enters the glomeruli through arteries that branch inside the organ to form capillary tufts, i.e., tiny looping blood vessels. The glomerular filtration barrier, which separates the blood stream from the urinary space, is composed of three distinct layers: the endothelial cells, the glomerular basement membrane, and the podocyte cells (Figure 1.3 A). The innermost layer of endothelial cells displays a specialized, fenestrated morphology. Podocytes, on the other hand, are highly modified epithelial cells that terminate in foot processes. The basal aspects of these processes intertwine on the surface of the glomerular basement membrane, thereby forming cell-cell junctions known as slit diaphragms. Thus, slit-like openings are found on both sides of the intervening basement membrane, which is composed of the fused basal laminae of the other two layers (Figure 1.3 B). The glomerular filtration barrier functions both as a size- and a charge-selective filter. The capillary pores allow passage

of all plasma components but not blood cells, while the basement membrane retains all but the smallest proteins. In addition, other macromolecular anions, i.e., most plasma proteins, are repelled by the negatively charged glycoproteins of the basement membrane. Ultimately, the thin membranes constituting the slit diaphragms between adjacent foot processes can block the passage of proteins.

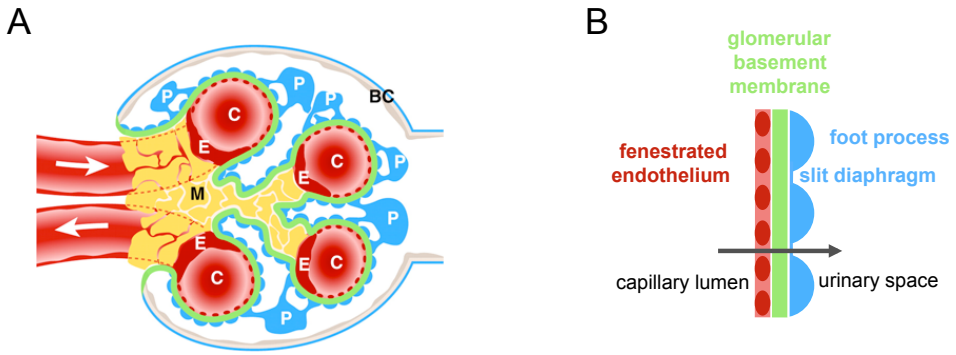

Figure 1.3 Schematic of a mature glomerulus and the glomerular filtration barrier
A. The four major cell types in the glomerulus are the parietal epithelial cells (gray) lining the Bowman's capsule (BC), podocytes (P, blue), mesangial cells (M, yellow), and endothelial cells (E, red) of the capillary loops (C). Modified after [Quaggin and Kreidberg, 2008] **B**. The glomerular filtration barrier is composed of three layers: the fenestrated endothelial cells, the glomerular basement membrane, and the slit diaphragms between adjacent foot processes of the podocytes. Arrow indicates filtration direction from the capillary lumen to the urinary space.

Proteins that are 'trapped' in the filtration membrane are degraded by mesangial cells. Mesangial cells are mostly found at the stalk of the capillary tuft. These cells are a specialized type of smooth muscle cells, which are involved in maintaining the structure of the glomerular tuft as well as in the response of the glomerular vasculature to various physical stimuli [Schlondorff, 1987] [Yamanaka, 1988]. Once the primary urine is produced, some substances including glucose and electrolytes are reabsorbed, whereas others like urea and creatinine are secreted while passing through the different parts of the renal tubular system, namely the proximal tubule, the loop of Henle, and the distal tubule. By the time the urine reaches the collecting duct, it is usually dilute. Therefore, water is reabsorbed in this part, and concentrated urine is excreted.

1.4 The Slit genes

The Slit gene was first described in Drosophila in 1988 [Rothberg et al., 1988], and only a decade later, three vertebrate homologs were identified [Itoh et al., 1998] [Holmes et al., 1998] [Nakayama et al., 1998] [Yuan et al., 1999]. The vertebrate Slit proteins are large secreted molecules consisting of a signal peptide, four leucine-rich repeat (LRR) regions, nine epidermal growth factor (EGF) repeats, which are interrupted by a laminin G domain, and a cysteine-rich carboxy-terminus [Brose et al., 1999]. It has been demonstrated that the Slit proteins signal through the roundabout (Robo) receptor family of proteins [Kidd et al., 1999].

The Slit/Robo system has been studied most extensively in the context of axon guidance. In the developing vertebrate spinal cord, all three Slit genes are expressed in the floor plate at the ventral midline, while three of the four transmembrane Robo receptors, namely *Robo1*, *Robo2*, and *Rig-1* (*Robo3*), are expressed on the surface of neuronal axons [Yuan et al., 1999] [Holmes et al., 1998] [Brose et al., 1999] [Erskine et al., 2000]. Growing axons either remain on one side of the spinal cord to project ipsilaterally or cross the midline and project contralaterally. The decision to cross or not to cross is largely governed by Slits and their Robo receptors. Crossing, i.e., commissural axons initially express *Robo1* and are thereby repelled from the midline by the Slit proteins (Figure 1.4 A). Rig-1, a divergent member of the Robo family, transiently blocks Robo1 function. Thus, the axons are no longer sensitive to the repulsive signal of the Slits and enter the midline (Figure 1.4 B). Robo1 function is reactivated only after crossing of the midline, which allows the Slits to force the axons out of the midline and prevent them from recrossing (Figure 1.4 C) [Long et al., 2004] [Sabatier et al., 2004] [Mambetisaeva et al., 2005]. This repulsive signal is mediated by slit/robo GTPase-activating proteins (srGAPs), which ultimately leads to a decreased cytoskeletal actin polymerization, causing the cells to migrate away from areas of high Slit concentration [Wong et al., 2001].

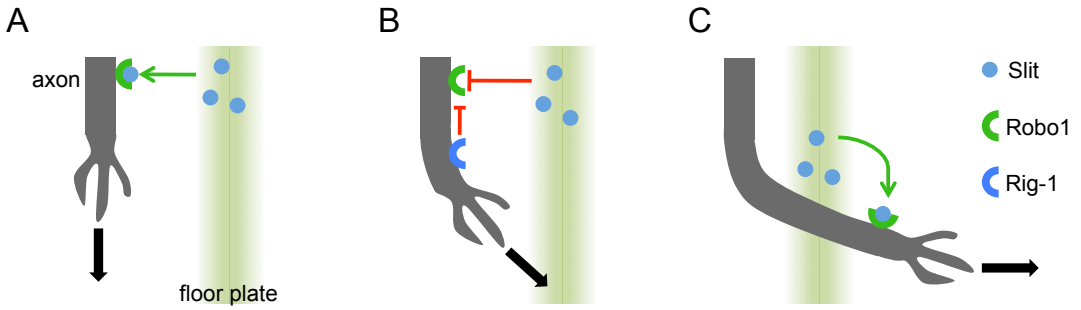

Figure 1.4 Slit/Robo system of regulating midline crossing of axons
A. Growing axons initially express *Robo1* and are thus prevented from crossing the floor plate at the ventral midline of the nervous system by Slit. **B**. *Rig-1* expression then blocks Robo1 function, allowing the axons to enter the midline. **C**. After crossing the floor plate, *Robo1* is reexpressed, forcing the axons away from the midline by the repellent function of Slit. Adapted from [Gilbert, 2006]

In *Slit1*- and *Slit2*-single- as well as in *Slit1*/*Slit2*-double-mutant mice, no obvious defects are observed in commissural axon guidance within the developing spinal cord despite severe abnormalities in the formation of several major forebrain tracts [Bagri et al., 2002] [Plump et al., 2002]. This observation was attributed to the fact that expression of *Slit3* in the floor plate of the spinal cord possibly compensated the loss of the other two Slit proteins, while its expression in the affected forebrain regions was reported to be weak or absent. *Slit1*/*Slit2*/*Slit3*-triple mutants confirmed this assumption. In these mice, the commissural axons appear highly disorganized and defasciculated at the floor plate [Long et al., 2004]. *Slit2*- as well as combined *Slit1*/*Slit2*-deficient animals show early postnatal lethality, whereas *Slit1*-mutant mice seem grossly normal [Plump et al., 2002]. Conversely, *Slit3*-deficiency results in partial embryonic lethality. The surviving mutants display various defects, including diaphragmatic herniation as well as heart and kidney defects [Liu et al., 2003].

In addition to the well-characterized role of Slit proteins in axon repulsion, a growing body of evidence shows that they also regulate the migration of various other cell types, e.g., muscle precursor cells [Kramer et al., 2001] and chemotactic leukocytes [Wu et al., 2001].

Although first discovered and described as mediators of axon guidance, Slit genes have a more widespread role during development and are involved in the formation of several organs, namely the lung and the kidney. The mammalian lung develops through complex interactions between endoderm and surrounding mesenchyme with the differentiation of the developing epithelial respiratory

tube being determined by the regional specificity of the mesenchyme. Expression of *Slit2* and *Slit3* in conjunction with *Robo1* and *Robo2* in specific subsets of embryonic and fetal lung mesenchyme implicates a function during pulmonary development [Anselmo et al., 2003] [Greenberg et al., 2004]. In the kidney, expression of all three members of the Slit family of proteins has been described in confined regions of the developing metanephric mesenchyme and ureteric bud tree [Piper et al., 2000] [Stuart et al., 2003]. In *Slit2*-deficient embryos, several defects are observed during kidney formation. By E18.5, the mutants display grossly dilated collecting ducts and ureters. In addition, the site where new nephrons are generated is no longer restricted to the nephrogenic zone. Instead, nephrogenesis is also observed in the medullary region. To analyze the nature of these abnormalities, embryos were examined at the onset of renal development. In E11.5 mutant embryos, supernumerary ureteric buds had emerged from the nephric duct. By E14.5, most of these buds had invaded the metanephric mesenchyme, thereby inducing the formation of additional kidneys. These defects were attributed to inappropriate maintenance of glial cell line-derived neurotrophic factor (*Gdnf*) expression. Its expression is normally restricted to the posterior nephrogenic mesenchyme where it induces the formation of a single ureteric bud [Hellmich et al., 1996] [Suvanto et al., 1996]. In the *Slit2* mutants, however, its expression domain is extended into the anterior nephrogenic mesenchyme, causing the above described defects [Grieshammer et al., 2004].

During the recent years, studies have accumulated that suggest a role for the human Slit genes in tumorigenesis. *SLIT2* is known to be silenced by promoter hypermethylation in lung, breast, and colorectal cancer, and its ectopic reexpression in the respective cancer cell lines suppressed their ability to form colonies [Dallol et al., 2002] [Dallol et al., 2003]. Epigenetic inactivation of *SLIT1*, *SLIT2*, and *SLIT3* was also shown to be an early event during progression of cervical cancer [Narayan et al., 2006]. Decreased *SLIT2* expression has been reported in human esophageal squamous cell carcinomas. This study implicated a *SLIT2*-mediated regulation of apoptosis and cell cycle progression via downregulation of molecules involved in both processes [Kim et al., 2008]. Other experiments demonstrated inhibition of glioma cell invasiveness by *SLIT2* through attenuation of cell migration [Yiin et al., 2009].

1.5 The Slit-like 2 gene

The murine Slit-like 2 gene (*Slitl2*; GenBank accession AJ458938) was first identified in 2002. It is located on the forward strand of chromosome 16 at band A1 and spans over 10,805 bp. The locus consists of two exons which are interrupted by a large intronic sequence of 8,033 bp. The smaller first exon of 189 bp encodes the 5' untranslated region (5' UTR) along with the first 9 bp of the larger second exon (2,583 bp). The 3' UTR is encoded by 552 bp of the second exon (Figure 1.5 A). The open reading frame (ORF) on exon 2 translates into a protein of 673 amino acids (aa) with a calculated molecular weight of 72 kDa. *Slitl2* is a highly conserved gene. Orthologs have been identified in numerous other species, including rat (Rattus norvegicus), zebrafish (Danio rerio), chicken (Gallus gallus), and man (Homo sapiens). Alignment of the mouse Slitl2 full length sequence reveals an overall identity of more than 95% and 83% at the amino acid level with the rat and the human homolog, respectively. The Slitl2 protein is a typical single-pass type I transmembrane protein. Its extracellular amino-terminus contains a putative hydrophobic signal peptide, one leucine-rich repeat (LRR) region comprising ten leucine-rich repeats flanked by an amino- and a carboxy-terminal LRR motif, one epidermal growth factor (EGF) repeat, and a fibronectin type III (FNIII) domain. These motifs are followed by a highly hydrophobic stretch of amino acids predicting a transmembrane domain (TM). The short intracellular carboxy-terminus of approximately 80 aa shows no similarity to any known sequences (Figure 1.5 B). The combination of LRR regions and EGF domains is conserved within the Slit family of proteins. Based on this shared feature, *Slitl2* was designated its name. In contrast to the secreted Slit proteins, however, Slitl2 is a transmembrane protein as was confirmed by immunofluorescence microscopy (Figure 1.5 C).

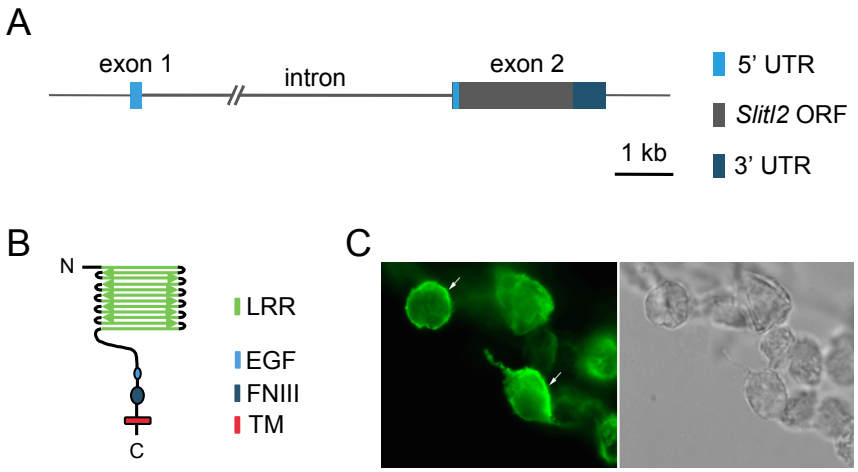

Figure 1.5 The murine *Slitl2* gene and Slitl2 protein
A. The *Slitl2* locus consists of two exons. The *Slitl2* open reading frame (ORF) is located entirely on exon 2. **B**. The Slitl2 protein consists of an amino-terminal signal peptide (N), a leucine-rich repeat region (LRR), an epidermal growth factor repeat (EGF), a fibronectin type III domain (FNIII), a transmembrane domain (TM), and a short intracellular carboxy-terminus (C). **C**. Hemagglutinin-tagged Slitl2 (Slitl2-HA, arrows) can be localized to the cell membrane of HEK293T cells by fluorescence microscopy using an anti-HA antibody (left). Corresponding bright field image (right). (Image courtesy of Dr. Heinrich Schrewe)

So far, only two reports have been puplished on Slit-like 2. The first report describes the zebrafish *slitl2* gene encoding for a protein of 688 aa with a calculated molecular weight of 75.5 kDa. Analysis of the protein structure predicted an amino-terminal signal peptide, LRR and EGF repeats, i.e., a Slit domain, and a cripto growth factor domain. Interestingly, no transmembrane domain was found. Whole-mount *in situ* hybridization on zebrafish embryos revealed expression in midline structures of the central nervous system as well as in the vascular system, suggesting that slitl2 might be essential during their development [Chen et al., 2005].

The second report introduces the human homolog of the Slit-like 2 gene, which is known as vasorin (*VASN*). It encodes a protein of 673 aa and shares all the features of the murine protein. Immunofluorescence analysis corroborated its transmembrane localization, and Northern blot analysis detected strong expression in the aorta and moderate expression in the kidney and placenta. *In situ* hybridization demonstrated vasorin expression in interstitial cells of the kidney and in arterial vascular smooth muscle cells (VSMCs). When in culture, VSMCs convert from a contractile, differentiated into a synthetic, dedifferentiated phenotype,

and semiquantitative reverse transcription (RT)-PCR showed that *VASN* was significantly downregulated in cultured VSMCs. Furthermore, surface plasmon resonance analysis revealed specific and significant binding of transforming growth factor-β1 (TGF-β1) to vasorin's extracellular domain. *In vitro* functional analyses performed on vasorin-expressing cells demonstrated inhibition of TGF-β1 downstream signaling. This effect was abrogated by concomitant stimulation with a constitutively active TGF-β1 receptor, suggesting that VASN inhibits TGF-β-signaling at the extracellular and/or cell surface level. *In vivo* functions of vasorin were investigated using a rat arterial balloon-injury model. Following mechanical vascular injury, vasorin expression was downregulated, while *TGF-β1* expression was found to be upregulated. This upregulation is known to promote vessel repair by formation of neointima. Adenovirus-mediated restoration of vasorin expression significantly reduced neointimal formation, and this inhibitory effect was attributed to a modulation of TGF-β1 downstream signaling in the vessel wall [Ikeda et al., 2004].

1.6 TGF-β1 in development and disease

Transforming growth factor-β1 (TGF-β1) is one of over 30 structurally related members of the TGF-β superfamily of proteins. In addition to the eponymous TGF-β family, the superfamily includes the bone morphogenetic proteins (BMPs), the inhibin/activin family, and numerous other proteins, e.g., growth and differentiation factors (GDFs) and glial cell line-derived neurotrophic factor (GDNF). Three different TGF-β isoforms have been identified in mammals (TGF-β1, 2, and 3). TGF-β is synthesized as a precursor which is cleaved intracellularly to form a disulfide-bonded dimer. The mature TGF-β peptide at the carboxy-terminus remains associated to the amino-terminal TGF-β latency-associated protein (LAP) prodomain via non-covalent bonds. While this so-called small latent complex (SLC) is secreted very slowly, covalent binding to latent TGF-β binding proteins (LTBPs) enhances the secretion of TGF-β in a large latent complex (LLC) (Figure 1.6 A). LTBPs rapidly deposit latent TGF-β in the extracellular matrix, and activation of TGF-β requires its cleavage from the LAP prodomain. Various mechanisms, including proteolysis and acidic microenvironment conditions, have been proposed to mediate this activation *in vivo* (reviewed in [Saharinen et al., 1999]). Upon activation, TGF-β initiates signaling by interacting with two pairs of receptor serine/threonine kinases known as type I and type II receptors.

Binding of TGF-β to the type II receptors induces complex formation with and subsequent phosphorylation of the type I receptors. The activated type I receptors, in turn, transduce the signal intracellularly. TGF-β type III receptors (e.g., betaglycan or endoglin) function as coreceptors for some ligand–receptor interactions, thereby modulating TGF-β signaling. The best understood intracellular downstream signaling pathway involves phosphorylation of the receptor-activated Smad proteins (Smad2, Smad3). Upon phosphorylation, these molecules form a complex with the common mediator Smad (Smad4) and translocate to the nucleus to regulate transcription of target genes (Figure 1.6 B) (reviewed in [Massague and Gomis, 2006]).

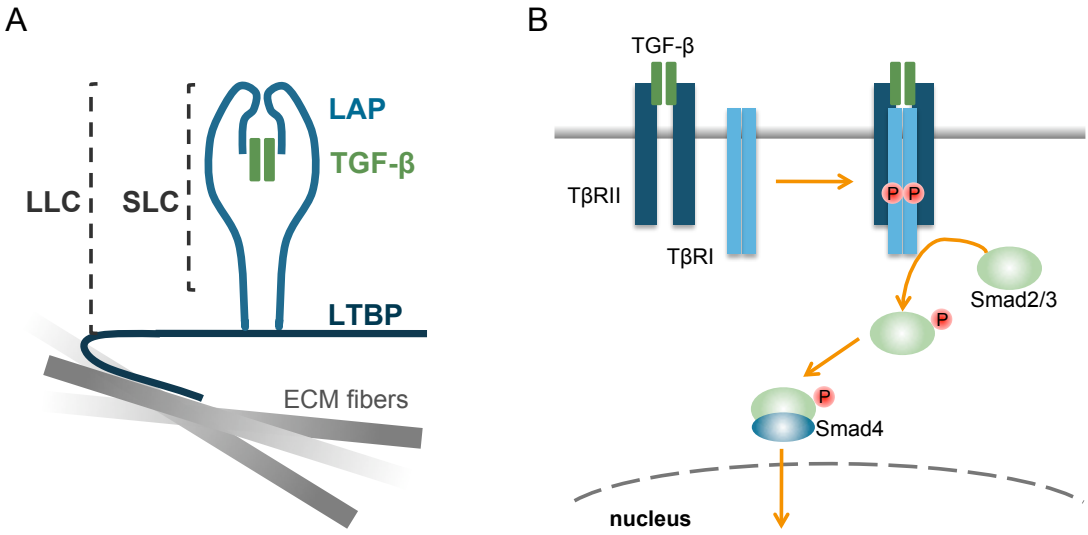

Figure 1.6 Schematic of the TGF-β latent complex and TGF-β signaling
A. The mature TGF-β dimer (green) remains associated to the amino-terminal TGF-β latency-associated protein (LAP) prodomain in the small latent complex (SLC). It is secreted as large latent complex (LLC) in conjunction with latent TGF-β binding proteins (LTBP), which deposit it in the extracellular matrix (ECM). Adapted from [Saharinen et al., 1999] **B**. The released TGF-β dimer binds to the type II receptors (TβRII), which induces complex formation and phosphorylation of the type I receptors (TβRI), leading to phosphorylation of the receptor-activated Smads (Smad2/Smad3). These form a complex with the common mediator Smad (Smad4) and translocate to the nucleus to regulate transcription of target genes. Adapted from [Gilbert, 2006]

TGF-β regulates a myriad of different and often diverse cellular processes. It is, for example, known to induce cell cycle arrest in mouse primary embryonic fibroblasts [Datto et al., 1999], while it promotes proliferation of fibroblasts isolated from adult tissue [Dkhissi et al., 1999] [Strutz et al., 2001] [Pelaia et al., 2007]. It also induces transformation of these cells into spindle-shaped myofibroblasts. This process is associated with a reorganization of the cytoskeleton and an upregulation of α-smooth muscle actin (α-SMA). Myofibroblasts appear to be essential in the production of extracellular matrix *in vivo* and are found in fibrotic disease conditions [Kuhn and McDonald, 1991] [Qi et al., 2006]. Overexpression of TGF-β leads to severe lung fibrosis [Sime et al., 1997] [Lee et al., 2001], and attenuation of TGF-β-signaling has been shown to prevent skin, lung, and liver fibrosis [McCormick et al., 1999] [George et al., 1999], underscoring the therapeutic potential of this pathway.

TGF-β also exerts paradoxical functions in cancer. It acts as tumor suppressor in the premalignant state by repressing growth-promoting transcription factors and activating cell cycle inhibitors in epithelial cell lines [Moses et al., 1991] [Datto et al., 1995] [Reynisdottir et al., 1995]. During cancer development, however, tumors producing high levels of TGF-β may evade immune surveillance by exploiting its potent immunosuppressive effects [Torre-Amione et al., 1990] [Gorelik and Flavell, 2001]. Furthermore, TGF-β induces epithelial-mesenchymal transition of cancer cells, whereby the cells acquire motility and invasive properties needed for dissemination [Oft et al., 2002] [Janda et al., 2002].

Transforming growth factor-β1 (*Tgfb1*)-deficiency in mice leads to intrauterine lethality of over 50% caused by defective hematopoiesis and vasculogenesis of extraembryonic tissues [Dickson et al., 1995]. Live-born mutant pups are initially indistinguishable from their wild-type littermates. Approximately two weeks after birth, however, the mutants develop a severe wasting syndrome and die due to massive inflammatory infiltration of multiple organs including the heart, lung, liver, and brain [Shull et al., 1992] [Kulkarni et al., 1993]. Blood samples revealed a significant increase in monocytes and immature neutrophils in the mutant animals [Shull et al., 1992], and expression of both class I and class II major histocompatibility complex (MHC) molecules was found to be elevated in the affected organs prior to inflammatory cell infiltration, suggesting altered antigen presentation as underlying cause for the multifocal inflammatory disease [Geiser et al., 1993]. This inappropriate immune response commences with leukocyte adhesion to venous endothelial walls followed by tissue infiltration [Kulkarni et al., 1995].

The autoimmune nature of the inflammatory reaction observed in *Tgfb1* mutants was demonstrated by increased levels of circulating autoantibodies and immune complex deposition in renal glomeruli [Yaswen et al., 1996]. These lesions are absent in *Tgfb1*/MHC II double-deficient animals, corroborating the assumption that autoimmunity in the *Tgfb1*-deficient mice is indeed provoked by abnormal antigen presentation [Letterio et al., 1996]. Analyses on lymphoid organs of *Tgfb1* mutants showed that T and B lymphocyte development is evidently unaffected during embryogenesis, whereas symptomatic animals display a reduction in immature T and B cells with a concomitant increase in mature lymphocytes [Christ et al., 1994] [Kulkarni et al., 1995] [Boivin et al., 1995].

Equally, overexpression of TGF-β1 in transgenic mice causes a variety of lesions. Aberrant expression in hepatocytes induces liver fibrosis via increased production of collagen I. In addition, extrahepatic defects including glomerulosclerosis and renal fibrosis, arteritis, and myocarditis are observed due to elevated serum levels of TGF-β1 [Sanderson et al., 1995] [Kopp et al., 1996]. Excess TGF-β1 has also been reported to perturb normal tissue homeostasis in the central nervous system [Wyss-Coray et al., 1995] [Galbreath et al., 1995], the skin [Fowlis et al., 1996], and the mammary gland [Silberstein et al., 1992].

1.7 Objectives

The high degree of sequence similarity between the human and the mouse orthologs of the Slit-like 2 protein suggests an evolutionary conserved function in these two species. Thus, elucidating the function of Slit-like 2 (*Slitl2*) in the mouse might help to understand human development and disease. This thesis aimed at providing first information about the function of the murine *Slitl2* protein. Therefore, a detailed expression pattern was compiled by describing endogenous *Slitl2* expression as well as reporter gene expression in *Slitl2-LacZ* knock-in and *Slitl2-Venus* transgenic mice. In addition, *Slitl2*-deficient mice were generated and extensively characterized. With the comprehensive results presented here, this thesis has laid the groundwork for future studies.

2 Materials and methods

2.1 Mouse strains and animal husbandry

The mouse strains used for this study were all purchased from the Harlan Laboratories (Harlan Winkelmann GmbH, Borchen, Germany). The outbred strain CD-1® was derived from Swiss-Webster mice at the beginning of the 20th century, from which a stock was established at the Institute for Cancer Research (ICR), Philadelphia, PA (USA). Offspring were transferred to the Charles River Breeding Laboratories, Wilmington, MA (USA). The Harlan Sprague Dawley, Inc. (Hsd) obtained a breeding stock from the Charles River Breeding Laboratories (*Hsd:ICR(CD-1®)*). The outbred NMRI strain was derived from Swiss mice and established at the US Naval Medical Research Institute (NMRI). They were obtained by the Federal Research Institute for Virus Diseases of Animals in Tübingen (Germany) in 1955 and went to the Central Institute for Laboratory Breeding, Hannover (Germany) in 1958, from where Harlan UK obtained a stock in 1994 (*HsdHan:NMRI*). The strain 129 was originally derived from a cross of coat color stocks and a chinchilla stock at the beginning of the 20th century. A stock was obtained by the Harlan Laboratories from the Jackson Laboratory, Bar Harbor, ME (USA). The Harlan inbred strain represents a substrain of 129. 'S' refers to the origin from a congenic strain made by outcrossing the *steel* mutation, the number following the letter distinguishes the different 129 parental strains within the lineage, and 'Sv' indicates the name of the Stevens lab (*129S2/SvHsd*). The strain C57BL is the most widely used inbred strain. It was generated in 1921, and strain 6 (C57BL/6) was separated from strain 10. The C57BL/6 strain was obtained from the Jackson Laboratory (J) by Harlan UK, formerly OLAC (Ola), and later went to Harlan Netherlands. The strain purchased from Harlan Sprague Dawley, Inc. is therefore referred to as *C57BL/6JOlaHsd*.

The mice were housed under specific pathogen free (SPF) conditions at the animal facility of the Max Planck Institute for Molecular Genetics, Berlin, Germany. They were kept on a 12 h/12 h light/dark cycle at 22 °C with a relative humidity of 55±10%. A pelleted, irradiated diet (ssniff M-Z®, Soest, Germany)

containing 22% raw protein, 4.5% raw fat, 3.9% raw fiber, and 6.8% raw ashes and distilled water were provided ad libitum. All experimental work was approved by the Berlin State Office for Safety at Work, Health Protection and Technical Safety (Landesamt für Arbeitsschutz, Gesundheitsschutz und technische Sicherheit, LAGetSi; now Berlin State Office of Health and Social Affairs, LAGeSo) under the project number G 0248/03 (now G 0368/08) with a special amendment for the generation of genetically modified mice for the analysis of the function of *Slitl2*. All experiments were carried out in accordance with the German Animal Welfare Act (Tierschutzgesetz, TSchG).

2.2 Generation of *Slitl2*-mutant mouse lines

2.2.1 Constructs

2.2.1.1 *Slitl2* knock-out plasmid

The plasmid used for the generation of the *Slitl2*$^{floxed\text{-}neo}$ allele was provided by Dr. Heinrich Schrewe (Institute for Medical Genetics, Charité University Medicine, Berlin, Germany). It is described in more detail under subsection 3.2.1. Prior to electroporation into ES cells, 40 μg of the plasmid were linearized o/n at 37 °C with 4 μl *Nru*I (12 U/μl; Promega) and 15 μl Buffer B (Roche) in a total volume of 150 μl. In order to purify the linearized plasmid DNA the next day, it was subjected to phenol/chloroform extraction as follows: 1 vol. of 1:1 phenol:chloroform solution was added, and the contents were mixed. The sample was transferred to a Phase Lock Gel Heavy™ tube (Eppendorf) and centrifuged at 16,100 × g for 1 min. The upper phase was transferred to a standard tube, and the plasmid DNA was precipitated by adding 0.1 vol. 3 M sodium acetate pH 5.2 and 2.5 vol. cold 100% EtOH. The sample was incubated at -70 °C for 10 min before centrifugation at 16,100 × g for 10 min at 4 °C. The supernatant was removed, 200 μl cold 70% EtOH were added, and the sample was briefly vortexed before centrifuging it again as above. The supernatant was removed, the pellet was air-dried in a laminar flow hood and dissolved in 20 μl PBS. 1 μl was taken off to verify the linearization on a 1% (w/v) agarose gel as described under subsection 2.2.5. The remaining sample was stored at -20 °C until further use.

2.2.1.2 *Slitl2-LacZ* knock-in plasmid

The plasmid used for the generation of the *Slitl2*$^{LacZ\text{-}neo}$ allele was generated by Manuela Scholze (Institute for Medical Genetics, Charité University Medicine, Berlin, Germany) and is described in more detail under subsubsection 3.1.2.1. It was linearized, extracted, and precipitated as above (subsubsection 2.2.1.1).

2.2.1.3 Generation of the *Slitl2-Venus* BAC construct by recombineering

All procedures for recombineering followed the protocols provided by the National Cancer Institute (NCI-Frederick) described at http://recombineering.ncifcrf.gov/.

Introduction of the *Slitl2* BAC clone into SW105 cells For the generation of the *Slitl2-Venus* construct, a bacterial artificial chromosome (BAC) clone was selected that contained the complete *Slitl2* locus flanked by approximately 115 kb and 80 kb of its native genomic environment at its 5' and 3' end, respectively (NCBI Clone ID RPCI-23-224H7). This 205 kb-long fragment had been isolated from female C57BL/6J mouse genomic DNA and was cloned into the pBACe3.6 vector (GenBank accession U80929), which confers chloramphenicol resistance. The BAC clone was isolated from E. coli DH10B cells and electroporated into SW105 bacteria by Manuela Scholze (Institute for Medical Genetics, Charité University Medicine, Berlin, Germany). This bacterial strain contains a defective λ prophage inserted into the bacterial genome which encodes the recombination proteins, namely *exo*, *bet*, and *gam*. *exo* is a 5'-3' exonuclease that creates single-stranded overhangs on introduced linear DNA, i.e., the targeting construct, *bet* protects these overhangs, and *gam* prevents degradation of linear DNA. Their expression is driven by a promoter that is repressed by a temperature-sensitive repressor at 32 °C and derepressed at 42 °C. After a brief heat-shock at 42 °C, a sufficient amount of recombination proteins is produced. Linear DNA with sufficient homology in the 5' and 3' ends to a target DNA molecule already present in the bacteria can be introduced into heat-shocked and electrocompetent bacteria using electroporation. The introduced DNA is modified by *exo* and *bet* and undergoes homologous recombination with the target molecule [Warming et al., 2005].

Generation of the BAC targeting fragment A plasmid harboring the Venus coding sequence, which encodes a variant of the yellow fluorescent protein (YFP) with enhanced maturation and brightness [Rekas et al., 2002], in addition to an *FRT*-flanked neomycin (neo) selection cassette was used as template for the generation of the BAC targeting fragment. The neo gene is expressed both from a prokaryotic promoter (EM7) and a eukaryotic promoter (phosphoglycerate kinase, PGK). This plasmid was a modified version of the PL451 plasmid [Liu et al., 2003]. Chimeric primers were designed that allowed for amplification of the Venus-neo insert along with *Slitl2* homology arms on both ends. The primers each comprised a 69 bp-long sequence homologous to *Slitl2* at their 5' end and a shorter sequence homologous to the template plasmid at their 3' end (Table 2.1). The homology regions of the forward and the reverse primer corresponded to the 3' region of the *Slitl2* intronic sequence and the 5' region of exon 2, respectively. The primers were ordered from MWG and adjusted to a final concentration of 10 μM with ddH_2O prior to use.

Primer	**Sequence (5'→3')**
Forward	CTTCTCTGGCTTCCTGATGTGTCTGCCCTCAGCCCTGACTCATA AGCTCTTTGCTCTTAGGGACAGAAGccaccatggtgagcaagggcg
Reverse	CCCTGTACTCCAGACCCCAGGAGCACCAGAAGCAACAACAGGAG AGGTGGCAGGCAGCTCCTGGAGTGCgttatattatgtacctgactgatg

Table 2.1 Chimeric primers for amplification of the Venus-neo targeting fragment
Capital letters represent homology regions to *Slitl2*, small letters represent homology regions to the template plasmid.

The chimeric Venus-neo fragment with a total fragment size of 2,737 bp was amplified with the Expand Long Template PCR System (Roche). A 50 μl reaction was set up as follows: 5 μl 10×-concentrated Expand Long Template Buffer 2, 2.5 μl dNTPs (10 mM), 1.5 μl forward primer (10 μM), 1.5 μl reverse primer (10 μM), 0.75 μl Expand Long Template Enzyme Mix, 37.75 μl ddH_2O, 1 μl template plasmid (50 ng/μl). The reaction was performed according to the following program on an MJ Research PTC-200 Thermal Cycler:

Step	Temperature	Time
1. Initial denaturation	94 °C	2 min
2. Denaturation	94 °C	30 sec
3. Annealing	60 °C	30 sec
4. Elongation	68 °C	3 min
	go to step 2.	34 times
5. Final elongation	68 °C	7 min
6. Cooling	15 °C	∞

Table 2.2 PCR program for generation of the BAC targeting fragment

The PCR reaction was purified using the QIAquick PCR Purification Kit (Qiagen) according the manufacturer's instructions. Briefly, 250 μl Buffer PB were added to the PCR sample and mixed. The sample was applied to the membrane of a QIAquick spin column in a collection tube and was centrifuged at 16,100 × g for 1 min at RT. The flow-through was discarded, 750 μl Buffer PE were added, and the column was spun down as above. The flow-through was discarded, and the column again centrifuged for 1 min to remove residual wash buffer. The column was placed in a clean tube, and 50 μl ddH_2O were pipetted onto the center of the QIAquick membrane. After 1 min, the purified PCR reaction was eluted by spinning the column for 1 min at 16,100 × g. It was then treated with *Dpn*I. This enzyme cleaves DNA at methylated sites only. Thus, the template plasmid – but not the PCR product – is digested in order to prevent transformation of the template plasmid later. 3 μl *Dpn*I (10 U/μl; Roche), 6 μl Buffer A (Roche), and 1 μl ddH_2O were added to the 50 μl elution volume. The reaction was incubated o/n at 37 °C. The next day, the PCR product was extracted using the QIAquick Gel Extraction Kit (Qiagen). Therefore, the 2.8 kb PCR fragment band was excised from a 1% (w/v) agarose gel under UV light following electrophoresis. The gel slice was put in a standard tube, and 3 vol. Buffer QG were added. The gel slice was dissolved for 10 min at 50 °C. 1 vol. isopropanol was added to the sample before mixing it. The sample was applied to a QIAquick column, washed, and eluted in 50 μl ddH_2O as above. The purified PCR product was stored at -20 °C until further use.

Recombineering SW105 bacteria harboring the *Slitl2* BAC clone were grown o/n at 30 °C in 5 ml selective LB medium (1% Bacto™ Tryptone, BD; 0.5% Bacto™ Yeast Extract, BD; 0.5% NaCl; 25 μg/ml chloramphenicol). After a 15 min heat-shock at 42 °C to induce production of the recombination proteins (*exo*, *bet*, and *gam*), the bacterial suspension was centrifuged at 3,000 × g for 10 min at 0 °C in prechilled 15 ml tubes. The pellet was resuspended in 888 μl ice-cold ddH_2O, transferred to a 1.5 ml tube and again centrifuged at 16,100 × g for 20 sec at 0 °C. The supernatant was removed, and the pellet again resuspended in 888 μl ice-cold ddH_2O and centrifuged. This process was repeated three times before finally dissolving the pellet in 50 μl ice-cold ddH_2O. The bacterial suspension was pipetted onto the bottom of an electroporation cuvette (0.1 cm gap; Bio-Rad), and 10 μl purified PCR fragment were added. (As negative control, one sample without heat-induction was included). The electroporation was performed with a GenePulser (Bio-Rad) using 1.75 kV, 25 μF, and 200 Ω. 1 ml prewarmed LB medium was immediately added to the cuvette. The bacteria were transferred to a 1.5 ml tube and incubated at 32 °C for 1 h. After this recovery phase, 300 μl were plated on chloramphenicol (Cam; 25 μg/ml)- and kanamycin (Kan; 30 μg/ml)-containing LB agar plates (3.2% LB agar, Invitrogen) in order to select for clones that had successfully undergone recombineering. The plates were incubated o/n at 32 °C.

Identification of the targeted *Slitl2-Venus* BAC After two days, colonies were picked and grown o/n at 32 °C in 5 ml selective LB medium (Cam/Kan). The next day, the BAC DNA was isolated from the bacteria as follows: 2 ml of each o/n culture were centrifuged at 16,100 × g for 3 min at RT. The supernatant was discarded, and the bacterial pellet was carefully dissolved in 250 μl Buffer P1 (Qiagen). 250 μl Buffer P2 (Qiagen) were added, and the content was mixed by inverting the tube a few times. The bacteria were allowed to lyse for 5 min at RT. The reaction was neutralized by the addition of 350 μl Buffer N3 (Qiagen), and the content was mixed by inverting the tube. The mixture was spun down at 16,100 × g for 10 min at 20 °C. The supernatant was transferred into a new tube, and the DNA was precipitated by the addition of 0.7 vol. 100% isopropanol. The solution was mixed by invertion and centrifuged at 16,100 × g for 30 min at 10 °C. The supernatant was discarded, and the pellet was washed with 150 μl 70% EtOH. After a final centrifugation at 16,100 × g for 15 min at 10 °C, the pellet was quickly air-dried, and the isolated BAC DNA was dissolved in 20 μl TE buffer.

To verify that the isolated DNA was BAC DNA, 5 μl of each sample were digested o/n at 37 °C in a 20 μl reaction (2 μl 10× Buffer B (Roche), 1 μl *BamH*I (10 U/μl; Promega), 12 μl ddH_2O). The digestion pattern was analyzed on a 1% (w/v) agarose gel. The clone showing the correct BAC digestion pattern with multiple large bands without any template plasmid contamination was analyzed further by various PCRs to confirm that the entire Venus-neo insert had correctly integrated into the *Slitl2* locus. Therefore, primer pairs spanning over different fragment junctions were used. Pimers 326 and 327 were external primers on the original BAC clone to confirm site-directed targeting of the fragment. The standard PCR mix (Table 2.5) and standard PCR program (Table 2.6) with an annealing temperature of 60 °C and an elongation time of up to 3 min were used with several combinations of forward/reverse primers (Table 2.3). All primer sequences are listed on page 145. Following the PCR, 5 μl of each reaction were analyzed on a 1.5% (w/v) agarose gel. In addition, the PCR products were sequenced with the respective primers at MWG to verify the results.

Primer pair	**Fragment junction**	**Fragment size**
326/277	*Slitl2* intron/Venus ORF	222 bp
278/292	Venus ORF/neo ORF	300 bp
274/327	neo ORF/*Slitl2* exon 2	323 bp
326/292	*Slitl2* intron/neo ORF	1,078 bp
278/327	Venus ORF/*Slitl2* exon 2	2,015 bp

Table 2.3 Primer pairs used for the verification of correct integration of the Venus-neo fragment into the *Slitl2* locus of the BAC clone (ORF: open reading frame)

Large-scale isolation of the *Slitl2-Venus* BAC After confirmation of the correct sequences, *Slitl2-Venus* BAC-containing SW105 cells were grown o/n at 30 °C in 100 ml selective LB medium (Cam/Kan). The next day, the BAC DNA was isolated using the NucleoBond® BAC 100 Maxi Kit (Clontech) according to the manufacturer's instructions. The bacterial cells were harvested by centrifugation at 3,100 × g for 15 min at 4 °C. The pellet was carefully resuspended in 24 ml Buffer S1 (with RNase A), and 24 ml Buffer S2 were added to the suspension, which was then mixed by inverting the tube a few times. The mixture was in-

cubated for 3 min at RT before adding 24 ml Buffer S3. The mixture was again inverted a few times and then incubated on ice for 5 min. The lysate was cleared by centrifuging the suspension at high speed for 15 min at 4 °C. Meanwhile, a NucleoBond® Folded Filter was placed in a funnel and prewetted with a few drops of Buffer N2. After centrifugation, the lysate was carefully decanted onto the filter, and the flow-through was collected. The cleared lysate was loaded onto a preequilibrated NucleoBond® BAC 100 column, and the column was allowed to empty by gravity flow. The flow-through was reloaded before washing the column twice with 18 ml Buffer N3. The BAC DNA was eluted with 15 ml preheated (50 °C) Buffer N5. The DNA was precipitated by addition of 11 ml isopropanol. The mixture was centrifuged at 3,100 × g for 30 min at 4 °C, the supernatant was discarded, and 5 ml ice-cold 70% EtOH were added to the pellet. It was again centrifuged at 3,100 × g for 5 min at 4 °C. The supernatant was carefully removed, and the pellet was allowed to air-dry for 10 min. The pellet was then dissolved in 50 μl TE buffer. The final concentration was measured using a NanoPhotometer™ (Implen).

Linearization of the *Slitl2-Venus* BAC The BAC DNA was digested with *P*I-*Sce*I prior to electroporation into embryonic stem (ES) cells. This enzyme is a so-called homing endonuclease with long, not stringently-defined recognition sequences. Thus, single base changes do not abolish its cleavage capacity. It recognizes a sequence in the pBACe3.6 vector backbone, thereby linearizing the *Slitl2-Venus* BAC. 10 μg BAC DNA, 20 μl *P*I-*Sce*I (1 U/μl; NEB), 20 μl 10× Buffer (NEB), 10 μl 100× BSA (Promega) were adjusted to a final volume of 200 μl with ddH_2O. The reaction was incubated o/n at 37 °C. 100 ng of BAC DNA were analyzed on a 1% (w/v) agarose gel to verify linearization. Prior to preciptiation of the linearized BAC, proteins were removed by phenol/chloroform extraction. Therefore, 1 vol. phenol:chloroform (1:1) solution was added, and the suspension briefly vortexed before incubating it for 10 min at RT. The reaction was loaded onto Phase Lock Gel Heavy™ tubes (Eppendorf) and centrifuged at 16,100 × g for 1 min. The aqueous upper phase was transferred to a new tube, and the DNA was precipitated by adding 0.1 vol. 3 M sodium acetate pH 5.2 and 2.5 vol. cold 100% EtOH. The reaction was centrifuged at 16,100 × g for 10 min at 10 °C, and the pellet was washed with cold 70% EtOH. The sample was again spun down as above, and the pellet was resuspended in 25 μl PBS after it had been air-dried and stored at 4 °C until further use.

2.2.2 Generation of ES cell lines

All experimental procedures were based on the protocols described in [Nagy, 2003].

Electroporation The procedures were performed under sterile conditions in a laminar flow hood (HERAsafe®; Heraeus). 2-5 $\times$ 10^6 ES cells were seeded onto a monolayer of mitotically inactivated primary embryonic fibroblasts, i.e., feeder cells (3×10^6/plate), in a gelatin-coated 10 cm cell culture dish (Corning®) and incubated at 37 °C in a humified 5% CO_2 incubator (HERAcell 150; Heraeus). The cells were grown in ES cell medium composed of Dulbecco's Modified Eagle's Medium (DMEM containing 4,500 mg/ml glucose, without sodium pyruvate; Sigma-Aldrich), 15% (v/v) ES cell-qualified, heat-inactivated fetal bovine serum (FBS; Gibco), 2 mM L-glutamine (Sigma-Aldrich), 50 U/ml penicillin (Sigma-Aldrich), 50 μg/ml streptomycin (Sigma-Aldrich), 1% 100× non-essential amino acids (Sigma-Aldrich), 0.1 mM β-mercaptoethanol (Sigma-Aldrich), 1% 100× nucleosides (Sigma-Aldrich). 1000 U/ml murine leukemia inhibitory factor (LIF; Chemicon) were added to keep the ES cells in an undifferentiated state. The medium was exchanged daily until round colonies were visible. Before trypsinization, the ES cells were grown in fresh medium for at least 2 h. The medium was aspirated, and the cells were carefully washed twice with cell-culture grade D-PBS (Lonza). 1 ml trypsin/EDTA solution (Gibco) was added, and the cells were incubated at 37 °C for 10 min in order to disrupt cell-cell contacts. The enzyme was inactivated by the addition of 2 ml ES cell medium before pipetting vigorously up and down to produce a single cell suspension. The cell density was determined with a hemocytometer (Neubauer; Roth), and the cells were collected by centrifugation for 5 min at 200 $\times$ g. 2-5 $\times$ 10^6 ES cells were then resuspended in 800 μl D-PBS and transferred to an electropration cuvette (0.4 cm gap; Bio-Rad). The respective linearized DNA (*Slitl2* knock-out plasmid; *Slitl2-LacZ* knock-in plasmid; *Slitl2-Venus* BAC) was added and mixed with the ES cells. The cells were electroporated with a GenePulser (Bio-Rad) using 240 V and 500 μF. After electroporation, the cell suspension was immediately transferred to a 15 ml tube containing 10 ml ES cell medium, the cells were collected by centrifugation as above, and the pellet was resuspended in 10 ml ES cell medium. The cells were seeded on a monolayer of neomycin-resistant feeder cells (1×10^6/plate) in 6 cm cell culture dishes and incubated at 37 °C in ES cell medium. Selection for clones that had integrated the respective DNA fragment was started 36 h after

electroporation with selection medium (ES cell medium containing 350 μg/ml G418 Sulfate; Gibco). The medium was exchanged daily until ES cell colonies became visible (approximately 1 week after electroporation).

Picking Fresh ES cell medium was added to the cells 3-4 h prior to picking. The cells were washed twice with D-PBS before covering the colonies with a layer of fresh D-PBS. Individual colonies were picked using disposable 10 μl pipette tips under a stereo microscope (MZ8; Leica) and transferred to the wells of a round-bottomed 96-well plate (Corning®) filled with 50 μl cold trypsin/EDTA solution. After all colonies had been picked, the 96-well plate was placed in the 37 °C incubator for 10 min. 100 μl ES cell medium were added per well to inactivate the trypsin. The colonies were disaggregated with a multipipette and transferred to the wells of a gelatinized, flat-bottomed 96-well plate (Corning®) containing a monolayer of feeder cells (1×10^6 feeder cells/plate) and grown in regular ES cell medium. The next day, the medium was replaced by selection medium.

Splitting and freezing After the cells had been grown in selection medium for 2 days, they were washed twice with D-PBS before incubating them at 37 °C with 70 μl trypsin/EDTA for 10 min. The trypsinization was stopped by adding 140 μl bicarbonate-free DMEM (Sigma-Aldrich) supplemented with 10 mM HEPES (Sigma-Aldrich) and 20% FBS (v/v). The cells in the so-called 'DNA Original Plate' were disaggregated, and 70 μl of the 210 μl were transferred to the wells of a round-bottomed 96-well plate (Corning®) containing 70 μl 2×-concentrated ES cell freezing medium (bicarbonate-free DMEM (Sigma-Aldrich), 10 mM HEPES, 20% FBS, 20% DMSO). The contents of this so-called 'Master Plate' were mixed well by pipetting. Another 70 μl of the remaining 140 μl cell suspension were transferred to the wells of a gelatinized, flat-bottomed 96-well plate (Corning®) containing 200 μl ES cell medium ('DNA Replica Plate'), and the contents were again mixed. The 'Master Plate' was sealed, placed inside a styrofoam box, and frozen at -80 °C. 200 μl ES cell medium were added to the remaining 70 μl cell suspension in the 'DNA Original Plate' and the contents were mixed. The cells in the 'DNA Original Plate' and the 'DNA Replica Plate' were grown to confluency at 37 °C. DNA was isolated and subsequently used for analysis by Southern blot or by PCR (subsubsection 2.2.3.1 and subsubsection 2.2.3.2).

Transient expression of Cre recombinase Cre recombinase, an enzyme produced by the bacteriophage *P1*, is not present in mammalian cells. It mediates

DNA recombination at 34 bp long sequences, called *loxP*, thereby excising the DNA sequence flanked by these sites. In order to excise *loxP*-flanked, i.e., floxed, sequences in ES cells harboring a *Slitl2*$^{floxed\text{-}neo}$ allele to produce a *Slitl2*^{floxed} or a *Slitl2*^{null} allele, these cells were electroporated with a plasmid carrying the Cre recombinase coding sequence under control of the CMV-IE enhancer/β-actin promoter (pTurbo-Cre; kindly provided by Timothy Ley, M.D., The Washington University, St. Louis, MO, USA). 10 μg of the Turbo-Cre plasmid were precipitated with 0.1 vol. 3 M sodium acetate pH 5.2 and 2.5 vol. cold 100% EtOH. The contents were mixed and incubated at -80 °C for 10 min before spinning the reaction down at 16,100 × g for 10 min at 4 °C. The supernatant was removed, 200 μl cold 70% EtOH were added, and the reaction was again spun down as above. The supernatant was removed, the pellet was allowed to air-dry in a laminar flow hood and diluted in 10 μl PBS before adding it to 5×10^6 *Slitl2*$^{floxed\text{-}neo}$ allele-carrying ES cells. The subsequent procedures of electroporation, picking, splitting and freezing, and Southern blot analysis followed the basic protocols as described under subsection 2.2.2 and subsubsection 2.2.3.1. Of note, the cells were plated at very low densities following electroporation with the Turbo-Cre plasmid (1000/500/200 cells), and selection was no longer performed as Cre-mediated recombination potentially led to the excision of the neomycin selection cassette conferring resistance to the G418 selection drug.

2.2.3 Screening of ES cell clones

2.2.3.1 Southern blot analysis

Isolation of DNA Southern blot analysis was performed in order to identify ES cell clones that had successfully generated a *Slitl2*$^{floxed\text{-}neo}$, *Slitl2*^{floxed}, or *Slitl2*^{null} allele. It followed the protocol described in [Ramirez-Solis et al., 1993]. ES cells were grown to confluency in the wells of a 96-well plate (in the so-called 'DNA Original Plate' and the 'DNA Replica Plate' (subsection 2.2.2) in a humidified incubator at 37 °C and 5% CO_2 (HERAcell 150; Heraeus). The cells were carefully washed twice with D-PBS and 50 μl prewarmed lysis buffer (10 mM Tris-HCl pH 7.5, 10 mM EDTA pH 8.0, 10 mM NaCl, 0.5% sacrosyl) containing 1 mg/ml proteinase K (Roche) were added per well. The plate was placed inside a humified chamber and incubated o/n at 60 °C. The next day, 100 μl ice-cold 75 mM NaCl/100% EtOH were added without mixing. The plate was allowed to stand on the bench for 30 min to precipitate the DNA as a filamentous network

on the bottom of the wells. The plate was then carefully inverted to discard the solution, and excess liquid was blotted on a paper towel. The wells were rinsed 3 times by addition of 200 μl 70% EtOH. After the final wash, the precipitated DNA was allowed to dry on the bench. The 'DNA Replica Plate' was sealed and stored at -20 °C. The 'DNA Original Plate' was used for restricition enzyme digestion.

Digestion and gel electrophoresis A restriction digest mix was prepared containing 1 U/μl *Hind*III (Promega), 1× Buffer B (Roche), 1 mM spermidine (Promega), 100 μg/ml BSA (Promega), 100 μg/ml RNase A (Promega). The mix was prewarmed to 37 °C, and 30 μl were added to each well without mixing. The reaction was incubated at 37 °C for 2-4 h in a humified chamber before mixing the content of the wells. The 37 °C incubation was continued o/n in a humified chamber. The next day, 6 μl 6× gel loading buffer were added to each well, and the DNA was electrophoretically separated in a 0.7% TBE agarose gel in 1× TBE electrophoresis buffer for 12-18 h at 30 V. The next day, the gel was documented with the GelDoc™ 2000 system (Bio-Rad).

Blotting After electrophoretic size separation, the gel was pretreated in order to facilitate transfer of large DNA fragments. First, the DNA was partially depurinated by soaking the gel twice in 0.25 N HCl for 10 min. The gel was washed in ddH_2O for 5 min before denaturing the DNA by placing the gel in a bath of 0.5 N NaOH on a moving platform for 40 min at RT. The DNA was then blotted o/n onto a preequilibrated nylon Zeta-Probe® GT membrane (Bio-Rad) by capillary transfer. The DNA was UV-crosslinked to the membrane using 5000 μJ/cm^2 radiation (Stratalinker 2400; Stratagene). The membrane was washed twice in 2×-concentrated SSC pH 7.0 and either air-dried and stored at -20 °C in a sealed plastic bag or directly hybridized.

Probe labeling For the generation of the radioactively labeled 5' and 3' external probes, 25 ng of the respective template DNA fragments (694 bp and 485 bp, respectively) were diluted in 45 μl TE buffer and denatured for 3 min at 95 °C. After the sample was cooled down on ice for 2 min, it was added to a reaction tube containing a dried mix of dATP, dGTP, dTTP, Klenow enzyme, and random primers (Rediprime™ II Random Prime Labelling System; Amersham), and the components were mixed. All following procedures were performed in an isotope laboratory facility according to the manufacturer's instructions. 5 μl of

[α-^{32}P]dCTP (Redivue™; Amersham) with a specific activity of 3000 Ci/mmol were added, and the mixture was incubated for 10 min at 37 °C to allow for the labeling reaction catalyzed by the Klenow fragment of the DNA polymerase I. The radioactive sample was pipetted onto the Sephadex™ gel matrix of an equilibrated NICK™ column (Amersham) to separate the labeled probe from unincorporated radioactive nucleotides via gravity flow. 400 μl TE buffer were added, and the elution was discarded. Again, 400 μl TE buffer were added, and the purified sample was collected in a new tube. The labeled DNA probe was denatured for 3 min at 95 °C, briefly put on ice, and added to the hybridization buffer (see below).

Hybridization The DNA-blotted membrane was prehybridized in a glass bottle with 5 ml prewarmed ExpressHyb™ Hybridization Solution (Clontech) for 30 min in a hybridization oven (Hybaid Shake'n'Stack; Thermo Scientific) at 68 °C with constant rotation. After prehybridization, the denatured, labeled probe was added to the solution, and the membrane was hybridized o/n at 60 °C with constant rotation. The next day, the membrane was washed in 2×-concentrated SSC pH 7.0 for 5 min rocking at RT, in preheated 2× SSC/1% SDS for 30 min at 60 °C (the membrane was turned over after 15 min), and – if higher stringency was required – in 0.1× SSC/0.1% SDS for up to 30 min. A rinse in 0.1× SSC at RT followed before sealing the membrane inside a plastic bag. The radioactively labeled DNA was then detected by autoradiography using conventional X-ray films (BioMax MS, Kodak).

2.2.3.2 PCR screening

Both the *Slitl2-LacZ* and the *Slitl2-Venus* ES cell clones were screened via PCR. The isolation of the DNA followed the same protocol as described above (subsubsection 2.2.3.1).

***Slitl2-LacZ* ES cell clones** The clones carrying a *Slitl2*$^{LacZ\text{-}neo}$ allele were identified using the Expand Long Template PCR System (Roche) according to the protocol of the European Conditional Mouse Mutagenesis Program (EUCOMM; http://www.eucomm.org). Each reaction mix contained 2 μl forward primer (3 μM), 2 μl reverse primer (3 μM), 0.75 μl dNTPs (10 mM), 0.15 μl 100% DMSO, 0.75 μl $MgCl_2$ (25 mM), 1.0 μl trehalose (1 M), 1.5 μl 10×-concentrated Expand Long Template Buffer 2, 0.1 μl Expand Long Template Enzyme Mix,

6 μl DNA, and 0.75 μl ddH_2O. The primer combinations for the 5' and the 3' end were 637/274 and 388/639, respectively. All primer sequences are listed on page 145. The PCR was run in a sealed 96-well PCR plate (ThermoFast® 96, non-skirted; Thermo Scientific) on a Mastercycler ep gradient S (Eppendorf) using the program listed in Table 2.4. Following the PCR reaction, 5 μl ddH_2O were added to each well, and 10 μl were taken off to verify the correct amplification on a 1% (w/v) agarose gel as described under subsection 2.2.5. The expected fragment size was 2.9 kb and 3.7 kb for the 5' and the 3' end, respectively.

Step	**Temperature**	**Time**
1. Initial denaturation	94 °C	2 min
2. Denaturation	93 °C	15 sec
3. Annealing	70 °C	30 sec
4. Elongation	68 °C	6 min
reduce annealing temperature	go to step 2. 1 °C per step	9 times
5. Denaturation	93 °C	15 sec
6. Annealing	60 °C	30 sec
7. Elongation	68 °C	6 min
increase elongation time	go to step 5. 20 sec per step	24 times
8. Final elongation	68 °C	7 min
8. Cooling	15 °C	∞

Table 2.4 PCR program for screening of *Slitl2-LacZ* ES cell clones

***Slitl2-Venus* ES cell clones** In addition to the above described internal PCRs (Table 2.3), two PCRs were conducted to confirm integration of the entire *Slitl2-Venus* BAC transgene. Therefore, primer pairs spanning the pBACe3.6 vector–*Slitl2* BAC junctions were selected. The PCR mix and the PCR program followed the standard protocols described in Table 2.5 and Table 2.6 using an annealing temperature of 60 °C. The primer combinations for the 5' and the 3' and were

408/410 and 407/409, respectively. All primer sequences are listed on page 145. 10 μl of each reaction were subsequently analyzed by gel electrophoresis as described under subsection 2.2.5.

2.2.4 Generation of mouse lines

After identification of the clones that had undergone successful recombination or had successfully integrated the BAC genome, the respective 'Master Plate' was retrieved from the -80 °C freezer and placed in a 37 °C incubator to allow for thawing of the cells. The cells from the wells corresponding to the correct clones were each transferred to 15 ml tubes containing 5 ml ES cell medium and spun down at 200 × g for 5 min. The supernatant was carefully aspirated, the pellet resuspended in ES cell medium, and the cells were plated on a monolayer of feeder cells. The cells were grown in ES cell medium at 37 °C for propagation. They were subsequently used for the generation of mutant mouse lines via morula injection (*Slitl2-floxed*), the ES cell-morula aggregation technique (*Slitl2-null*, *Slitl2-Venus*), or the ES cell–tetraploid embryo aggregation technique (*Slitl2-floxed-neo*, *Slitl2-LacZ-neo*). These procedures were performed by Karol Macura and Ingo Voigt (Max Planck Institute for Molecular Genetics, Berlin, Germany) and followed the protocols described in [Nagy, 2003]. For the morula injection, the laser system XYclone (Hamilton Thorne) was used. Embryos from C57BL/6 mice were used for the morula injection, while for all other procedures, CD-1® embryos were employed.

2.2.5 Genotyping of mice

Isolation of DNA Genomic DNA was isolated according to the protocol described in [Laird et al., 1991] as follows. Tail biopsies of 0.5-1 cm were incubated o/n at 56 °C with gentle agitation in 0.5 ml lysis buffer (200 mM NaCl, 100 mM Tris-HCl pH 8.5, 5 mM EDTA, 0.2% SDS) with 150 μg/ml proteinase K (Roche). The lysates were centrifuged for 10 min at 16,100 × g, and the supernatants were poured into new tubes containing 0.5 ml isopropanol. The samples were mixed until the DNA was completely precipitated, the precipitates were fished out using disposable tips and transferred to new tubes containing 0.5 ml TE buffer. The DNA was dissolved for several hours at 37 °C under agitation and stored at 4 °C.

Polymerase chain reaction (PCR) For PCR analysis of the above obtained DNA, a reaction mix was prepared on ice. The master mix contained PCR buffer (200 mM Tris pH 8.4, 500 mM KCl), $MgCl_2$, dNTP mix (dATP, dCTP, dGTP, dTTP), *Taq* DNA polymerase (all from Invitrogen), and primers. All primers were ordered from MWG and adjusted to a final concentration of 20 μmol with ddH_2O prior to use. A list of all primer sequences can be found on page 145. 1 μl of genomic DNA was used as template in a 50 μl reaction (Table 2.5). A negative control without template was included in each run. For the *Slitl2-floxed-neo* and the *Slitl2-null* mouse strain, a 3-primer PCR was performed using the primer combinations 326/327/274 and 442/326/110, respectively. Therefore, 0.5 μl of the respective third primer (20 μM) was added to reaction mix. The volume was subtracted from the amount of added ddH_2O.

Components of Master Mix	**Volume**	**Final concentration**
10× PCR buffer w/o $MgCl_2$	5.0 μl	1×
$MgCl_2$, 50 mM	1.5 μl	1.5 mM
dNTP mix, 10 mM each	1.0 μl	200 μM each
Forward primer, 20 μM	0.5 μl	0.2 μM
Reverse primer, 20 μM	0.5 μl	0.2 μM
Taq DNA polymerase, 5U/μl	0.5 μl	0.05 U/μl
ddH_2O	40.0 μl	
Volume of Master Mix	**49.0** μl	
DNA template	1.0 μl	
Final volume	**50.0** μl	

Table 2.5 Standard PCR mix

A standard PCR program with repeated cycles of denaturation, annealing, and elongation was run on an MJ Research PTC-200 Thermal Cycler using the parameters listed in Table 2.6. The annealing temperature was adjusted for each primer pair. The elongation time was chosen according to the expected fragment size. Details on primer pairs, detected alleles, annealing temperature ($T_\mathbf{a}$), and

amplified fragment size of the different PCRs for the various mouse strains are listed in Table 2.7. All primer sequences are listed on page 145.

Step	Temperature	Time
1. Initial denaturation	94 °C	4 min
2. Denaturation	94 °C	30 sec
3. Annealing	50-62.5 °C	30 sec
4. Elongation	72 °C	30 sec
	go to step 2.	34 times
5. Final elongation	72 °C	7 min
6. Cooling	15 °C	∞

Table 2.6 Standard PCR program

Mouse strain	Primer pair	Detected allele	T_a	Fragment
Slitl2-floxed-neo	326/274	*Slitl2*$^{floxed\text{-}neo}$	60.0 °C	186 bp
	326/327	*Slitl2*$^{wild\text{-}type}$	62.5 °C	293 bp
Slitl2-floxed	109/110	*Slitl2*^{floxed}	60.0 °C	153 bp
	109/110	*Slitl2*$^{wild\text{-}type}$	60.0 °C	107 bp
Slitl2-null	326/110	*Slitl2*^{null}	62.5 °C	146 bp
	442/110	*Slitl2*$^{wild\text{-}type}$	62.5 °C	348 bp
Slitl2-LacZ	379/380	*Slitl2*^{LacZ}	60.0 °C	429 bp
Slitl2-Venus	326/277	Venus transgene	60.0 °C	222 bp

Table 2.7 Overview of genotyping PCRs

Agarose gel electrophoresis The PCR products were subsequently analyzed on a 2% (w/v) agarose gel. UltraPure™ agarose (Invitrogen) was mixed with the appropriate volume of 1× TAE buffer in a glass beaker, microwaved until dissolved, and cooled to about 60 °C. Ethidium bromide was added at a concen-

tration of 0.2 μg/ml, and the solution was well swirled before pouring it into a gel tray holding a comb. The comb was removed after solidification of the gel, and the tray was placed in a gel chamber (PerfectBlue Gel System; Peqlab) filled with 1× TAE electrophoresis buffer. The first well was loaded with marker (GeneRuler™ 100bp Plus DNA Ladder (Fermentas) or 1 Kb Plus DNA Ladder (Invitrogen)). 2 μl 6× gel loading buffer were added to 10 μl of PCR mix before loading the samples. Following electrophoretic size separation, the PCR products were visualized under transilluminescent UV light (λ=302 nm) and documented using the GelDoc™ 2000 system (Bio-Rad).

2.2.6 Generation of mouse primary embryonic fibroblasts

The procedure followed the basic protocol described in [Abbondanzo et al., 1993]. Timed-pregnant mice were euthanized via cervical dislocation. The uterus was removed, and the embryos (stage E14.5) were individually dissected in cold PBS. The head was removed and used for genotyping according to the protocol described in subsection 2.2.5. For each embryo, the visceral organs were removed, and the carcass was washed twice in PBS. It was minced into 2-3 mm^2 tissue pieces with a pair of fine forceps. The pieces were transferred to standard tubes containing 1 ml trypsin/EDTA solution (Gibco). The tissue was digested for 5 min at 37 °C, briefly vortexed, and again incubated for 25 min at 37 °C. The sample was briefly vortexed before pipetting vigorously up and down to produce a single cell suspension. 5 ml feeder cell medium (Dulbecco's Modified Eagle's Medium containing 4,500 mg/ml glucose, without sodium pyruvate (Sigma-Aldrich), 10% (v/v) FBS, 2 mM L-glutamine (Sigma-Aldrich), 50 U/ml penicillin (Sigma-Aldrich), 50 μg/ml streptomycin (Sigma-Aldrich)) were added, and the cells were again disaggregated by pipetting up and down before adding another 5 ml feeder cell medium. The cells of each embryo were plated on a 10 cm cell culture dish and incubated in a humidified incubator at 37 °C and 5% CO_2 (HERAcell 150; Heraeus).

2.3 Molecular and cellular biology

2.3.1 Northern blot analysis

Isolation of RNA Total RNA was isolated from whole embryos and adult tissues using the RNeasy Mini or Midi Kit (Qiagen) according to the manufacturer's instructions. All volumes were adjusted accordingly. Briefly, fresh tissue was homogenized in RLT Buffer with a T8 Ultra-Turrax® disperser (IKA-Werke) and centrifuged at full speed for 3 min. The supernatant was transferred into a new tube, and 1 vol. 70% EtOH was added to the lysate, and the contents were mixed by pipetting. The sample was transferred to an RNeasy column placed in a collection tube and centrifuged, and the flow-through was discarded. RW1 Buffer was added, and the column was again spun down. An on-column DNase digestion step was performed: RNase-free DNase I was mixed with RDD Buffer and pipetted onto the spin column membrane, which was then incubated on the benchtop for 15 min. RW1 Buffer was added, and the column was centrifuged. The flow-through was discarded. The membrane was washed twice with RPE Buffer before eluting the RNA with RNase-free H_2O into a new collection tube. The RNA concentration was measured using a NanoPhotometer™ (Implen).

Gel electrophoresis 10 μg of the above purified RNA of each sample were precipitated as follows. 4 μl 10 M ammonium acetate, 0.4 μl glycogen, and 50 l ice-cold 100% EtOH were added per 11 μl initial volume and well mixed. The samples were incubated at -20 C for several hours before spinning them down at 16,100 × g for 30 min at 4 °C. The supernatant was removed, and 200 μl ice-cold 70% EtOH were added. The supernatant was again removed, and the pellets were allowed to air-dry. The subsequent electrophoretic size separation was performed according to the protocol described in [Fourney et al., 1988]. The pellets were dissolved in 5 μl sample dissolving solution (25 mM EDTA/0.1% SDS), and 25 μl freshly prepared electrophoresis sample buffer (750 μl deionized formamide, 150 μl 10×-concentrated MOPS buffer, 240 μl 37% formaldehyde, 100 μl RNase-free H_2O, 100 μl glycerol, 80 μl 10% (w/v) bromophenol blue (Sigma-Aldrich)) were added before incubating the samples at 65 °C for 15 min. Finally, 1 μl 0.1% ethidium bromide was added, the samples thoroughly mixed and stored on ice. A denaturing formaldehyde gel was prepared as follows: per 100 ml of the gel, 1.5 g UltraPure™ agarose (Invitrogen) were dissolved in 87 ml RNase-free H_2O in a microwave oven and cooled to about 50 °C before adding 10 ml 10× MOPS buffer.

In a fume hood, 5.1 ml 37% formaldehyde were mixed with the solution, which was then carefully poured in an RNase-free gel tray holding a comb. After solidifation of the gel, the samples were loaded into the wells. The first well was loaded with 5 μl 0.24-9.5 kb RNA Ladder (Invitrogen). The RNA was electrophoretically separated for 18 h at 20 V in a fume hood. The next day, the gel was documented using the GelDoc™ 2000 system (Bio-Rad).

Blotting After electrophoretic size separation, the gel was washed twice in 10× SSC pH 5.0 for 20 min at RT with gentle shaking. The RNA was blotted o/n onto a preequilibrated positively charged nylon membrane (GeneScreen Plus™ Hybridization Transfer Membrane; PerkinElmer) by capillary transfer. The RNA was UV-crosslinked to the membrane using 5000 μJ/cm^2 radiation (Stratalinker 2400; Stratagene) and either air-dried and stored at -20 °C in a sealed plastic bag or directly hybridized.

Probe labeling and hybridization Both the probe labeling and the hybridization procedures were identical to that of the Southern blot analysis (subsubsection 2.2.3.1). For the Northern blot analysis, specific probes to detect *Slitl2* or *Gapdh* RNA expression were generated from the respective DNA templates, and RNase-free solutions were used at all times.

2.3.2 cDNA microarray analysis

The Illumina® TotalPrep™ RNA Amplification Kit (Ambion) was used for generating biotinylated, amplified cRNA for hybridization on Illumina Sentrix® arrays. All steps were performed according to the manufacturer's instructions.

First strand cDNA synthesis DNase-digested total RNA was prepared with the RNeasy Mini or Midi Kit (Qiagen) as described under subsection 2.3.1. For a single reaction, 500 ng RNA were diluted in a total volume of 11 μl RNase-free H_2O in a sterile, RNase-free tube. For each sample, a Reverse Transcription Master Mix was assembled at RT as follows: 1 μl T7 Oligo (dT) Primer, 2 μl 10× First Strand Buffer, 4 μl dNTP Mix, 1 μl RNase Inhibitor, and 1 μl ArrayScript were mixed well, and 9 μl of the Master Mix were transferred to each RNA sample. The samples were thoroughly mixed by pipetting, briefly centrifuged to collect the reaction at the bottom of the tube, and placed in a 42 °C incubator for 2 h. After the incubation, the tubes were immediately put on ice.

Second strand cDNA synthesis 80 μl Second Strand Master Mix was prepared on ice (63 μl RNase-free H_2O, 10 μl 10× Second Strand Buffer, 4 μl dNTP Mix, 2 μl DNA Polymerase, 1 μl RNase H) and transferred to each sample. The contents were mixed well, briefly centrifuged and incubated at 16 °C for 2 h. After the incubation, the tubes were immediately placed on ice.

cDNA purification 250 μl cDNA Binding Buffer were added to each sample, the samples were mixed, and the reaction was pipetted onto the center of the cDNA Filter Cartridge. The cartridges were centrifuged at 10,000 × g for 1 min at RT. The flow-through was discarded, and 500 μl Wash Buffer were applied to each cartridge before centrifuging them again as above. The flow-through was discarded, and the cartridges were again spun to remove trace amounts of buffer. The cartridges were placed in a cDNA Elution Tube, and 10 μl preheated (55 °C) RNase-free H_2O were applied to the center of the filter. After a 2-min incubation at RT, the cartridges were again spun. Additional 9 μl preheated RNase-free H_2O were pipetted onto the filter, and the cartridges were centrifuged at 10,000 × g for 2 min at RT. The eluted, purified cDNA samples were either stored at -20 °C or directly used to proceed with the protocol.

cRNA transcription The IVT Master Mix was prepared at RT (2.5 μl T7 10× Reaction Buffer, 2.5 μl T7 Enzyme Mix, 2.5 μl Biotin-NTP Mix), and 7.5 μl IVT Master Mix were added to each purified cDNA sample. The samples were thoroughly mixed by pipetting, briefly centrifuged to collect the reaction at the bottom of the tube, and placed in a 37 °C incubator for 14 h. The reaction was stopped by the addition of 75 μl RNase-free H_2O.

cRNA purification 350 μl cRNA Binding Buffer and 250 μl 100% EtOH were added to each sample. The contents were mixed by pipetting and directly transferred onto the center of a cRNA Filter Cartridge. The cartridges were centrifuged at 10,000 × g for 1 min at RT, and the flow-through was discarded. 650 μl Wash Buffer were applied to each cartridge, which were again spun as above. The flow-through was discarded, and the cartridges again centrifuged to remove trace amounts of buffer. The cartridges were placed in cRNA Collection Tubes, and 70 μl preheated (55 °C) RNase-free H_2O were applied to the center of the filter. After a 2-min incubation at RT, the purified cRNA was eluted by spinning the cartridges at 10,000 × g for 2 min at RT. The cRNA concentration was measured

using a NanoPhotometer™ (Implen), and the cRNA quality was assessed on a 1% (w/v) agarose gel.

Hybridization To assess genome-wide expression profiles, 750 ng purified cRNA in a total volume of 5 μl RNase-free H_2O were provided for each sample. The samples were hybridized to MouseRef-8 Expression BeadChips (Illumina) and scanned on the Illumina BeadArray Reader. All these procedures were performed by Pamela Kepper (Service Department, Max Planck Institute for Molecular Genetics, Berlin, Germany) according to the manufacturer's instructions.

Data analysis Scaling and quantile normalization was applied to the raw data from the Illumina Bead Array Reader to generate dendrograms and lists of deregulated genes. Adjusted *P*-values were calculated using the method of Benjamini and Hochberg [Benjamini and Hochberg, 1995]. These procedures were performed by Dr. Martin Werber (Max Planck Institute for Molecular Genetics, Berlin, Germany) using the *beadarray* package from the open source software Bioconductor (http://www.bioconductor.org/). Functional annotation clustering of the generated lists of genes was performed with the online available DAVID Bioinformatics Database tool (http://david.abcc.ncifcrf.gov/) using the predefined high classification stringency.

2.3.3 Quantitative real-time PCR

Selection of primers Selected results from the cDNA microarray analysis were confirmed by quantitative real-time PCR. Therefore, primers were selected using the online software 'Primer3' (http://frodo.wi.mit.edu/primer3/input.htm). They were designed to anneal to the mRNA sequence in two different exons spanning over an intron to allow differentiation between the amplified cDNA and PCR products derived from potential contaminating genomic DNA. All primers were ordered from MWG and adjusted to a final concentration of 20 μM with ddH_2O prior to use. Table 2.8 lists all genes with the respective primer pair. A list of all primer sequences can be found on page 145.

Gene	Primer pair (5'/3')	Product size
Bmp4	779/780	119 bp
Ctgf	787/788	100 bp
Flt1	795/796	119 bp
Areg1	801/802	109 bp
Timp1	805/806	111 bp
Tnfrsf12a	809/810	107 bp
Gapdh	Gapdh5'/Gapdh3'	202 bp

Table 2.8 Primer pairs used for quantitative real-time PCR

Reverse transcription (RT)-PCR The SuperScript™ III First-Strand Synthesis System for RT-PCR from Invitrogen was used for reverse transcription of RNA into cDNA. The isolation of RNA is described under subsection 2.3.1. The same samples as used for the microarray analysis served as templates in this assay. Therefore, 8 μg RNA were diluted in a total volume of 8 μl DECP-H_2O. 1 μl random hexamers and 1 μl dNTP mix (10 mM) were added per reaction, and the samples were incubated at 65 °C for 5 min before placing them on ice for 1 min. A reaction mixture was prepared containing 2 μl 10× RT Buffer, 4 μl $MgCl_2$ (25 mM), 2 μl 0.1 M DTT, 1 μl RNaseOUT per sample. It was added to the RNA mixture and incubated at 25 °C for 2 min. 1 μl SuperScript™ III (50 U/μl) reverse transcriptase was added, and the samples were incubated successively at 25 °C for 10 min, at 42 °C for 50 min, and at 70 °C for 15 min. The reactions were cooled on ice before adding 1 μl RNase H to each tube and incubating them for 20 min at 37 °C. The cDNA samples were stored at -20 °C until further use.

Quantitative real-time PCR Quantitative real-time PCR was performed with the above yielded cDNA using the Power SYBR® Green PCR Master Mix (Applied Biosystems). This mix contains polymerase, dNTPs, buffer, and SYBR® Green I Dye, which binds to double-stranded DNA. Thus, the fluorescent signal reflects the amount of double-stranded PCR product that is generated during the reaction. For each reaction, a mixture of 10 μl Power SYBR® Green PCR Master Mix, 0.5 μl forward primer (20 μM), 0.5 μl reverse primer (20 μM), and 7 μl

DECP-H_2O were transferred to the wells of a MicroAmp® Fast Optical 96-Well Reaction Plate (Applied Biosystems) before adding 2 μl of 1:20 diluted cDNA sample. Each sample was run in technical triplicates. Negative controls without cDNA were included in each run. The reaction was run on a StepOne™ Real-Time PCR System according to the program listed below (Table 2.9). The results were analyzed using the StepOnePlus™ Software v2.0.2. The housekeeping gene *Gapdh* was used as internal control for normalization of each cDNA sample.

Step	**Temperature**	**Time**
1. Initial denaturation	95 °C	10 min
2. Denaturation	95 °C	15 sec
3. Elongation	60 °C	30 sec
	go to step 2.	39 times
4. Melt curve	95 °C	15 sec
	60 °C	15 sec
	95 °C	15 sec
6. Cooling	30 °C	∞

Table 2.9 Quantitative real-time PCR program

2.3.4 Western blot analysis

Isolation of proteins from cells The cell lysis buffer was freshly prepared before use by dissolving one protease inhibitor cocktail tablet (Complete Mini, Roche) in 10 ml cell lysis buffer (10 mM Tris-HCl pH 8.0, 2.5 mM $MgCl_2$, 5 mM EGTA pH 8.0, 0.5% Triton X-100). The solution was thoroughly mixed and put on ice. Mouse primary embryonic fibroblasts (subsection 2.2.6), that were grown on 10 cm culture dishes to approximately 90% confluency, were carefully washed twice with PBS before adding 750 μl cell lysis buffer. The dishes were put on ice, and the cells were washed off, transferred into a 1.5 ml tube, briefly vortexed, and incubated on ice for 20 min to allow for lysis of the cells. The protein lysates were centrifuged at 1,500 × g for 10 min at 4 °C. The supernatant was collected, snap frozen on dry ice, and stored at -80 °C until further use.

Sodium dodecyl sulfate polyacrylamide gel electrophoresis (SDS-PAGE) The proteins were separated via sodium dodecyl sulfate polyacrylamide gel electrophoresis (SDS-PAGE) using the XCell SureLock™ Mini-Cell system (Invitrogen). Therefore, the above obtained protein lysates were thawed on ice. 15 μl protein lysate were mixed with 5 μl 4× NuPAGE® LDS Sample Buffer (Invitrogen), and the proteins were denatured at 70 °C for 10 min, then put on ice. Precast NuPAGE® 4-12% Bis-Tris gels were placed in the Mini Cell, and the system was filled with 1× NuPAGE® MOPS SDS Running Buffer (Invitrogen). The denatured protein samples were loaded into the wells. SeeBlue® Plus2 Pre-Stained Standard (Invitrogen) served as protein molecular weight marker. The proteins were electrophoretically separated for 1 h at 200 V.

Blotting and detection of proteins The proteins were blotted onto a polyvinylidene fluoride (PVDF) membrane (Immobilon-P; Millipore) using the Mini Trans-Blot™ cell system (Bio-Rad). Prior to use, the membrane was permeabilized in 100% MetOH for 2 min and rinsed with transfer buffer (192 mM glycine, 25 mM Tris). The proteins were blotted in transfer buffer for 1 h at 100 V. The protein transfer was verified by immersing the membrane in Ponceau S Staining Solution (Sigma-Aldrich) for 5 min. After the proteins had been visualized, the membrane was rapidly immersed in 0.1 M NaOH before rinsing it with ddH_2O for 2-3 min. The membrane was then blocked o/n at 4 °C in TBST containing 5% milk powder (Fluka). The next day, the membrane was washed once with TBST for 15 min at RT before incubating it with α-Slitl2 antibody (1:2,000) in 1% milk/TBST for 2 h at RT. The membrane was again washed 3× in TBST and then incubated with a 1:10,000 dilution of horseradish peroxidase (hrp)-coupled secondary antibody (ECL Rabbit IgG, hrp-coupled, NA943; Amersham) in 1% milk/TBST for 1 h at RT. Five washes in TBST and one wash in TBS, each 15 min at RT, followed. The ECL™ Advance Western Blotting Detection Kit and Hyperfilm-ECL films (Amersham) were used for radiographic detection.

2.3.5 Flow cytometric analysis

Preparation of single cell suspensions Mice were euthanized via cervical dislocation. The thymus and the spleen were dissociated in 1 ml 0.5% (w/v) BSA (Sigma-Aldrich) in PBS by forcing the respective tissue through the mesh of a commercial stainless-steel sieve using the plunger of a syringe. Bone marrow cells were harvested by flushing the cavities of femur and tibia with 1 ml 0.5% BSA/PBS. The cell supsensions were centrifuged at 500 × g for 5 min at 4 °C before resuspending the pellets in 500 μl red blood cell (RBC) lysis buffer (155 mM NH_4Cl (Sigma-Aldrich), 0.13 mM EDTA, 10 mM $KHCO_3$ (Roth)). After an incubation for 5 min at RT, lysis was stopped by adding 500 μl 0.5% BSA/PBS. The cells were pelleted as above and filtered through MACS® Pre-Separation Filters (Miltenyi Biotec) in a total volume of 1 ml 0.5% BSA/PBS. The cell suspension were again spun down as above. The cells from the spleen, the bone marrow, and the thymus were resuspended in 500 μl, 300 μl, and 150 μl 0.5% BSA/PBS, respectively. To evaluate total cell numbers, 10 μl were diluted with 90 μl trypan blue solution (Sigma-Aldrich), which stains dead cells blue. Live, unstained cells were then counted using a hemocytometer (Neubauer; Roth).

Antibody incubation and flow cytometric analysis 10 μl cell suspension were pipetted into the wells of a conical-bottomed 96-well plate (Corning®), and fluorochrome-labeled antibodies were added in a predefined combination at 1 μl aliquots. The antibodies were diluted in 0.5% BSA/PBS prior to use. The cells were incubated for 15 min at 4 °C in the dark to allow coupling of the antibodies. 200 μl 0.5% BSA/PBS were added to each well, the plate was centrifuged at 500 × g for 3 min, and the pellets were diluted in 250 μl 0.5% BSA/PBS. Table 2.10 lists all antibodies with their respective clone name, fluorochrome label, dilution factor, and supplier. For each sample, 50,000-100,000 cells were counted with a FACSCalibur™ Flow Cytometer (BD Biosciences) and the collected data were subsequently analyzed using the FlowJo 7.2.5 software (Tree Star).

Specificity	Clone	Label	Dilution	Supplier
CD4	RM4-5	PerCP	1:400	BD Biosciences
CD8a	53-6.7	PE	1:200	BD Biosciences
CD69	H1.2F3	FITC	1:200	BD Biosciences
TCRβ	H57-597	APC	1:200	BD Biosciences
CD21	B3/B4	PE	1:200	DRFZ Berlin
CD23	7G6	Cy5	1:800	DRFZ Berlin
IgMb	AF6-78	Alexa488	1:50	DRFZ Berlin
B220	RA3.6B2	Cy5	1:800	DRFZ Berlin

Table 2.10 Antibodies used for flow cytometric analysis

2.4 Histology

2.4.1 Standard staining procedures

Specimen preparation Mice were euthanized via cervical dislocation. Tissues were harvested under sterile conditions and fixed o/n at 4 °C in 10% neutral buffered formalin solution (Sigma-Aldrich). The next day, the samples were washed twice with PBS before manually processing them through a graded ethanol series: 30%, 50%, 70% EtOH, each for 15 min at 4 °C. The subsequent steps of dehydration and paraffin infiltration were performed automatically in a MICROM STP 120 processor (MICROM) according to the following program:

Solution	Time	Agitation
80% EtOH	120 min	2
96% EtOH	120 min	2
100% EtOH	60 min	2
100% EtOH	60 min	2
100% EtOH	60 min	2
100% Xylene	90 min	2
100% Xylene	90 min	1
100% Paraffin	120 min	1
100% Paraffin	120 min	1

Table 2.11 MICROM STP 120 program

The specimens were embedded in metal molds with paraffin (Histowax; Leica) using an EC 350-1 embedding station (MICROM) and placed onto the cooling plate until the paraffin block was solidified. 5 μm-thick sections were cut on a rotary microtome (HM 355 S; MICROM), transferred onto adhesion microscope slides (SuperFrost®; Menzel), and dried o/n at 37 °C. All slides were stored in a desiccated slide box at 4 °C until further use.

2.4.1.1 Hematoxylin and Eosin (H&E) staining

Formalin-fixed, paraffin-embedded sections were deparaffinized in xylene (2× for 8 min) and rehydrated (100% EtOH, 2× for 5 min; 90% EtOH, 80% EtOH, ddH_2O, each 1× for 5 min). The samples were stained with Mayer's Hematoxylin Solution (Sigma-Aldrich) for 3 min, washed under running tap water for 15 min, dipped in 0.25% HCl/EtOH for 3 sec followed by a 5-min incubation in tap water, stained with alcoholic Eosin Y Solution (Sigma-Aldrich) for 5 min, and briefly washed in ddH_2O for 30 sec. The sections were then dehydrated (dip into 90% EtOH, 100% EtOH 2× for 5 min, xylene 1× for 5-10 min), immediately mounted in Entellan® (Merck), and covered with glass cover slips (Roth).

2.4.1.2 Periodic acid-Schiff (PAS) staining

The PAS staining was used to detect polysaccharides, which stain magenta-purple with this method. The sections were deparaffinized and rehydrated as above (subsubsection 2.4.1.1). The PAS staining kit from Merck was used for the subsequent staining procedure. The samples were placed in 0.5% periodic acid solution for 5 min, washed under running tap water for 3 min, rinsed in ddH_2O, and incubated in Schiff's reagent for 15 min. The slides were again washed under running tap water for 3 min and rinsed in ddH_2O before staining the specimens in Mayer's Hematoxylin Solution for 2 min. Excess staining solution was washed off under running tap water for 3 min. The sections were then dehydrated and mounted as above.

2.4.1.3 Masson's trichrome staining

The Masson's trichrome staining was employed to detect collagen, which stains blue with this method. Accustain® Trichrome Stains (Sigma-Aldrich) were used for this staining procedure. The sections were deparaffinized and rehydrated as above (subsubsection 2.4.1.1) and incubated in preheated Bouin's solution (Sigma-Aldrich) at 56 °C for 15 min. Excess Bouin's solution was washed off under running tap water. The tissue was stained in Weigert's Iron Hematoxylin Working Solution (1:1 Reagent A:Reagent B; Sigma-Aldrich) for 5 min at RT before washing the sections for 5 min under running tap water and rinsing them in ddH_2O. The slides were stained in Biebrich Scarlet-Acid Fuchsin for 5 min, rinsed in ddH_2O, and placed in Phosphotungstic/Phosphomolybdic Acid Working Solution (1:1:2 Phosphotungstic Solution:Phosphomolybdic Solution:H_2O) for 5 min

followed by a 5-min incubation in Aniline Blue Solution. The slides were rinsed in ddH_2O and incubated for 3 min in 1% acetic acid solution. The sections were then dehydrated and mounted as above.

Imaging Tissue sections were photographed with an AxioStar *plus* microscope (Zeiss) and a DFC320 camera (Leica) using the FireCam V3.0 software (Leica).

2.4.2 Whole-mount *in situ* hybridization

The procedures for the whole-mount *in situ* hybridization followed the online available protocols of the Molecular Anatomy of the Mouse Embryo Project (mamep) of the Max Planck Institute for Molecular Genetics (Berlin, Germany; http://mamep.molgen.mpg.de/). For all steps, RNase-free solutions were used.

Fixation of mouse embryos Timed-pregnant mice were euthanized via cervical dislocation. The uterus was removed, and the embryos were dissected in cold PBS and fixed o/n at 4 °C in 4% PFA/PBS solution on a roller mixer. The next day, the fixative was removed by two washes with cold PBS for 10 min, and the embryos were dehydrated through a graded methanol series (25% MetOH/PBS, 50% MetOH/PBS, 75% MetOH/PBS, 1× for 10 min each, 100% MetOH 2× for 10 min). All steps were performed at 4 °C on a roller mixer with precooled solutions. The fixed embryos were stored in 100% MetOH at -20 °C until further use.

Processing of mouse embryos The desired number of fixed embryos of one stage were pooled. If not stated otherwise, all subsequent steps comprised a 10-min incubation at 4 °C on a roller mixer. The embryos were rehydrated (1× 75% MetOH/PBST, 1× 50% MetOH/PBST, 1× 25% MetOH/PBST, 2× PBST), bleached in a 6% H_2O_2/PBST solution (10 min for E8.5, 20 min for E9.5, 30 min for E10.5, 45 min for E11.5), and washed 3× in PBST. The specimens were digested with 10 μg/ml proteinase K/PBST (7 min for E8.5, 10 min for E9.5, 13 min for E10.5, 17 min for E11.5) in order to allow for better penetration of the probe later. The digestion process was stopped by an incubation with 2 mg/ml glycine/PBST solution followed by two washes with PBST. The embryos were refixed in 0.2% glutaraldehyde/4% PFA/PBST for 30 min at RT while rolling, washed twice with PBST at RT, and preincubated with hybridization solution (50% formamide, 5× SSC pH 5.0, 1% SDS, 0.05 μg/ml yeast RNA

(Sigma-Aldrich), 0.05 μg/ml heparin (Sigma-Aldrich), in RNase-free H_2O) for 15 min at RT. The solution was exchanged with fresh hybridization solution, and the embryos were prehybridized for 2 h at 68 °C in order to reduce unspecific background staining. Prehybridized embryos were either directly used for hybridization or stored at -20 °C in hybridization solution.

Preparation of the *Slitl2*-specific probe The *Slitl2*-specific probe was prepared using the pKS-Slitl2 plasmid provided by Dr. Heinrich Schrewe (Institute for Medical Genetics, Charité University Medicine, Berlin, Germany). This plasmid harbors a 1.8 kb-long fragment of the Slitl2 cDNA sequence introduced into the vector pBluescript II KS (Stratagene) with an *EcoR*I at the 5' end and an *Xho*I site at the 3' end. The 5' and the 3' end of the insert are flanked by T3 and T7 RNA polymerase promoters, respectively. These promoters allow for transcription of downstream cloned DNA by the corresponding RNA polymerase. At first, the plasmid was linearized. Therefore, 3 μg plasmid were digested for 3 h at 37 °C with 2 μl *EcoR*I (12 U/μl; Roche) in a 50 μl reaction mix containing 1× SuRE/Cut Buffer H (Roche). Following the incubation, 16 μl 10 M ammonium acetate and 160 μl ice-cold 100% EtOH were added, the sample was mixed and spun down at 16,100 × g for 30 min at 4 °C. The supernatant was discarded, 200 μl ice-cold 70% EtOH added, and the pellet was again spun down at 16,100 × g for 15 min at 4 °C. The supernatant was taken off, and the precipitated plasmid was air-dried in a fume hood before dissolving it in 38.5 μl RNase-free H_2O. An *in vitro* transcription mix was set up as follows: 38.5 μl linearized plasmid, 6 μl 10 × transcription buffer (Roche), 6 μl ACG nucleotide mix (each 4 mM; Roche), 1.5 μl digoxigenin-UTP (dig-UTP) mix (4 mM, Roche), 3 μl DTT (200 mM), 2 μl RNase inhibitor (40 U/μl; Peqlab), and 3 μl T7 RNA polymerase (20 U/μl; Roche) were mixed and incubated for 2.5 h at 37 °C. Following the incubation, the template DNA was digested with 6 μl RNase-free DNase I (10 U/μl; Roche) for 15 min at 37 °C. The probe RNA was precipitated by adding 2.4 μl glycogen, 24 μl 10 M ammonium acetate, and 300 μl ice-cold 100% EtOH before spinning it down at 16,100 × g for 30 min at 4 °C. The supernatant was removed, 300 μl ice-cold 70% EtOH added, the pellet again centrifuged at 16,100 × g for 15 min at 4 °C. The pellet was air-dried in a fume hood and dissolved in 60 μl hydrolysis buffer (40 mM $NaHCO_3$, 75 mM Na_2CO_3; pH 10.2) in order to reduce the probe size to allow better penetration of the embryonic tissues. The reaction was incubated for 4 min at 60 °C, and the RNA pellet was again precipitated as above but with-

out the addition of glycogen. The final pellet was dissolved in 50 μl RNase-free H_2O. 3 μl were taken off for documentation on a 1% (w/v) agarose gel, and the remaining 47 μl were stored at -20 °C.

Hybridization The required number of wells from a 12-well plate (Corning®) were filled with 2 ml preheated hybridization solution (68 °C). A clean netwell (15 mm diameter, 74 μm mesh; Corning®) was placed in each well, and the prehybridized embryos were sorted into the wells. The embryos were prewarmed to 68 °C for 30 min. Meanwhile, a fresh 12-well plate with 2 ml hybridization solution containing 23.5 μl of hydrolyzed probe per well was prepared. The probes were denatured at 80 °C for 10 min by placing the plate inside a sealed plastic box in a hot water bath. Right after denaturation, the netwells with the embryos were transferred to the plate containing the probes. The plate was placed inside a humid plastic box and incubated o/n in an oven with rocking function (BFED 053; Binder) at 68 °C for hybridization of the probe to its complementary mRNA.

Antibody incubation The netwells were transferred back to a 12-well plate filled with pure hybridization solution and incubated at 68 °C for 30 min. The netwells were transferred into a netwell reagent tray (Corning®) and washed twice at 68 °C for 30 min with approximately 90 ml of preheated Solution 1 (50% formamide, 5× SSC pH 5.0, 1% SDS) followed by two washes for 30 min and two washes for 60 min at 68 °C with Solution 3T (50% formamide, 2× SSC pH 5.0, 0.1% Tween-20) inside a humified box. The box was removed from the oven, and the embryos were washed three times with TBST for 15 min at RT. During the washing procedure, the antibody solution was prepared as follows: 6 ml TBST were mixed with a pinch of embryo powder (for preparation of the embryo powder: see below) and heat-inactivated for 30 min at 70 °C in a waterbath. After cooling the solution on ice, 60 μl heat-inactivated lamb serum (Gibco) and 12.5 μl of α-dig-AP antibody (Roche) were added, and the solution was incubated at 4 °C for at least 1 h rolling in the dark in order to preabsorb the antibody. The solution was spun down at 1,500 × g for 10 min at 4 °C, and the supernatant was transferred into a tube containing 19 ml 1% lamb serum/TBST and mixed well. The antibody solution was stored at 4 °C in the dark until use. Following the last washing steps, the embryos were blocked in a fresh 12-well plate filled with 2 ml 10% lamb serum/TBST per well for 2-3 h at RT. The embryos were then transferred to a fresh 12-well plate containing 2 ml antibody solution per well and incubated o/n rocking at 4 °C in the dark. The next day, the embryos

were washed twice for 15 min, twice for 30 min, and at least six times for 1 h at RT in the dark with approximately 90 ml TBST. To reduce background staining, the specimens were incubated o/n at 4 °C in TBST in the dark.

Staining The next day, the embryos were washed four times at RT for 15 min with 90 ml freshly prepared NTMT (100 mM Tris-HCl pH 9.5, 100 mM NaCl, 50 mM $MgCl_2$, 0.1% Tween-20). Meanwhile, the staining solution was prepared. Therefore, 112.5 μl NBT (75 μl/μg; Roth) and 87.5 μl BCIP (50 μg/μl; Roth) were added to 25 ml ice-cold NTMT. The solution was filter-sterilized using a 0.45 μm syringe filter (Schleicher&Schuell) before filling 2 ml of it into the wells of a fresh 12-well plate. The embryos were then transferred into the staining solution and incubated rocking in the dark at RT. The staining intensity was monitored periodically under a binocular. Once an appropriate staining was obtained, the reaction was stopped by washing the embryos once in NTT (100 mM Tris-HCl pH 9.5, 100 mM NaCl, 0.1% Tween-20) and several times in PBST at RT. The stained embryos were postfixed in 4% PFA/PBST and stored in the dark at 4 °C.

Imaging Whole-mount specimens were photographed with a SteREO Discovery.V12 microscope (Zeiss) and an AxioCam Color camera (Zeiss) using the AxioVision 4.6 software (Zeiss).

Preparation of mouse embryo powder Approximately 25 mouse embryos of the stages E12.5-E14.5 were homogenized in a minimum volume of ice-cold PBS using a tissue homogenizer (T8 Ultra-Turrax®; IKA-Werke). 4 vol. ice-cold acetone were added, the solution was mixed and incubated on ice for 30 min. The solution was then centrifuged at 10,000 × g for 10 min at 4 °C, the supernatant was removed, and the pellet washed with ice-cold acetone and again spun down. The pellet was spread out and ground into a fine powder on a sheet of filter paper. The powder was air-dried and stored at 4 °C.

2.4.3 X-gal staining

The X-gal staining procedure followed the basic protocol described in [Nagy, 2003].

2.4.3.1 Whole-mount specimens

Staining Mice were euthanized via cervical dislocation. Embryos were dissected in cold PBS and immediately transferred into ice-cold 4% PFA/PBS as were tissue specimens. The samples were fixed for 1 h at 4 °C, rinsed three times with rinse buffer (5 mM EGTA, 0.01% deoxycholate, 0.02% NP40, 2 mM $MgCl_2$, in PBS) for 15 min at RT. Meanwhile, the staining buffer was prepared containing 5 mM potassium ferricyanide (Merck), 5 mM potassium ferrocyanide (Merck), 5 mM EGTA, 0.01% deoxycholate, 0.02% NP40, 2 mM $MgCl_2$ in PBS. X-gal (40 mg/ml in dimethylformamide) was added to a final concentration of 1 mg/ml, and the solution was filtered using a Steritop™ filter (Millipore). The specimens were then incubated in staining buffer at 37 °C in the dark until an appropriate staining was obtained. After staining, the specimens were washed three times for 5 min at RT and postfixed o/n in 4% PFA/PBS at 4 °C. They were either stored as whole-mounts in 4% PFA/PBST at 4 °C or further processed for sectioning.

Paraffin-embedding and sectioning The next day, excess fixative was removed by two washes with PBS before manually processing them through a graded ethanol series: 30%, 50%, 70% EtOH, each for 15 min at 4 °C. The specimens were then automatically infiltrated by paraffin, embedded in metal molds, and sectioned on a rotary microtome. The detailed protocol for these procedures is described above (subsection 2.4.1). The sections were counterstained in eosin for 1 min (Eosin Y Solution; Sigma-Aldrich), briefly dipped in ddH_2O, dehydrated (dip into 90% EtOH, 100% EtOH 2× for 5 min, xylene 1× for 5-10 min), immediately mounted in Entellan® (Merck), and covered with glass cover slips (Roth).

2.4.3.2 Cryo sections

Cryo embedding and sectioning Since penetration of the staining substrate was insufficient in embryos older than E11.5, they were first embedded, sectioned, and then stained. Embryos were dissected in cold PBS and directly embedded in plastic molds (Peel-A-Way®; Polysciences) with Tissue-Tek® OCT compound (Ted Pella) after removing excess PBS by blotting it on a paper towel. The

specimens were placed in the center of the mold filled with freezing compound and frozen on a metal block cooled with dry ice and EtOH. This method – as opposed to paraffin embedding – preserved the β-galactosidase enzyme activity. Frozen blocks were stored at -20 °C until sectioning. 14-20 μm-thick sections were cut on a cryotome (CryoStar HM 560 M; MICROM) and transferred onto adhesion microscope slides (SuperFrost®; Menzel). The sections were dried on a 30 °C heating plate for 30 min and stored at -20 °C in a sealed, desiccated plastic box.

Staining After storage, the slides were allowed to warm to RT inside the sealed box. The sections were postfixed on ice in 1% PFA/PBS for 10 min before quickly rinsing and then washing them on ice in cold 2 mM $MgCl_2$/PBS for 10 min on a shaker. After two washes with cold rinse buffer (subsubsection 2.4.3.1) for 10 min, the slides were incubated o/n in the dark at 37 °C in staining buffer (subsubsection 2.4.3.1). The next day, the sections were washed three times in 2 mM $MgCl_2$/PBS for 5 min at RT, rinsed in ddH_2O for 5 min, counterstained, dehydrated, and mounted as above (subsubsection 2.4.3.1).

2.4.3.3 Bone sections

In order to cut and stain bone specimens, the tissue had to be decalcified. Therefore, the surrounding soft tissue was removed, and the bones were decalcified in OSTEOSOFT® solution (Merck) o/n rolling at RT. The next day, the bones were incubated in Tissue-Tek® OCT compound (Ted Pella) for 1 h at 4 °C before embedding them in molds filled with freezing compound on a metal block cooled with dry ice and EtOH. 8 μm-thick sections were cut and stained as above (subsubsection 2.4.3.2).

Imaging Whole-mount specimens and tissue sections were photographed as described under subsection 2.4.2 and subsection 2.4.1, respectively.

2.4.4 Immunohistochemistry

For this assay, formalin-fixed, paraffin-embedded tissue sections were used (subsection 2.4.1). They were deparaffinized in xylene (3× for 5 min) and rehydrated (100% EtOH, 2× for 5 min; 90% EtOH, 80% EtOH, ddH_2O, each once for 5 min). The slides were then incubated in 1% H_2O_2 for 10 min at RT in order to quench endogenous peroxidase activity. The sections were washed three times for 5 min

in PBS before unmasking the epitopes. Therefore, the slides were boiled in a glass beaker for 20 min containing a buffer with either moderately acidic pH (pH 6.0, 10 mM sodium citrate; pH adjusted with 1 M citric acid) or basic pH (pH 9.0, 10 mM Tris, 1.25 mM EDTA). After this heat-induced antigen retrieval, the glass beaker was placed in an ice bucket, and the buffer was cooled down to approximately 40 °C. The slides were washed 3× for 5 min in PBS and blocked o/n at 4 °C with 2.5% horse serum (ImmPRESS™ REAGENT kit; Vector Laboratories). The next day, the sections were incubated with the primary antibody diluted in 2.5% horse serum for 2 h at RT inside a humified chamber. Uncoupled antibody was removed by five washes in PBS for 5 min. The sections were then incubated with ImmPRESS™ reagent for 60 min at RT; depending on the species that the primary antibody was raised in, this was either the anti-mouse Ig or the anti-rabbit Ig reagent. These reagents contain micropolymers of a very active peroxidase coupled to affinity purified secondary antibodies. The slides were washed three times for 3 min in PBS and incubated for 15 min at RT in peroxidase substrate solution (Vector® NovaRED™; Vector Laboratories). The slides were rinsed in tap water at RT for 5 min before counterstaining them for 5 sec in hematoxylin (Mayer's Hematoxylin Solution; Sigma-Aldrich). The sections were again rinsed in tap water for 5 min, dehydrated (dip into 90% EtOH, 100% EtOH 2× for 5 min, xylene once for 5-10 min), immediately mounted in Entellan® (Merck) and covered with glass cover slips (Roth). Table 2.12 lists all primary antibodies with their respective dilutions, the pH of the buffer used for antigen retrieval, and the ImmPRESS™ secondary antibody reagent.

1° Antibody	**Supplier**	**Dilution**	**Retrieval**	**ImmPRESS™**
α-GFP (11 814 460 001)	Roche	1:100	pH 9.0	α-mouse
α-GFP (A111222)	Invitrogen	1:100	pH 6.0	α-rabbit
α-Desmin (ab8470)	abcam	1:100	pH 9.0	α-mouse
α-PECAM-1 (sc-1506)	Santa Cruz	1:100	pH 6.0	α-rabbit
α-WT1 (M3561)	Dako	1:50	pH 9.0	α-mouse

Table 2.12 Antibodies used for immunohistochemistry

Imaging Tissue sections were photographed as described under subsection 2.4.1.

2.4.5 Immunocytochemistry

Mouse primary embryonic fibroblasts (subsection 2.2.6) were grown to confluency in a 10 cm cell culture dish containing gelatin-coated round glass cover slips (12 mm; Roth). The cover slips were carefully transferred into the wells of a 24-well plate (Corning®) and washed twice with PBS. The cells were fixed with 4% PFA/PBS at RT for 15 min. Following two washes with PBS, the cells were permeabilized with 0.5% Triton X-100/PBS for 5 min at RT. The cells were again washed twice with PBS and blocked with DMEM (Lonza) supplemented with 10% fetal calf serum (FCS; Invitrogen) for 30 min at RT. The cells were then incubated with the primary antibody (α-Slitl2, diluted 1:200 in DMEM/10% FCS) for 1 h at RT. After two washes with PBS, incubation with the secondary antibody (Cy3-conjugated α-rabbit, 711-166-152; Jackson ImmunoResearch) diluted 1:10,000 in DMEM/10% FCS for 1 h at RT followed. The cells were again washed twice with PBS, and the nuclei stained with 0.2 μg/ml DAPI (Sigma-Aldrich) in PBS for 2 min at RT before a final wash with PBS. The cover slips were mounted upside down onto microscope slides (SuperFrost®; Menzel) using Immu-Mount™ mounting media (Thermo Scientific) and stored in the dark.

Imaging The cells were photographed using an Observer.Z1 microscope (Zeiss) and the AxioVision 4.6 software (Zeiss).

2.4.6 Electron microscopy

The procedures for the electron microscopy study were performed by Beatrix Fauler (Max Planck Institute for Molecular Genetics, Berlin, Germany). Briefly, fresh kidney samples were prefixed for 1.5 h in 2% PFA/2% glutaraldehyde in 50 mM sodium cacodylate buffer (SERVA) and postfixed o/n in 2.5% glutaraldehyde/50 mM sodium cocodylate buffer at 4 °C. The samples were washed several times in sodium cacodylate buffer before incubating them for 2 h in 0.5% osmium tetroxide/50 mM sodium cacodylate buffer. The specimens were washed several times in ddH_2O and incubated in 0.1% tannic acid/100 mM HEPES buffer for 1 h at RT. The samples were again washed in ddH_2O and incubated in 2% uranyl acetate for 1.5 h at RT. They were dehydrated in a graded ethanol series, then processed via propylene oxide into resin (Low Viscosity 'Spurr' Kit; Ted Pella), and polymerized at 60 °C for 3 days. Ultrathin sections (70 nm) were cut and mounted on electron microscopic grids. The sections were counterstained with

uranyl acetate and lead citrate. The samples were examined and photographed with a FEI 120 kV Tecnai transmission electron microscope.

2.4.7 Skeleton staining

The procedure followed the protocol described in [Kessel et al., 1990]. Mice were euthanized by CO_2 inhalation. The skin and all visceral organs were removed before fixing the carcasses for four days in 100% EtOH at RT on a roller mixer. They were incubated in 100% acetone for three days, rinsed in water, and incubated in staining solution (1 vol. 0.3% Alcian Blue 8 GX (Sigma-Aldrich) in 70% EtOH, 1 vol. 0.1% Alizarin Red S (Sigma-Aldrich) in 95% EtOH, 1 vol. 100% acetic acid, 17 vol. 100% EtOH) for 10 days on a roller mixer. Excess soft tissue was removed by incubation with Clearing Solution (20% glycerol, 1% KOH). For storage, the specimens were transferred into 50%, 80%, and finally 100% glycerol.

2.4.8 Micro-computed tomography

Micro-computed tomography (μCT) was performed by Dr. Marco Eijken (Erasmus Medical Center, Rotterdam, The Netherlands). Bone samples of 25-day-old male mice were collected and fixed in 2% PFA/PBS. Surrounding soft tissue was removed, and the specimens were scanned using the SkyScan 1072 microtomograph scanner (SkyScan, Kontich, Belgium). Three-dimensional images were reconstructed with a 3D data analysis software (CTAnalyzer; SkyScan, Kontich, Belgium).

2.5 Evaluation of clinical laboratory parameters

2.5.1 Blood parameters

All samples were collected via exsanguination by puncture of the retroorbital sinus after anesthetizing the animals with isoflurane (Baxter).

2.5.1.1 Complete blood count

Blood was collected in standard 1.0 ml EDTA collection tubes (KABE). All parameters were evaluated at the Institut für Veterinärmedizinische Diagnostik (Berlin, Germany) using the Sysmex XT-2000iV hematology analyzer by combined laser-based flow cytometry and impedance technology.

2.5.1.2 Serum urea and serum calcium

The samples were allowed to clot at RT. The serum was collected after centrifugation at 100 × g for 15 min at 4 °C. All parameters were evaluated at the Institut für Veterinärmedizinische Diagnostik (Berlin, Germany) using the cobas c 501 module of the cobas® 6000 analyzer series (Roche).

2.5.1.3 Serum corticosterone

Corticosterone was measured with an enzyme-linked immunosorbent assay (Corticosterone ELISA Kit, RE52211; IBL). The samples were allowed to clot at RT. The serum was collected after centrifugation at 100 × g for 15 min at 4 °C and stored at -20 °C until further use. For the ELISA assay, 1 part Enzyme Conjugate (250×) was mixed with 250 parts Enzyme Diluent. The samples were diluted 1:10 with Standard 0 solution. 20 μl of each standard and samples were dispensed in technical triplicates into the plate wells coated with anti-Corticosterone antibody. 200 μl Enzyme Conjugate were added to each well. The contents were thoroughly mixed on a plate shaker for 10 sec before incubating the plate for 1 h at RT. The content of the wells was removed by inverting the plate, and the wells were washed three times with diluted Wash Solution (1:40 dilution with ddH_2O). 100 μl Substrate Solution were dispensed into each well, and the plate was incubated for 15 min at RT. The enzymatic reaction was stopped by adding 50 μl Stop Solution per well. The optical density (OD) was read at 450 nm within 10 min using a GloMax® luminometer (Promega). A standard curve was generated based on a 4-parameter logistic curve fit using the online available program 'gnuplot' (http://www.gnuplot.info/), and sample concentrations were calculated thereof.

2.5.1.4 Serum vitamin D

The samples were allowed to clot at RT. The serum was collected after centrifugation at 100 × g for 15 min and stored at -20 °C. 1,25-dihydroxycholecalciferol levels were evaluated at the Erasmus Medical Center (Rotterdam, The Netherlands) using the Gamma-B 1,25-dihydroxyvitamin D RIA (IDS, Boldon, UK) according to the manufacturer's instructions. Cross-reactivity with the inactive precursor, 25-hydroxvitamin D, is 0.001% for this test.

2.5.1.5 Serum albumin

The samples were allowed to clot at RT. The serum was collected after centrifugation at 2,000 × g for 10 min at 4 °C and stored at -20 °C until further use. Serum albumin values were evaluated with the competitive AssayMax Mouse Albumin ELISA Kit (Assaypro; EMA2201-1). All standard dilutions were prepared according to the manufacturer's instructions, and the samples were diluted 1:8,000 with MIX Diluent before transferring 25 μl of standards and samples – all in technical duplicates – into the wells of the coated Mouse Albumin Microplate. 25 μl Biotinylated Mouse Albumin Antibody were immediately added to each well. The plate was incubated for 1 h at RT, and the wells were washed five times with 200 μl Wash Buffer. 50 μl Streptavidin-Peroxidase Conjugate were pipetted into each well, and the plate was again incubated for 30 min at RT. The wells were washed as above before adding 50 μl Chromogen Substrate per well, and the plate was incubated for 8 min at RT. 50 μl Stop Solution were added per well, and the optical density (OD) was immediately read at 450 nm using a GloMax® luminometer (Promega). A standard curve was generated based on a 4-parameter logistic curve fit using the online available program 'gnuplot' (http://www.gnuplot.info/), and sample concentrations were calculated thereof.

2.5.2 Urinary parameters

2.5.2.1 SDS-PAGE urinalysis

Urinary proteins were detected by SDS-PAGE and subsequent staining with PageBlue™ Protein Staining Solution (Fermentas). Urine was collected by restraining the mouse with one hand and gently pressing the thumb of the other hand against the lower abdomen. 2 μl urine were diluted in 13 μl buffer (10 mM Tris-HCl pH 8.0, 2.5 mM $MgCl_2$, 5 mM EGTA pH 8.0). 5 μl 4× NuPAGE® LDS Sample Buffer (Invitrogen) were added, and the proteins were denatured for 10 min at 70 °C, then put on ice. The samples were loaded into the wells of a precast NuPAGE® 10% Bis-Tris gel and electrophoretically separated as above (subsection 2.3.4). Residual SDS was removed by rinsing the gel in ddH_2O. The proteins were visualized by incubating the gel in PageBlue™ Protein Staining Solution (Fermentas) for 1 h at RT on a shaker. Excess staining solution was removed by washing the gel o/n at RT in ddH_2O on a shaker.

2.5.2.2 Urinary calcium

Urine was collected in a tube by gently pressing one thumb against the abdomen. The collected sample was centrifuged at 800 × g for 5 min and stored at -20 °C until further use. Urinary calcium was measured using the QuantiChrom Calcium Assay Kit™ (DICA-500; Gentaur). Standard dilutions were prepared according to the manufacturer's instructions. 5 μl diluted standards and 5 μl undiluted urine – all in technical duplicates – were transferred into the wells of a clear-bottomed 96-well plate (ELISA microplate; Greiner). 200 μl working reagent (1:1 Reagent A:Reagent B) were added to each well, and the plate was incubated for 3 min at RT. The optical density (OD) was immediately read at 600 nm using a GloMax® luminometer (Promega). A standard curve was prepared using a linear regression curve fit, and sample concentrations were calculated thereof.

2.5.2.3 Urinary creatinine

Urinary creatinine values were evaluated with the Parameter™ kit (R&D Systems) according to the manufacturer's instructions. Briefly, standard dilutions were prepared as instructed, and 50 μl of each standard and each sample (diluted 1:10 with ddH_2O) – all in technical duplicates – were pipetted into the wells of a clear-bottomed 96-well plate (ELISA microplate; Greiner). 100 μl of Alkaline Picrate Solution were added, and the plate was incubated for 30 min at RT. The optical density (OD) was read at 450 nm using a GloMax® luminometer (Promega). A standard curve was generated based on a 4-parameter logistic curve fit using the online available program 'gnuplot' (http://www.gnuplot.info/), and sample concentrations were calculated thereof.

2.5.2.4 Urinary albumin

Urinary albumin values were evaluated with the AssayMax Mouse Albumin ELISA Kit (Assaypro; EMA3201-1). All standard dilutions were prepared according to the manufacturer's instructions, and the samples were diluted 1:100 with MIX Diluent before transferring 50 μl of standards and samples – all in technical duplicates – into the wells of the coated Mouse Albumin Microplate. The plate was sealed and incubated for 2 h at RT. The wells were washed five times with 200 μl Wash Buffer, and 50 μl Biotinylated Mouse Albumin Antibody were added to each well. All subsequent procedures are described under subsubsection 2.5.1.5.

Statistics Data are represented as median ±IQR (interquartile range). The non-parametric Mann–Whitney U test, also known as Wilcoxon rank-sum test, was used to determine the two-tailed level of significance (P-value) between samples from wild-type and knock-out, i.e., *Slitl2*-deficient mice with the online available program utest (http://elegans.swmed.edu/ leon/stats/utest.html). P-values of ≤ 0.05 were considered statistically significant.

2.6 General buffers, solutions, and chemicals

General buffers and solutions

Name	Composition
Gel loading buffer, 6×	1× TAE, 60 mM EDTA pH 8.0, 50% glycerol, 0.1% bromophenol blue
MOPS buffer, 10×	200 mM MOPS, 50 mM sodium acetate, 10 mM EDTA
PBS(T)	137 mM NaCl, 2.7 mM KCl, 10 mM Na_2HPO_4, 1.8 mM KH_2PO_4, (0.1% Tween-20)
SSC, 20×	300 mM trisodium citrate dihydrate, 3 M NaCl, pH adjusted with 1 M citric acid
TAE, 50×	2 M Tris, 950 mM acetic acid, 62.5 mM EDTA
TBE, 50×	4.5 M Tris, 4.5 M boric acid, 125 mM EDTA
TBS(T)	140 mM NaCl, 2.7 mM KCl, 25 mM Tris-HCl pH 7.5, (0.1% Tween-20)
TE	10 mM Tris-HCl pH 8.0, 1 mM EDTA pH 8.0
Tris-HCl	1 M Tris, pH adjusted with HCl (37%)

Table 2.13 General buffers and solutions

General chemicals

Name	Supplier
Acetic acid (100%)	Merck
Acetone	Merck
Ammonium acetate	Merck
Boric acid	Merck
Chloramphenicol	Sigma-Aldrich
Chloroform	Roth
Citric acid	Merck
DMSO	Sigma-Aldrich
DTT	Sigma-Aldrich

EDTA	Sigma-Aldrich
EGTA	Roth
Ethanol	Merck
Ethidium bromide (10%)	Roth
Formaldehyde (37%)	Fluka
Formalin (10%)	Sigma-Aldrich
Formamide	Merck
Glutaraldehyde	Sigma-Aldrich
Glycerol	Merck
Glycine	Merck
Glycogen	Peqlab
HCl (37%)	Merck
HEPES	Sigma-Aldrich
H_2O_2 (30%)	Roth
Isopropanol	Merck
Kanamycin	Sigma-Aldrich
KCl	Sigma-Aldrich
KOH	Merck
Methanol	Merck
$MgCl_2$	Roth
MOPS	Sigma-Aldrich
NaCl	Merck
Na_2HPO_4	Sigma-Alrich
NaOH	Merck
Phenol	Roth
SDS	Fluka
Sodium acetate	Sigma-Aldrich
Tris	Sigma-Aldrich
Trisodium citrate dihydrate	Merck
Triton X-100	Sigma-Aldrich
Tween-20	Sigma-Aldrich
X-gal	Roth
Xylene	Roth

Table 2.14 General chemicals

3 Results

3.1 *Slitl2* expression pattern

Three different strategies were pursued in order to describe a detailed temporospatial expression pattern of *Slitl2* during various stages of pre- and postnatal development of the mouse. First, endogenous gene expression was assessed. Therefore, *Slitl2* RNA was detected both by Northern blot analysis and whole-mount *in situ* hybridization (WISH). In addition, an antibody was generated to detect endogenous Slitl2 protein by immunocytochemistry. Secondly, a *Slitl2-LacZ* knock-in reporter mouse strain was produced to visualize *Slitl2* expression domains via β-galactosidase activity. Thirdly, *Slitl2-Venus* transgenic mice harboring a modified bacterial artificial chromosome (BAC) construct were generated. In these mice, *Slitl2* expression is mirrored by the expression of Venus, a variant of the yellow fluorescent protein (YFP).

3.1.1 Endogenous *Slitl2* expression

3.1.1.1 RNA expression

Northern blot analysis The Northern blot technique is used to study the RNA expression pattern of a particular gene and allows for comparison of expression levels between different developmental stages or tissues. To analyze endogenous *Slitl2* expression, total RNA was isolated from wild-type embryos and various adult tissues. 10 μg RNA were precipitated, electrophoretically separated on a denaturing formaldehyde gel, and blotted onto a nylon membrane. RNA was detected by hybridization with a *Slitl2*-specific probe binding to its 3' untranslated region (3' UTR). To control and correct sample variability, the same membranes were subsequently hybridized with a probe specifically detecting the RNA of a housekeeping gene, namely glyceraldehyde-3-phosphate dehydrogenase (*Gapdh*).

Endogenous *Slitl2* RNA expression was detected as early as embryonic day 8.5 (E8.5). Its expression gradually increased during the following stages of embryonic development (E9.5 to E13.5) and remained at high levels also during fetal

stages of development (E14.5 and E15.5) (Figure 3.1 A). Strong expression was detected in placental tissue as well as in adult testis. Lung, uterus, and kidney displayed moderate expression of *Slitl2* RNA. Weak expression could be observed in heart, liver, and spleen tissue, while *Slitl2* RNA was virtually absent in brain, thymus, and muscle tissue (Figure 3.1 B).

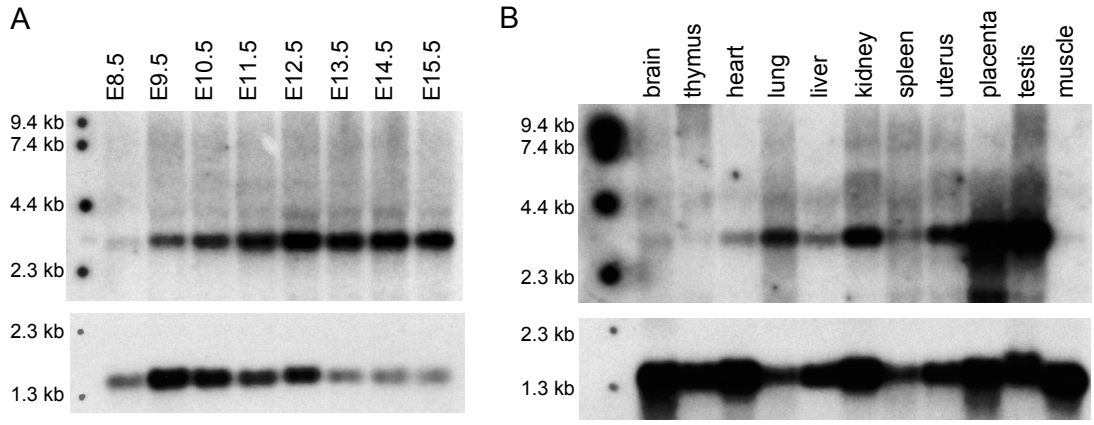

Figure 3.1 Northern blot analysis of *Slitl2* expression of embryonic stages and adult tissues **A**. Northern blot of 10 μg of total RNA prepared from whole mouse embryos at different stages of embryonic development (E8.5 to E15.5). **B**. Northern blot of 10 μg of total RNA prepared from various indicated adult mouse tissues. *Slitl2* RNA was detected as a single band at $\sim$3.2 kb (top). The same membranes were hybridized with a probe detecting *Gapdh* RNA expression as loading control (bottom).

Whole-mount *in situ* hybridization Whole-mount *in situ* hybridization (WISH) enables direct visualization of the expression pattern of a gene of interest within embryos. This technique is based on the formation of stable hybrids between an mRNA strand and a complementary, digoxigenin-labeled probe and the subsequent indirect detection of these hybrids. Owing to low penetration efficiency of the probe through the skin, this procedure is only suitable for embryos staged E11.5 and younger.

For *in situ* analysis of endogenous *Slitl2* expression, wild-type embryos were incubated with a digoxigenin-labeled *Slitl2*-specific probe. The labeled hybrids were detected with an alkaline phosphatase (AP)-coupled anti-digoxigenin antibody, and binding of the antibody was visualized via an AP-catalyzed color reaction. An early E8.5 embryo revealed staining of the head mesenchyme, the lateral mesoderm, and the neural tube at the midline, while the cranial neural folds, the developing heart, and the somites were clearly devoid of staining (Figure 3.2 A). By E9.0, additional expression became evident in the developing first branchial arch mesenchyme and in the roof plate of the neural tube (Figure 3.2 B). At E9.5 and E10.0, the emerging forelimb buds were clearly demarcated by *Slitl2* expression. Besides, the floor plate of the developing midbrain displayed expression as did the developing gut including the septum transversum, the lining of the coelomic cavity, and, as already observed in earlier stages, the head mesenchyme and the branchial arches revealed staining (Figure 3.2 C and D). By E10.5 and E11.0, the hindlimb buds in addition to the forelimb buds showed strong staining. Consistent with earlier stages, the head mesenchyme and the mesenchyme of the branchial arches exhibited *Slitl2* expression, whereas the neural epithelium, the developing heart, and the somites appeared unstained (Figure 3.2 E). By E11.0, *Slitl2* expression in the precartilaginous sclerotomic condensations became evident along both sides of the neural tube (Figure 3.2 F). The strong staining of the otic pit, which was observed from E10.0 onwards, was attributed to accumulation of unbound probe and therefore considered background.

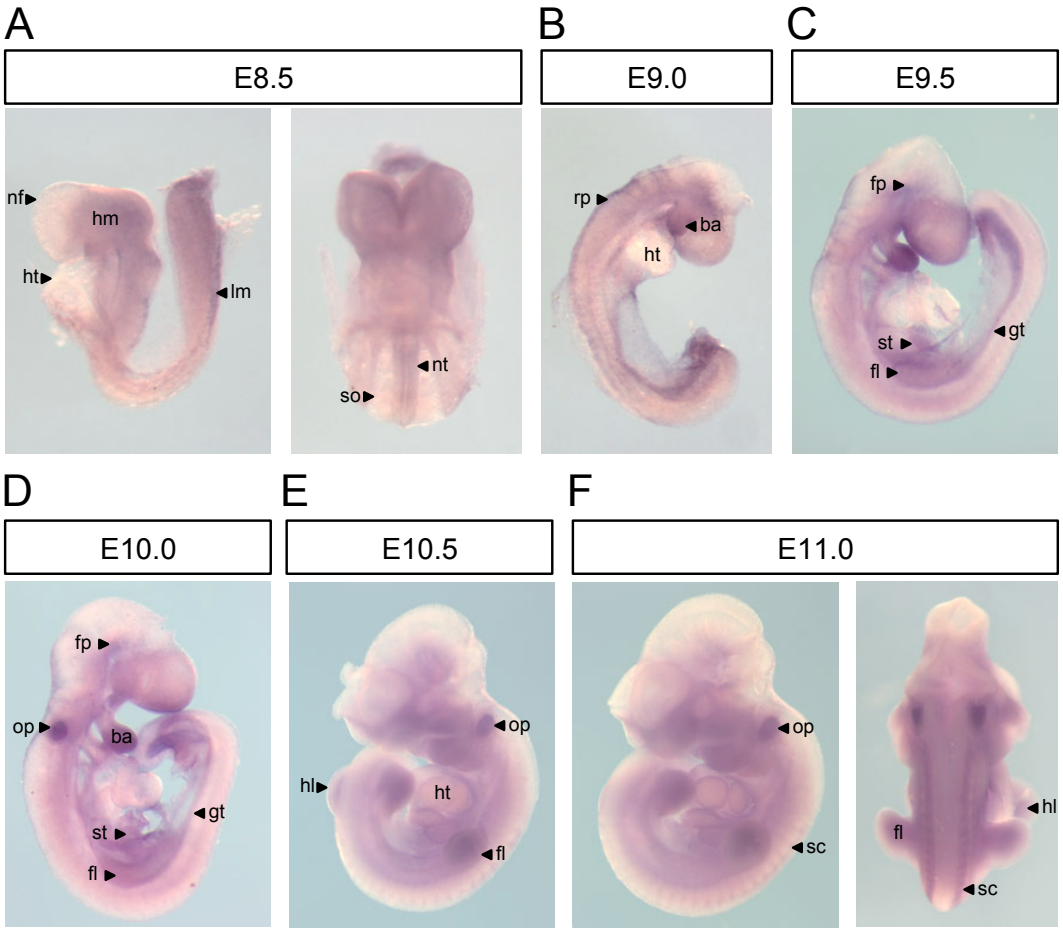

Figure 3.2 *Slitl2* whole-mount *in situ* hybridization from embryonic day 8.5 (E8.5) to E11.0
A. E8.5 (right: frontal view)
B. E9.0
C. E9.5
D. E10.0
E. E10.5
F. E11.0 (right: dorsal view)
ba, branchial arch;
fl, forelimb bud;
fp, floor plate;
gt, gut;
hl, hindlimb bud;
hm, head mesenchyme;
ht, heart;
lm, lateral mesoderm;
nf, neural fold;
nt, neural tube;
op, otic pit;
rp, roof plate;
sc, sclerotomic condensation;
so, somite;
st, septum transversum

3.1.1.2 Protein expression

To analyze endogenous Slitl2 protein expression, a polyclonal antibody was generated by Pineda Antibody Service (Berlin, Germany). An epitope of 14 amino acids (aa) corresponding to the murine Slitl2 carboxy-terminal sequence (aa 660-673 corresponding to aa sequence GPSLQGVLPAKHYI) was selected. Based on the presence of several positively charged amino acids, antibodies directed against this epitope were predicted to have a high binding capacity. Rabbits were immunized with the peptide, and sera were collected 130 days later. The antibody was affinity-purified by the supplier prior to delivery.

To determine the intracellular localization of the Slitl2 protein, mouse primary embryonic fibroblasts (MEFs) were generated from wild-type and heterozygous *Slitl2*$^{+/-}$ embryos. In addition, MEFs generated from homozygous *Slitl2*$^{-/-}$ embryos were included in this assay as a negative control. All three cell lines were subjected to immunocytochemical analysis using the α-Slitl2 antibody. Binding of the antibody was detected by a fluorochrome-labeled secondary antibody. Fluorescence microscopy identified Slitl2 protein scattered over the entire cell surface in the wild-type and heterozygous *Slitl2*$^{+/-}$ cell lines. However, due to non-specific binding of the antibody, faint signal could also be observed in cells lacking *Slitl2* expression, i.e., in MEFs derived from a *Slitl2*$^{-/-}$ embryo, when applying the same exposure conditions (Figure 3.3).

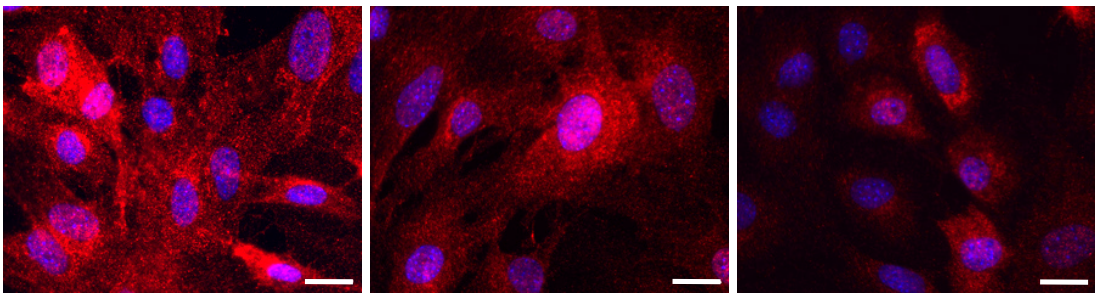

Figure 3.3 Immunocytochemical analysis of Slitl2 protein expression
Wild-type (left) and heterozygous *Slitl2*$^{+/-}$ (middle) mouse primary embryonic fibroblasts (MEFs) were subjected to immunocytochemical analysis using the polyclonal α-Slitl2 antibody. Slitl2 protein was detected over the entire cell surface in both cell lines (red). Nuclei were stained with DAPI (blue). Homozygous *Slitl2*$^{-/-}$ MEFs served as negative control. Due to non-specific binding of the antibody, faint signal was also observed in these cells when applying the same exposure conditions (right). (Scale bar: 20 μm)

3.1.2 *Slitl2-LacZ* expression

3.1.2.1 Generation of *Slitl2-LacZ* mice

For a more detailed analysis of *Slitl2* expression domains, a *Slitl2-LacZ* knock-in reporter mouse strain was generated. The bacterial LacZ gene encodes β-galactosidase. This enzyme cleaves the colorless substrate X-gal, thereby yielding galactose and 5-bromo-4-chloro-3-hydroxyindole, which subsequently oxidizes to form an insoluble blue precipitate. The construct used for targeting the *Slitl2* locus in G4 embryonic stem (ES) cells [George et al., 2007] comprised a *loxP*-flanked neomycin (neo) selection cassette in the *Slitl2* intronic sequence just upstream of the splice acceptor (SA) site and a LacZ open reading frame (ORF) with a nuclear localization signal (LacZ-NLS) (Figure 3.4 A). The *Slitl2* coding sequence had been replaced by the LacZ open reading frame, thus placing the bacterial gene under transcriptional control of the endogenous *Slitl2* regulatory elements after successful knock-in into the locus. Neo-resistant ES cell colonies were selected after electroporation, and successful targeting was assessed by long-range PCRs using primer pairs spanning the insertion sites on both the 5' and the 3' end of the targeting vector (Figure 3.4 B). After confirmation of correct integration of the construct into the *Slitl2* locus, mice were generated via the ES cell–tetraploid embryo aggregation technique. Using this strategy, mice can be generated that are completely ES cell-derived [Nagy, 2003]. Of 104 retransferred embryos, 16 heterozygous founder animals carrying a $Slitl2^{LacZ\text{-}neo}$ allele were born. They were mated with homozygous CMV-Cre mice. In these mice, the expression of Cre recombinase is driven by the cytomegalovirus (CMV) promoter, and the enzyme is therefore constitutively expressed in all cells. Cre recombinase catalyzes site-specific excision of DNA between *loxP* sites. Crossing of $Slitl2^{LacZ\text{-}neo/+}$ founders with CMV-Cre mice thus led to excision of the neo selection cassette in the generated progeny, thereby preventing any possible deleterious effect on LacZ expression (Figure 3.4 A). Heterozygous $Slitl2^{LacZ/+}$ mice were identified via a LacZ-specific PCR (Figure 3.4 C) and subsequently used for matings with wild-type NMRI mice to produce further heterozygous offspring in which *Slitl2* expression was reflected by LacZ expression.

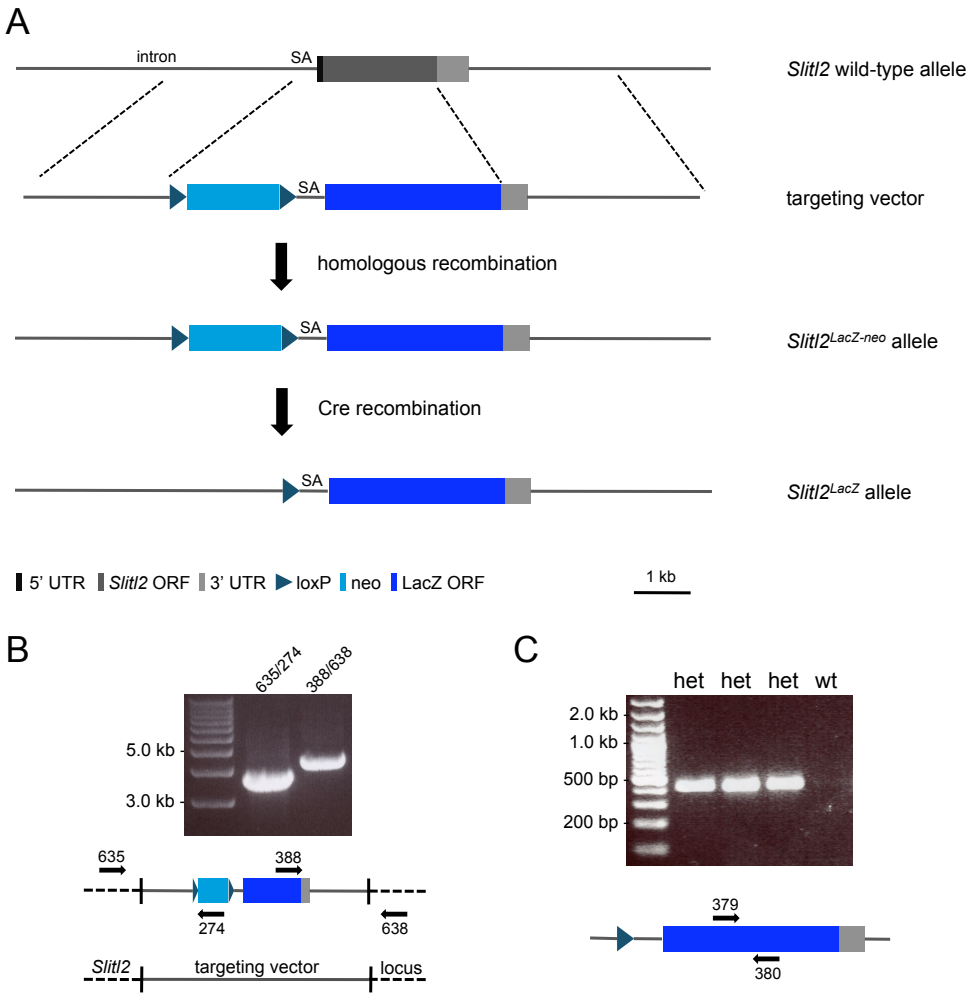

Figure 3.4 Generation of *Slitl2-LacZ* mice
A. Targeting scheme showing the *Slitl2* wild-type allele and the targeting vector. The $Slitl2^{LacZ\text{-}neo}$ allele was generated by homologous recombination. The $Slitl2^{LacZ}$ allele was derived by Cre-mediated recombination. (SA: splice acceptor) **B**. Correct integration into the *Slitl2* locus was confirmed by long range PCRs using primer pairs spanning the targeting vector–*Slitl2* locus junctions on both sides. Forward and reverse primers are indicated above and below the scheme, respectively. **C**. Heterozygous $Slitl2^{LacZ/+}$ mice were identified by a LacZ-specific PCR using the primer pair 379/380. Ethidium bromide-stained gel showing the PCR results for three heterozygous (het; left) and one wild-type mouse (wt; right).

3.1.2.2 *Slitl2-LacZ* expression at embryonic stages

To assess LacZ expression during mouse embryonic development, freshly dissected embryos were prefixed and incubated with X-gal staining solution at 37 °C until an appropriate staining intensity was obtained. Wild-type littermates did not reveal

any background staining with this protocol. Following the staining procedure, embryos from embryonic day 9.5 (E9.5) to E11.5 were postfixed and embedded in paraffin for subsequent sectioning. Due to insufficient penetration of the substrate, embryos from stage E12.0 onwards were embedded and frozen in Tissue-Tek® OCT compound (Ted Pella). Cryosections were obtained and incubated overnight with X-gal staining solution at 37 °C. All sections were counterstained with eosin before mounting.

β-Galactosidase activity was detected in heterozygous *Slitl2*$^{LacZ/+}$ whole-mount embryos already by **E8.0**. Weak expression was observed throughout the head mesenchyme. Stronger expression was evident in the lateral mesoderm and the caudal extremity of the embryo including the extraembryonic stalk of the allantois. Strong reporter expression was also seen in the developing hindbrain, while the neural folds were devoid of staining. Also, the somites as well as yet unsegmented paraxial mesoderm did not show expression (Figure 3.5 A).

At **E8.5**, expression was detected in several structures of the developing nervous system, namely the floor plate of the midbrain, rhombomeres 3 and 5, and the midline of the neural tube. Again, the lateral mesoderm and the caudal extremity of the embryo showed clear β-galactosidase activity. In addition, the mesenchyme of the developing first branchial arch exhibited staining (Figure 3.5 B).

By **E9.5**, the mouse embryo has completed the process of turning. β-Galactosidase expression at this stage was maintained in the floor plate and rhombomeres 3 and 5, while the remainder of the neural ectoderm showed no β-galactosidase activity. In addition, the mesenchyme of the branchial arches, the developing gut including the septum transversum, as well as the emerging forelimb buds, the lining of the coelomic cavities, and the ventral midline of the caudal extremity displayed expression (Figure 3.5 C).

The β-galactosidase signal became increasingly stronger with the advancement of embryonic development. Whole-mount specimens at **E10.5** revealed widespread expression throughout the head and trunk mesenchyme. Expression in the floor plate was maintained and could now also be observed in the roof plate. The branchial arches and both the forelimb and emerging hindlimb buds showed intense staining, while the developing heart seemed devoid of signal. Here, faint staining was only detected in its overlying surface ectoderm, the staining of which was indeed evident throughout the whole embryo. A median sagittal section confirmed expression in the floor plate and, in addition, revealed staining of the notochord (Figure 3.5 D).

At **E11.5**, the overall expression pattern of whole-mount specimens basically corresponded to that of the previous stage. However, marked changes were observed in the developing axial skeleton. Condensations of precartilaginous sclerotomic material were clearly evidenced by X-gal staining and were thereby readily distinguishable from intervening, unstained dorsal root ganglia. Moreover, expression in the developing ear pinna first became visible at this stage. Cross sections revealed staining of the coelom lining as well as the mesothelial lining of the hepatic primordium. The embryonic liver parenchyma itself, though, appeared clear of β-galactosidase signal at this stage of development (Figure 3.5 E).

From E12.5 to E15.5, the X-gal whole-mount staining patterns of heterozygous *Slitl2-LacZ* mice resembled each other. Digits of both the forelimbs and the hindlimbs became apparent and were intensely stained as were other parts of the developing skeletal system including the skull, the vertebral bodies, and the long bones of the limbs (Figure 3.6 A-D).

Sagittal sections of early **E12.5** embryos again displayed strong staining of both the visceral and parietal mesothelial linings. Also, the derivatives of the intermediate mesoderm were discernable at this stage. Faint expression was observed in the mesonephric tissue, which was thereby clearly demarcated from the even weaker stained metanephric blastema at its caudal tip and the unstained gonadal ridge at its medial aspect. The mesonephric duct, on the other hand, exhibited strong β-galactosidase signal (Figure 3.6 A).

As development progressed, expression in the developing urogenital system could be further specified given that at around E13.0, the sex of an embryo can be determined solely based on histological analysis. The cross section of an **E13.5** male embryo revealed a striped staining pattern characteristic of the testicular cords. The continuous differentiation of the metanephros also became obvious at this stage. The developing kidneys showed faint blue spots indicative of metanephric blastema cells forming nephrogenic vesicles (Figure 3.6 B).

The staining patterns of sagittal sections at **E14.5** and **E15.5** were very similar and are thus described synoptically. The most prominent β-galactosidase signal was again observed throughout the developing skeletal system. Interestingly, the nuclei pulposi of the intervertebral discs showed comparatively faint staining. The laryngeal cartilages as well as the cartilaginous tracheal rings, on the other hand, exhibited strong staining. Intense signal was also detected in arterial vessel walls, mainly the dorsal aorta. The developing lung exhibited a 'patchy' expression pattern due to stained mesenchymal interstitium but rather

unstained developing airway epithelium. In the esophagus, expression was restricted to the submucosal layer. This expression pattern was also observed in the intestine. Starting at E14.5, a defined cortical and medullary region could be distinguished in the kidneys, and faint β-galactosidase expression was indicated in first primitive glomeruli. By E15.5, numerous intensely stained glomeruli were visible. Virtually no signal was detected in the parenchyma of various other developing organs, namely the thymus, adrenal glands, and the liver. As already observed at younger stages, X-gal staining was detected in all visceral and parietal mesothelial linings of the body (Figure 3.6 C-D).

Figure 3.6 *Slitl2-LacZ* expression pattern from embryonic day 8.0 (E8.0) to E11.5
A. E8.0 **B**. E8.5 (left: dorsal view) **C**. E9.5
D. E10.5 (middle: dorsal view) **E**. E11.5
al, allantois;
ba, branchial arch;
ep, ear pinna;
fl, forelimb bud;
fp, floor plate;
gt, gut;
hb, hindbrain;
hl, hindlimb bud;
lm, lateral mesoderm;
nc, notochord;
nt, neural tube;
rh, rhombomere;
rp, roof plate;
sc, sclerotomic condensation;
st, septum transversum

Figure 3.7 *Slitl2-LacZ* expression pattern from embryonic day 12.5 (E12.5) to E15.5
A. E12.5 (middle: dorsal view) **B**. E13.5
C. E14.5 (middle: ventral view) **D**. E15.5
da, dorsal aorta;
es, esophagus;
gm, glomerulus;
gr, gonadal ridge;
lc, laryngeal cartilages;
lu, lung;
md, mesonephric duct;
mn, mesonephros;
mt, metanephros;
sm, stomach;
tc, testicular cord

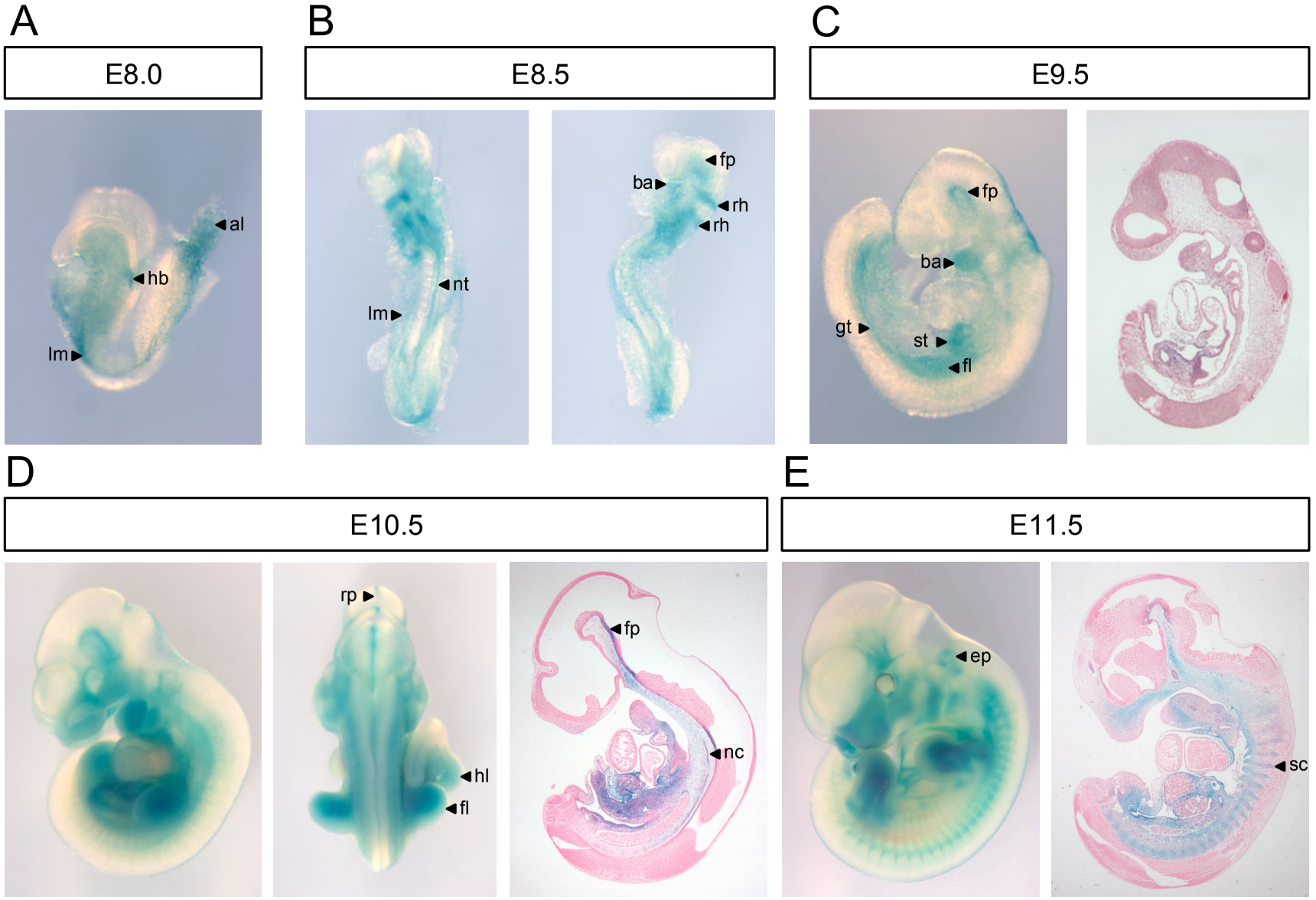

Figure 3.5 *Slitl2-LacZ* expression pattern from embryonic day 8.0 (E8.0) to E11.5. For details, see page 68.

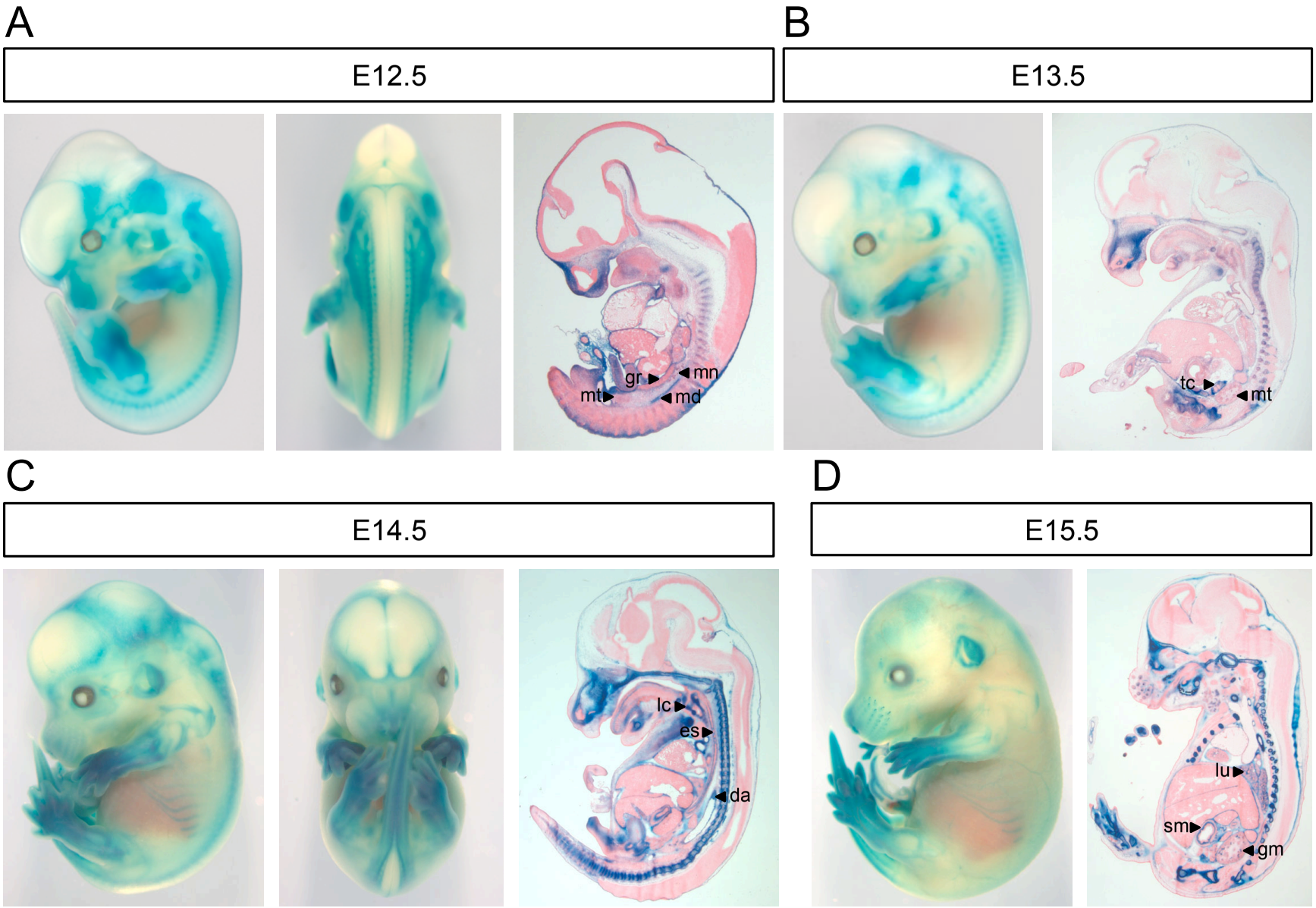

Figure 3.6 *Slitl2-LacZ* expression pattern from embryonic day 12.5 (E12.5) to E15.5. For details, see page 68.

3.1.2.3 *Slitl2-LacZ* expression at adult stage

To evaluate *Slitl2* expression domains at the adult stage, organs from 10-week-old *Slitl2-LacZ* mice were incubated with X-gal staining solution at 37 °C until an appropriate staining had developed. The organs were postfixed and paraffin-embedded, and the obtained sections were counterstained with eosin before mounting. Bone was decalcified with OSTEOSOFT® solution (Merck) prior to embedding with Tissue-Tek® OCT compound (Ted Pella). Cryo-sections were stained overnight at 37 °C and counterstained as above. For all tissues, accordingly treated wild-type samples did not reveal any background staining.

The kidney displayed a very distinct staining pattern already at macroscopic view. Most prominent were the intensely stained glomeruli throughout the cortical region. The arterioles as well as the interlobular arteries were also marked by reporter gene expression. In the renal medulla, the fine vasa recta were evident. In addition, the renal pelvis showed strong β-galactosidase activity (Figure 3.7 A and B). Microscopic examination of tissue sections revealed strong panglomerular β-galactosidase expression. However, at closer inspection, some nuclei, presumably of podocytes, seemed darkly stained, while others appeared rather unstained. Thus, with regard to the nuclear localization signal of the employed bacterial LacZ gene, diffusion of excess blue precipitate seemed to have caused the panglomerular expression pattern (Figure 3.7 C).

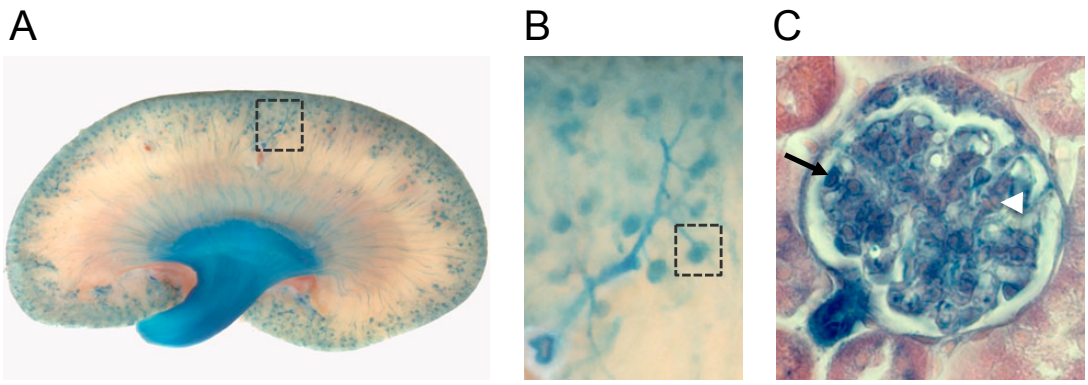

Figure 3.7 *Slitl2-LacZ* expression in the adult kidney
A. Cross section of a *Slitl2-LacZ* adult kidney showing strong β-galactosidase activity in the cortical region and in the renal pelvis. Dashed square indicates magnified region in B. **B**. Higher magnification revealed staining of the glomeruli, arterioles, and interlobular arteries in the cortex. Dashed square exemplifies magnified region in C. **C**. Microscopic view showed intense glomerular β-galactosidase activity. Arrow exemplifies darkly stained nucleus, arrowhead exemplifies unstained nucleus. (Magnification 100×)

In the cerebral cortex, the external granular cell layer exhibited intense staining (Figure 3.8 A), while in the cerebellum, β-galactosidase activity was only detected in the vessels (Figure 3.8 B). The airway epithelium throughout the lung exhibited staining as did the mesothelial cells lining the organ, namely the visceral pleura (Figure 3.8 C). A cross section of the descending aorta revealed strong expression in vascular smooth muscle cells (VSMCs). This staining was also evident in the adjacent vein, albeit less prominent due to the decreased thickness of the VSMC layer in this blood vessel type (Figure 3.8 D). Vessels in all organs examined were identifiable by staining of the VSMCs. In fact, they were the only cells that exhibited intense staining within the thymus and the liver (Figure 3.8 E and F). In the latter, the mesothelial cells of the organ capsule showed β-galactosidase activity, which was also the case for the spleen. Here, the vessels including the central arterioles of the white pulp regions displayed strong staining. Faint signal was observed throughout the splenic red pulp due to its extensive vascular tissue (Figure 3.8 G). The exocrine pancreas was devoid of β-galactosidase expression, while weak expression was seen in the islets of Langerhans (Figure 3.8 H). In the duodenum, the submucosal layer showed weak staining (Figure 3.8 I). Osteocytes, osteoblasts, osteoclasts, and chondrocytes were all clearly positive for reporter gene expression in the bone, whereas the cells of the bone marrow did not exhibit any staining (Figure 3.8 J).

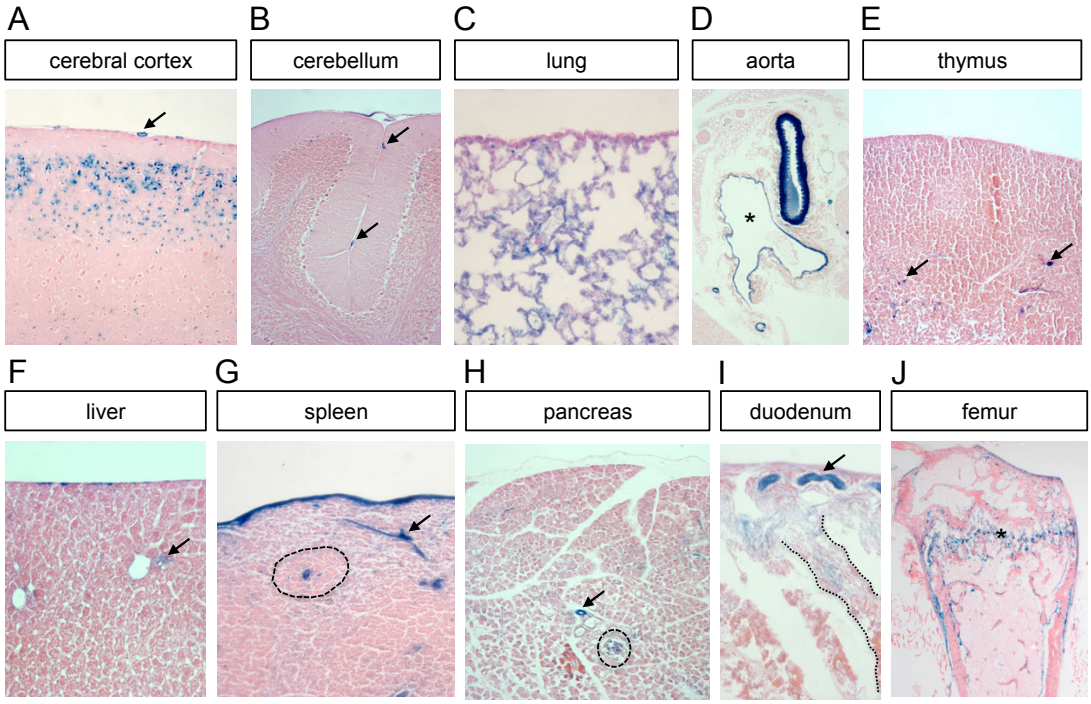

Figure 3.8 *Slitl2-LacZ* expression in adult organs
A. Cerebral cortex (Magnification 10×);
B. Cerebellum (Magnification 10×);
C. Lung (Magnification 20×);
D. Aorta; asterisk indicates vein lumen (Magnification 10×);
E. Thymus (Magnification 10×);
F. Liver (Magnification 20×);
G. Spleen; dashed circle demarcates white pulp region (Magnification 20×);
H. Pancreas; dashed circle demarcates islet of Langerhans (Magnification 10×);
I. Duodenum; dashed lines demarcate villus (Magnification 20×);
J. Femur; asterisk indicates growth plate (Magnification 5×);
Arrows indicate vessels in all images.
For detailed description, see subsubsection 3.1.2.3.

3.1.3 *Slitl2-Venus* expression

3.1.3.1 Generation of *Slitl2-Venus* mice

Slitl2-Venus transgenic mice were generated via bacterial artificial chromosome (BAC) recombineering. Recombineering stands for **recombi**nation-mediated genetic engi**neering** and is a powerful tool for site-specific modification of BAC DNA [Copeland et al., 2001]. Using a BAC containing the endogenous *Slitl2* locus (NCBI Clone ID RPCI-23-224H7) provided two advantages. First, BACs can harbor large inserts. Thus, the selected BAC most likely contained all as yet unidentified regulatory elements required for normal *Slitl2* expression as it contained the *Slitl2* locus flanked by approximately 115 kb and 80 kb of its native genomic environment on the 5' and the 3' end, respectively. Secondly, its large size also overcame the problems of positional effects associated with random integration of transgenes into the genome. The unmodified, circular BAC with its vector backbone pBACe3.6 was introduced into recombineering-competent SW105 bacteria [Warming et al., 2005]. For the generation of the targeting fragment, a modified version of the PL451 plasmid was used [Liu et al., 2003]. In addition to the *FRT*-flanked neomycin (neo) selection cassette, it contained the Venus open reading frame (ORF) encoding a variant of the yellow fluorescent protein (YFP) with enhanced maturation and brightness [Rekas et al., 2002]. The Venus-neo fragment was PCR-amplified using chimeric primers that added *Slitl2* homology regions on both ends of the product. Thus, after successful targeting, the Venus gene together with the neo selection cassette would be introduced upstream of the *Slitl2* coding sequence and, as a result, Venus expression would be under control of the endogenous *Slitl2* regulatory sequences, thereby mirroring *Slitl2* expression (Figure 3.9 A). The targeting fragment was electroporated into SW105 bacteria harboring the unmodified *Slitl2* BAC, kanamycin-resistant colonies were selected, and successful recombination was confirmed by various PCRs with primer pairs designed to span the different intergenic junctions (Figure 3.9 B and C). The modified BAC was then isolated from the bacteria and linearized with *P*I-*Sce*I, which recognizes a sequence in the pBACe3.6 vector backbone. It was introduced into G4 embryonic stem (ES) cells [George et al., 2007] via electroporation, and neo-resistant ES cell colonies, that had integrated the modified BAC randomly into their genome, were selected and subsequently used for the production of *Slitl2-Venus* transgenic mice via the ES cell–morula aggregation technique [Nagy, 2003]. Ten transgenic mice were born out of 120 retransferred embryos. Inte-

gration of the entire modified BAC into the mouse genome was confirmed by PCR using primer pairs flanking the pBACe3.6 vector–BAC junctions on both ends (Figure 3.9 B and D). Transgenic mice were identified by PCR and used for matings with wild-type NMRI mice to produce further offspring in which *Slitl2* expression was reflected by Venus expression.

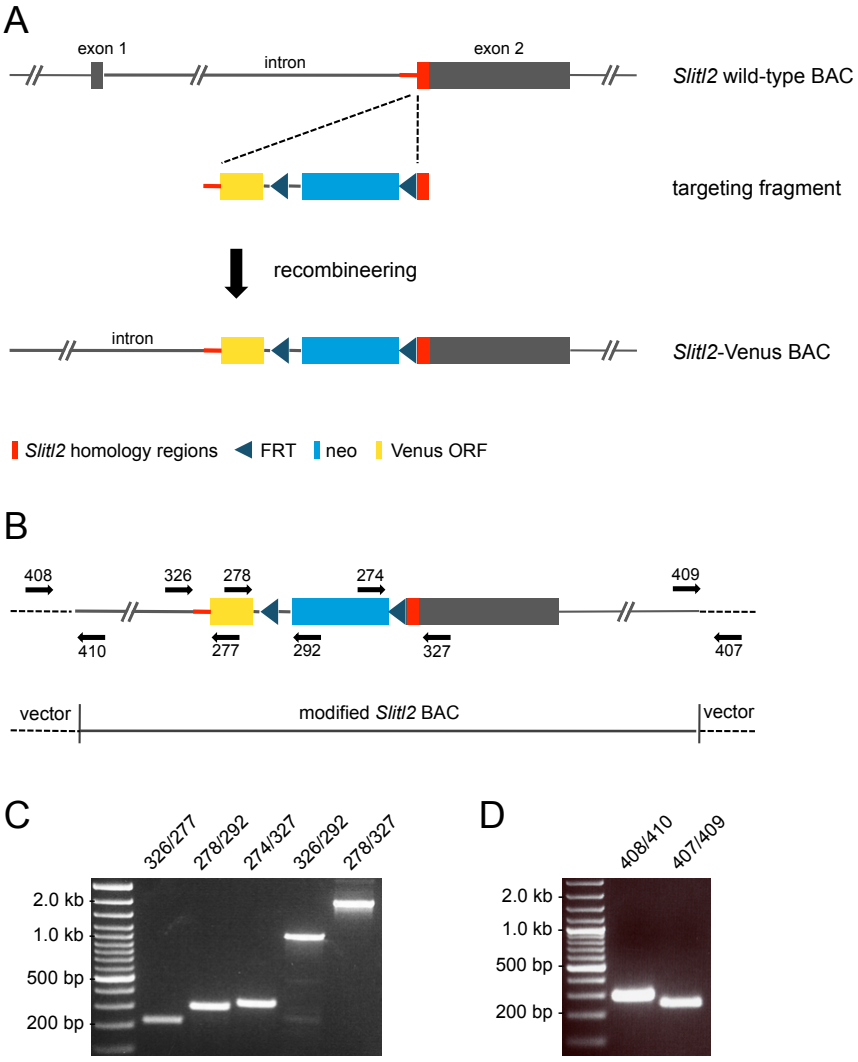

Figure 3.9 Generation of *Slitl2-Venus* transgenic mice
A. Targeting scheme showing the *Slitl2* wild-type BAC and the Venus-neo targeting fragment with *Slitl2* homology arms on both ends. The *Slitl2-Venus* BAC was generated by recombineering. **B**. PCR screening scheme. Forward and reverse primers are indicated above and below the *Slitl2-Venus* BAC, respectively. **C**. Ethidium bromide-stained gel showing PCR results using primer pairs spanning over different fragment junctions. Primer combinations are indicated above each lane. **D**. Integration of the entire BAC genome was confirmed by PCRs using primer pairs spanning over the vector–BAC junctions on both ends. Primer combinations are indicated above each lane.

3.1.3.2 Venus expression in *Slitl2-Venus* embryos

Venus expression could be directly visualized by fluorescence microscopy in *Slitl2-Venus* embryos due to the protein's autofluorescence. Even though the signal was very faint initially, transgenic embryos could be identified with this method and thereby be distinguished from wild-type littermates. Venus expression could be attributed to the developing skeletal system as early as E12.5. As development proceeded, the signal intensity in the bone-forming tissue increased. By E14.5, the Venus expression pattern distinctly resembled the β-galactosidase expression pattern observed in *Slitl2-LacZ* heterozygous embryos (Figure 3.6). This approach demonstrated that Venus expression in *Slitl2-Venus* transgenic mice is driven by *Slitl2* regulatory elements and that *Slitl2-Venus* mice can therefore be considered a *Slitl2* reporter mouse strain.

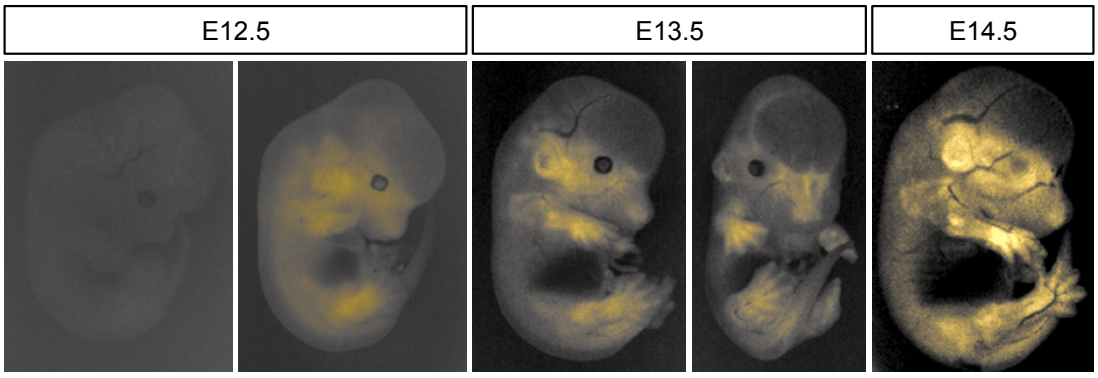

Figure 3.10 Venus expression in *Slitl2-Venus* embryos
Expression of Venus was visualized by fluorescence microscopy. In comparison to a wild-type littermate (left), a *Slitl2-Venus* transgenic embryo showed Venus expression at E12.5 when applying the same exposure conditions (right). Increased Venus expression was observed with proceeding development (E13.5-E14.5) and was predominantely detected in the developing skeletal system.

3.1.3.3 Venus expression in adult *Slitl2-Venus* kidneys

In order to evaluate the expression of Venus in adult *Slitl2-Venus* kidneys, formalin-fixed, paraffin-embedded tissue sections were subjected to immunohistochemical analysis. Venus was detected using two different anti-green fluorescent protein (α-GFP) antibodies able to recognize also mutant forms of the protein. Coupling of the primary antibody was assessed by incubation with peroxidase-coupled secondary antibodies (ImmPRESS™ REAGENT kit; Vector Laboratories) and sub-

sequent detection with NovaRED™ substrate (Vector Laboratories). All sections were counterstained with hematoxylin prior to mounting.

Both antibodies rendered a similar staining pattern for Venus expression in the glomeruli. Compared to the glomerular marker analysis using α-WT1, α-Desmin, and α-PECAM-1 antibodies (subsubsection 3.3.2.2), mainly podocytes seemed to be detected by the α-GFP antibodies. Similar to what was observed for the expression of β-galactosidase in *Slitl2-LacZ* kidneys, some cells in the glomeruli – presumably mesangial cells – were unstained (Figure 3.11 A and B). Marked Venus expression could also be seen in the vascular smooth muscle cell layer (Figure 3.11 B), a finding consistent with the *Slitl2-LacZ* expression analysis (subsubsection 3.1.2.3).

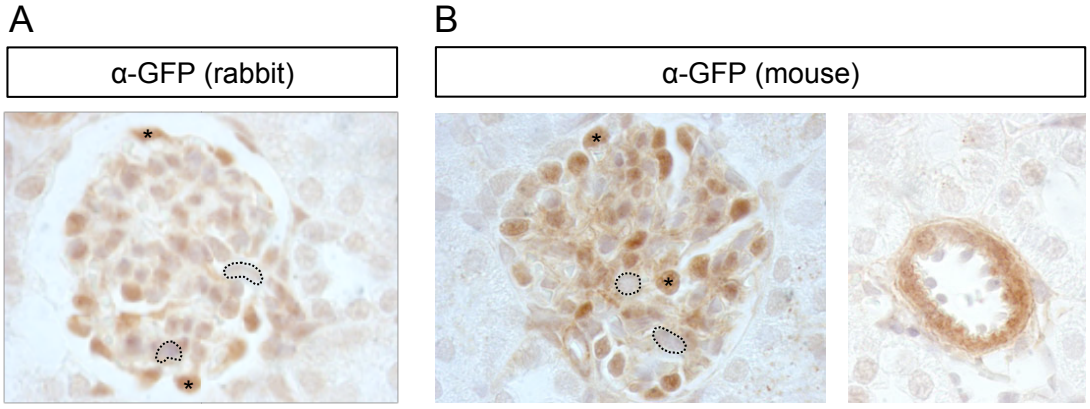

Figure 3.11 Immunohistochemical analysis of Venus expression in *Slitl2-Venus* kidneys
A. Venus expression in the glomerulus detected by a polyclonal anti-green fluorescent protein (α-GFP) antibody. (Magnification 100×) **B**. Venus expression detected by a monoclonal α-GFP antibody (left: glomerulus, right: arterial vessel; magnification 100×). Asterisks exemplify stained cells, dashed circles exemplify unstained cells in the glomeruli.

3.2 Generation of *Slitl2*-mutant mice

Slitl2-mutant mice were generated via classical gene targeting by the use of embryonic stem (ES) cells. This technique was pioneered by Mario R. Capecchi, Sir Martin J. Evans, and Oliver Smithies, for which they were awarded the 2007 Nobel Prize in Medicine. The method is based on homologous recombination between a targeting vector and an endogenous gene, thereby replacing the wild-type sequence with its modified version.

3.2.1 Gene targeting of the mouse *Slitl2* locus

The plasmid used for targeting the mouse *Slitl2* locus harbored a 10.5 kb-long construct inserted into the pBluescript II SK vector (Stratagene). The insert contained a *loxP*-flanked, i.e., floxed neomycin (neo) selection cassette in the intronic sequence of *Slitl2* 68 bp upstream of the ATG start codon, thereby leaving the splice acceptor site upstream of exon 2 intact. In addition, a third *loxP* site was introduced 96 bp downstream of the TAG stop codon in the 3' untranslated region (UTR). This modified version of the *Slitl2* coding exon 2 was flanked by a 3 kb- and a 3.6 kb-long 5' and 3' arm of homology, respectively (Figure 3.12 A). The construct was linearized with *Nru*I and electroporated into G4 ES cells. Neo-resistant ES cell colonies were selected, and clones that had successfully undergone homologous recombination to generate a $Slitl2^{floxed\text{-}neo}$ allele were identified by Southern blotting using *Hind*III-digested genomic DNA. As an additional *Hind*III site was introduced just downstream of the third *loxP* site, the digestion pattern allowed for discrimination between the wild-type and the mutated allele. Six out of 192 clones analyzed showed the correct targeting event with both external probes: while the wild-type allele rendered a 12 kb band for both probes, the $Slitl2^{floxed\text{-}neo}$ allele produced a 9.3 kb band for the 5' probe and a 4.2 kb band for the 3' probe (Figure 3.12 B and C).

Cre-mediated recombination was performed on one of the $Slitl2^{floxed\text{-}neo}$ allele-carrying clones in order to create a conditional $Slitl2^{floxed}$ allele, in which the neo cassette had been excised, and a $Slitl2^{null}$ allele, in which both the neo cassette and the coding sequence of *Slitl2* had been deleted (Figure 3.12 A). For transient expression of the Cre recombinase, a plasmid containing the Cre open reading frame under control of the phosphoglycerate kinase (PGK) promoter was electroporated into $Slitl2^{floxed\text{-}neo/+}$ ES cells to catalyze site-specific excision of DNA between the *loxP* sites. Following Cre treatment, the ES cells were plated at

low density, and the derived clones were again analyzed by Southern blotting of *Hind*III-digested DNA. Of 96 clones, three had undergone correct excision to generate a conditional *Slitl2*^{floxed} allele and one to generate a *Slitl2*^{null} allele. The 5' probe now revealed a 7.7 kb and a 5.5 kb fragment for the *Slitl2*^{floxed} and the *Slitl2*^{null} allele, respectively. The 3' probe showed a 4.2 kb band for both mutated alleles (Figure 3.12 B and C).

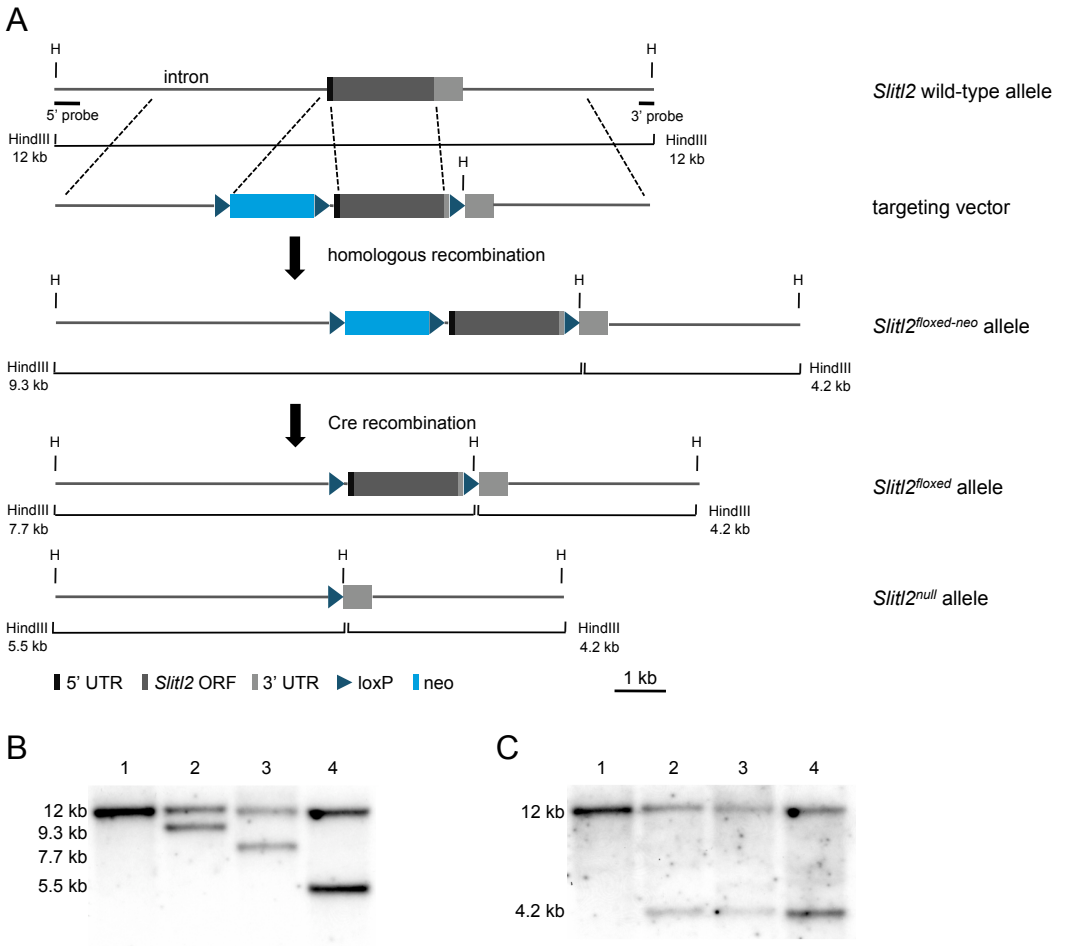

Figure 3.12 Targeting of the *Slitl2* locus

A. Targeting scheme showing the *Slitl2* wild-type allele and the targeting vector. The *Slitl2*$^{floxed\text{-}neo}$ allele was generated by homologous recombination. Subsequent Cre recombination produced a conditional *Slitl2*^{floxed} allele and a *Slitl2*^{null} allele. The introduction of an additional *Hind*III site (H) allowed for discrimination of the different alleles via Southern blot analysis using external 5' and 3' probes. **B**. Southern blot analysis of *Hind*III-digested genomic DNA from wild-type (1), heterozygous *Slitl2*$^{floxed\text{-}neo/+}$ (2), heterozygous *Slitl2*$^{floxed/+}$ (3), and heterozygous *Slitl2*$^{null/+}$ (4) ES cells using the external 5' probe. **C**. Southern blot analysis of *Hind*III-digested genomic DNA using the external 3' probe. (Lanes 1-4 as in **B**)

The three different heterozygous ES cell lines (*Slitl2*$^{floxed\text{-}neo/+}$, *Slitl2*$^{floxed/+}$, and *Slitl2*$^{null/+}$) were propagated and used for the production of *Slitl2*-mutant mouse lines. The ES cells employed for these experiments were male F1 hybrid cells of maternal 129S6/SvEvTac (129) and paternal C57BL/6Ncr (B6) background (G4 ES cells) [George et al., 2007]. These cells give rise to agouti offspring since the 129 agouti coat color is dominant over the B6 black coat color. Since embryos from white CD1 or black C57BL/6 mice served as hosts, it was possible to estimate the contribution of the ES cells to the derived animals by their coat color.

3.2.2 Generation of *Slitl2-floxed-neo* mice

It has been shown previously that inclusion of a neo cassette in the intronic sequence of a gene can produce a so-called hypomorphic allele. This effect was induced by cryptic splice sites within the neo coding region causing a reduction in the amount of functional gene expression due to aberrant splicing [Meyers et al., 1998]. To assess whether the neo cassette, which was inserted primarily as a selection marker for the targeted allele, led to impairment of *Slitl2* gene function, *Slitl2-floxed-neo* mice were generated by ES cell–tetraploid embryo aggregation [Nagy, 2003]. One agouti founder was born from 34 embryos that had been retransferred into recipient females. It was mated with C57BL/6 females to establish heterozygous F1 mice, which were then intercrossed to produce homozygous F2 progeny. The genotype of all animals was identified by PCR using primer pairs that allowed for discrimination between the wild-type and the modified allele (Figure 3.13 A and B). All further offspring were derived by mating homozygous F2 animals. In these mice, no obvious hypomorphic effect could be observed. The animals were phenotypically indistinguishable from wild-type mice, fertile, and had a normal life span without showing any symptoms of disease, indicating that insertion of the neo cassette didn't affect *Slitl2* gene function, at least not to a critical extent.

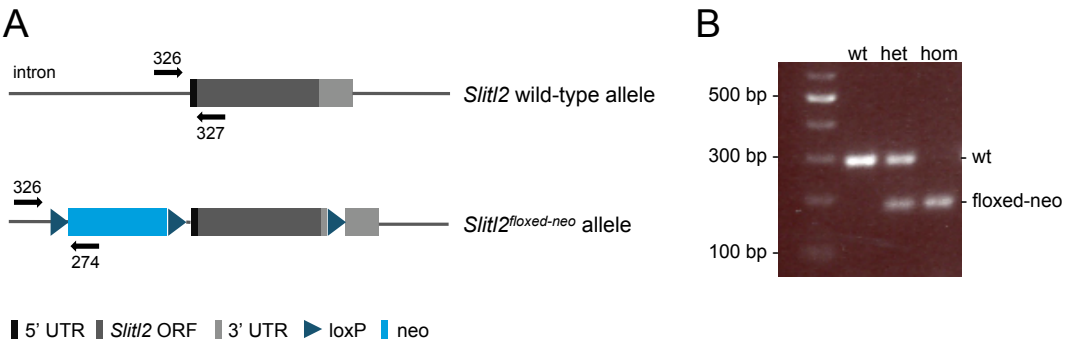

Figure 3.13 Genotyping of *Slitl2-floxed-neo* mice
A. PCR scheme used for discrimination of the *Slitl2* wild-type and the *Slitl2*$^{floxed\text{-}neo}$ allele. Forward and reverse primers are indicated above and below, respectively. **B**. Ethidium bromide-stained gel showing the PCR results of a wild-type (wt), a heterozygous *Slitl2*$^{floxed\text{-}neo/+}$ (het), and a homozygous *Slitl2*$^{floxed\text{-}neo/floxed\text{-}neo}$ (hom) mouse.

3.2.3 Generation of conditional *Slitl2-floxed* mice

The *Slitl2-floxed* strain was produced via the morula injection technique using C57BL/6 host embryos. Here, chimeric mice are generated as both the donor ES cells and the host morula cells can contribute to the developing embryo proper. All seven founders that were born from 60 retransfers were agouti-colored males, indicating that they were almost fully ES cell-derived. They were mated with C57BL/6 females. Heterozygous *Slitl2-floxed* offspring were identified by PCR and intercrossed in order to derive homozygous F2 progeny (Figure 3.14 A and B). These animals were then interbred to establish a homozygous *Slitl2-floxed* mouse line. In the genome of homozygous *Slitl2-floxed* mice, the *Slitl2* coding region is flanked by *loxP* sites, i.e., floxed on both alleles. Previous studies have demonstrated that the presence of a *loxP* site within the intronic sequence of a gene does not interfere with its expression [Meyers et al., 1998]. Thus, while being a functional wild-type, the *Slitl2*^{floxed} allele allowed for *in vivo* excision of the floxed region when mating these animals with mice expressing Cre recombinase. The capacity to delete the floxed gene *in vivo* was confirmed by crossing *Slitl2-floxed* mice with homozygous CMV-Cre transgenic mice [Schwenk et al., 1995]. In this mouse strain, the expression of Cre recombinase is driven by the cytomegalovirus (CMV) promoter, thus causing ubiquitous deletion of floxed DNA segments. To derive conditional *Slitl2*-deficient mice, homozygous *Slitl2-floxed* mutants were first crossed with CMV-Cre deleter mice to excise the *Slitl2* coding region on one

allele. The derived animals carrying only one intact *Slitl2* allele and one copy of the CMV-Cre transgene were then mated with homozygous *Slitl2-floxed* mice to produce offspring in which the coding sequence of *Slitl2* had been deleted on both alleles. These conditional *Slitl2* knock-out mice recapitulated the phenotype of homozygous *Slitl2-null* mice that were produced by the classical, non-conditional strategy (see below). This approach demonstrated that the conditional knock-out system is highly efficient in *Slitl2-floxed* mice and that it provides a useful tool for tissue-specific knock-out of *Slitl2* when crossing these mice with a strain that expresses the Cre recombinase under a promoter specific for the respective tissue.

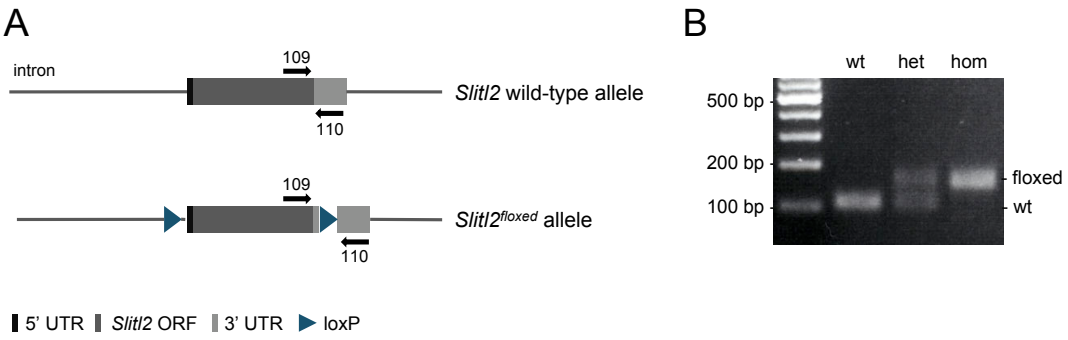

Figure 3.14 Genotyping of *Slitl2-floxed* mice
A. PCR scheme used for discrimination of the *Slitl2* wild-type and the *Slitl2*^{floxed} allele. Forward and reverse primers are indicated above and below, respectively. **B**. Ethidium bromide-stained gel showing the PCR results of a wild-type (wt), a heterozygous *Slitl2*$^{floxed/+}$ (het), and a homozygous *Slitl2*$^{floxed/floxed}$ (hom) mouse.

3.2.4 Generation of *Slitl2-null* mice

Slitl2-null founder animals were generated with ES cells heterozygous for the *Slitl2*^{null} allele using the morula aggregation technique [Nagy, 2003]. 42 retransfers yielded eleven *Slitl2-null* founders including one white, one chimeric, and six agouti males and one female of each coat color. C57BL/6 females were then mated with the agouti-colored male founders. They were chosen based on the assumption that the contribution of ES cells to their tissues was highest among all founder animals and thus were most likely to give germline transmission. Derived heterozygous *Slitl2-null* animals were phenotypically normal and were used for subsequent matings to generate *Slitl2*-deficient mice. The genotype of all mice was assessed by PCR using primer combinations that allowed for distinction between the wild-type and the mutated allele (Figure 3.15 A and B).

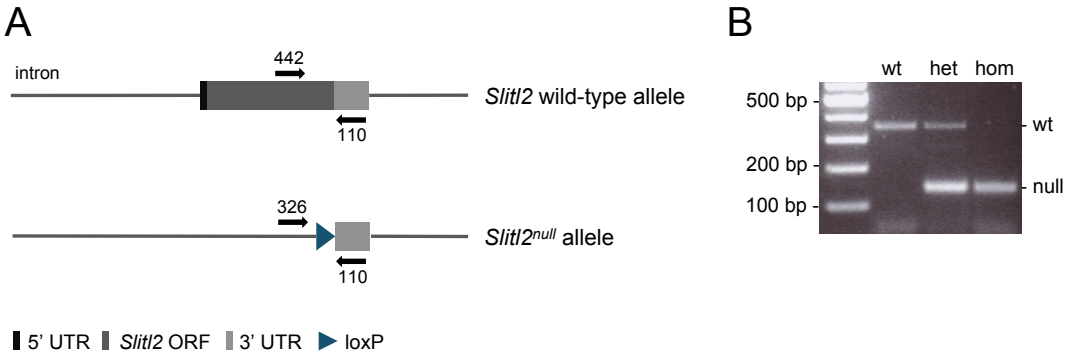

Figure 3.15 Genotyping of *Slitl2-null* mice
A. PCR scheme used for discrimination of the *Slitl2* wild-type and the *Slitl2*^{null} allele. Forward and reverse primers are indicated above and below, respectively. **B**. Ethidium bromide-stained gel showing the PCR results of a wild-type (wt), a heterozygous *Slitl2*$^{null/+}$ (het), and a homozygous *Slitl2*$^{null/null}$ (hom) mouse.

3.3 Phenotypic analysis of *Slitl2*-deficient mice

3.3.1 General characteristics

To elucidate the effect of a total loss of *Slitl2* gene function, heterozygous *Slitl2-null* mice were intercrossed. These matings yielded wild-type *Slitl2*$^{+/+}$, heterozygous *Slitl2*$^{+/-}$, and homozygous *Slitl2*$^{-/-}$ offspring at the expected Mendelian ratio (26%, 50%, and 24%, respectively; n=530). To ascertain that *Slitl2* expression was indeed eliminated in *Slitl2*$^{-/-}$ animals, total RNA from adult mouse kidneys and protein lysates from mouse primary embryonic fibroblast (MEF) cells of heterozygous and homozygous *Slitl2-null* mice were analyzed by Northern and Western blotting, respectively, using the same probe and antibody as described before (subsubsection 3.1.1.1 and subsubsection 3.1.1.2). Neither *Slitl2* RNA nor Slitl2 protein was detected in the homozygous mutants, confirming the complete inactivation of the gene (Figure 3.16 A and B).

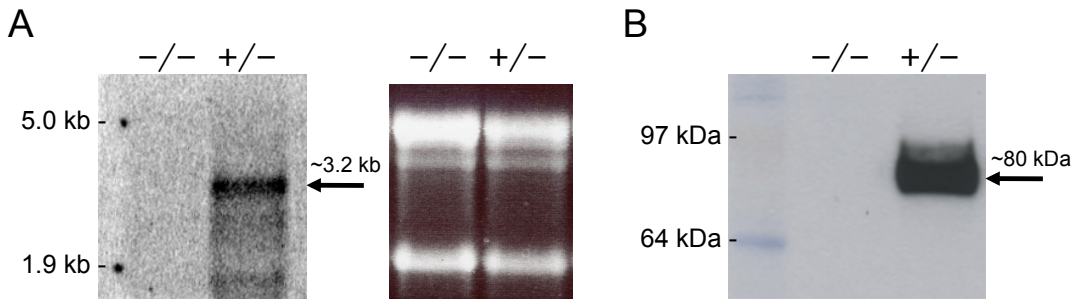

Figure 3.16 Verification of *Slitl2* gene inactivation
A. Northern blot analysis demonstrating the absence of *Slitl2* RNA expression in a homozygous *Slitl2*$^{-/-}$ compared to a heterozygous *Slitl2*$^{+/-}$ adult mouse kidney (left). Ethidium bromide-stained gel showing rRNA bands as loading control (right). **B**. Western blot analysis confirming the absence of Slitl2 protein in homozygous *Slitl2*$^{-/-}$ mouse primary embryonic fibroblasts (MEFs) compared to heterozygous *Slitl2*$^{+/-}$ MEFs.

The *Slitl2* knock-out mutants appeared normal at birth and were phenotypically indistinguishable from their littermates. Two weeks postnatally, however, the null mutants already exhibited mild growth retardation. The average weight of *Slitl2*$^{-/-}$ mice was decreased to approximately 90% of that of their wild-type littermates. By the age of three weeks, the average weight of *Slitl2*-deficient mice was down to approximately 80%, with some animals weighing as little as 50% of the controls (Figure 3.17).

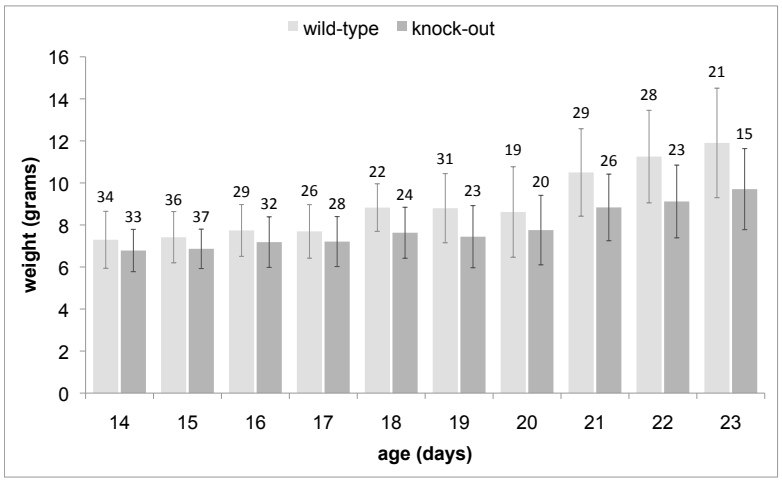

Figure 3.17 Growth retardation in *Slitl2*-deficient mice
Statistical analysis revealed impaired growth in *Slitl2*-deficient mice in comparison to their wild-type littermates. Error bars indicate ± SD. Numbers above error bars represent numbers of animals in the respective group.

Starting as early as two weeks after birth, all *Slitl2*-deficient animals developed a severe, eventually lethal illness. The typical external features of a moribund *Slitl2*$^{-/-}$ mouse – apart from its reduced size – included a marked generalized edema, smaller external ears, and a more round snout. Prior to death, null mutants presented lethargic, emaciated, with a hunched posture and a ruffled fur (Figure 3.18).

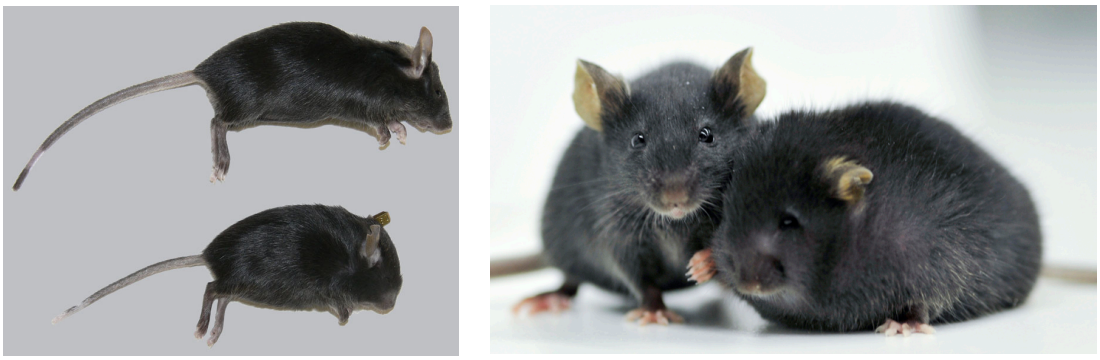

Figure 3.18 Phenotype of *Slitl2*-deficient mice
Moribund *Slitl2*-deficient mice showed a reduced size (left), severe generalized edema, smaller external ears, and a more round snout (right) in comparison to wild-type littermates.

The onset of wasting was clustered around weaning at postnatal day 21, and *Slitl2*-deficient mice died by the age of 26 days on average (n=31), ranging from 16 to 41 days (Figure 3.19).

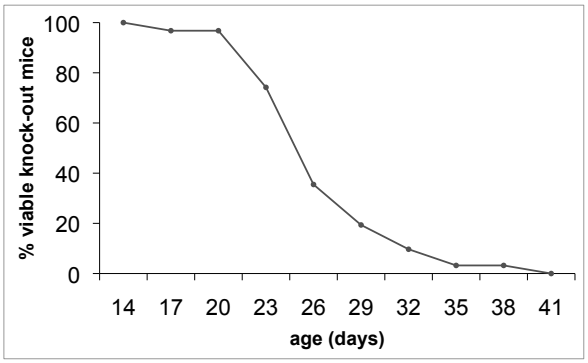

Figure 3.19 Mortality rate in *Slitl2*-deficient mice
Death in *Slitl2*-deficient mice (n=31) was clustered around weaning at postnatal day 21. Only three mutant mice lived longer than 35 days. No mutant mouse survived after postnatal day 41.

Necropsy of moribund *Slitl2*-deficient mice revealed severe subcutaneous edema, hydrothorax, and ascites. The most striking finding in all moribund mice were disproportionally small thymi and spleens. These organs were mostly less than half the size of that of wild-type littermates, and the spleens consistently displayed an extreme pale color. The mean thymic and splenic weight of moribund mutants was decreased to 0.08% and 0.1% of their body weight, respectively, while accounting for 0.5% and 0.4% of total body weight in control littermates (n=5).

In addition, lymph nodes were also found to be decreased in size. Moreover, the kidneys were consistently of ischemic appearance (Figure 3.20).

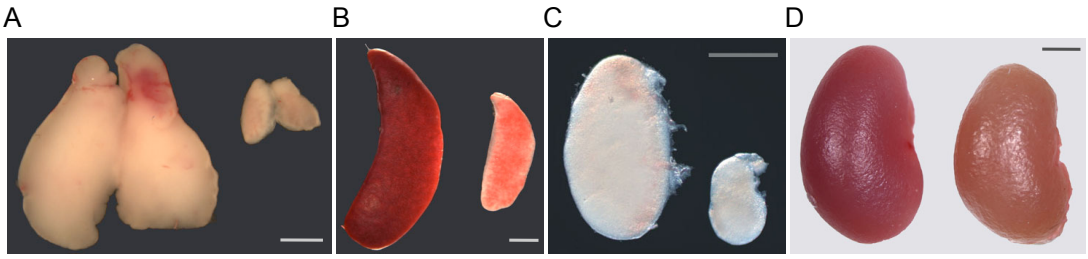

Figure 3.20 Comparison of thymus, spleen, lymph node, and kidney
A. Atrophic thymus (Scale bar: 2 mm) **B**. Atrophic, pale spleen (Scale bar: 2 mm) **C**. Atrophic iliac lymph node (Scale bar: 1 mm) **D**. Pale kidney (Scale bar: 2 mm); all pictures show organs of a moribund *Slitl2*-deficient mouse (right) in comparison to those organs from a wild-type littermate (left).

3.3.2 Kidney phenotype of *Slitl2*-deficient mice

3.3.2.1 Histological examination

To analyze the nature of histological changes in *Slitl2*-mutant mice, tissue sections were obtained from formalin-fixed, paraffin-embedded organs and subjected to hematoxylin and eosin (H&E) staining. Microscopic examination of kidneys from moribund *Slitl2*$^{-/-}$ mice revealed multiple proteinaceous casts that were dispersed throughout the cortex as well as the medulla. These casts mainly originated from the tubular system and caused their obstruction and subsequent dilation (Figure 3.21 A). In addition, hyaline droplet formation was observed in epithelial cells of as yet undilated proximal tubules due to substantial resorption of proteins (Figure 3.21 B). The pathological changes also affected the glomeruli. The gradual degeneration of the glomerular morphology was initially evidenced by capillary ectasia and intracytoplasmic vacuole formation. More severely damaged glomeruli exhibited a complete atrophy of the capillary tuft (Figure 3.21 C).

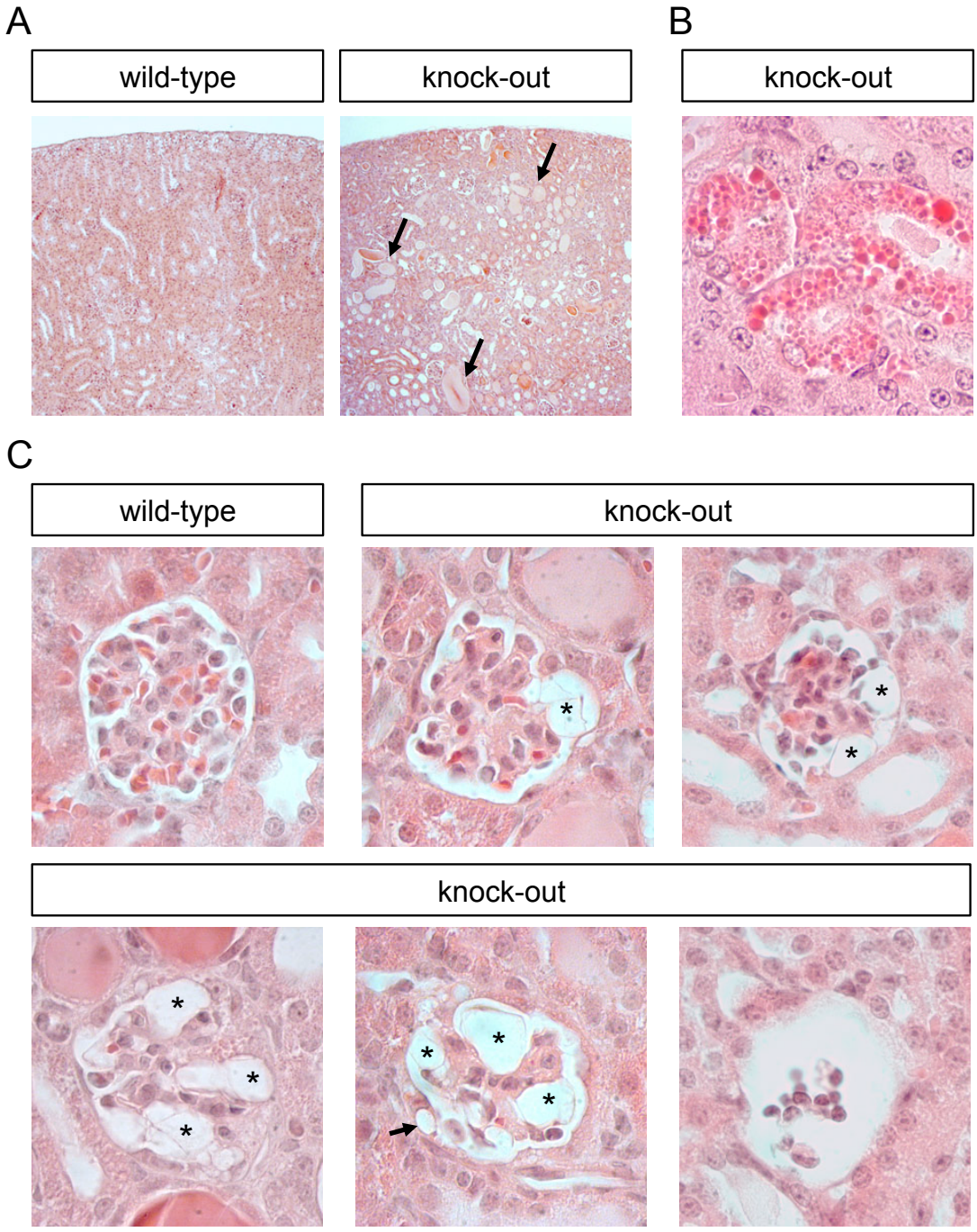

Figure 3.21 Kidney histopathology of *Slitl2*-deficient mice; H&E staining
A. Overview; arrows indicate proteinaceous casts in renal tubular system (magnification 10×). **B**. Higher magnification revealed hyaline droplets in proximal tubular cells (Magnification 100×). **C**. Higher magnification of glomeruli showed ectatic capillaries (asterisks), intracytoplasmic vacuoles (arrow), and atrophic capillary tufts (bottom right) (Magnification 100×).

To evaluate whether the absence of *Slitl2* function led to excess formation of connective tissue, sections were stained with periodic acid-Schiff (PAS) and Masson's trichrome to detect such possible deposits. Polysaccharides, neutral mucopolysaccharides, and basement membrane constituents stain purple-magenta in PAS staining, while collagen stains blue in Masson's trichrome staining. These staining methods are used to detect fibrotic or glomerulosclerotic lesions that are related to renal disease conditions. In the kidneys of moribund *Slitl2*-deficient mice, only tubular proteinaceous casts showed the respective characteristic staining, while the renal tissue itself was devoid of such deposits. (Figure 3.22 A–B).

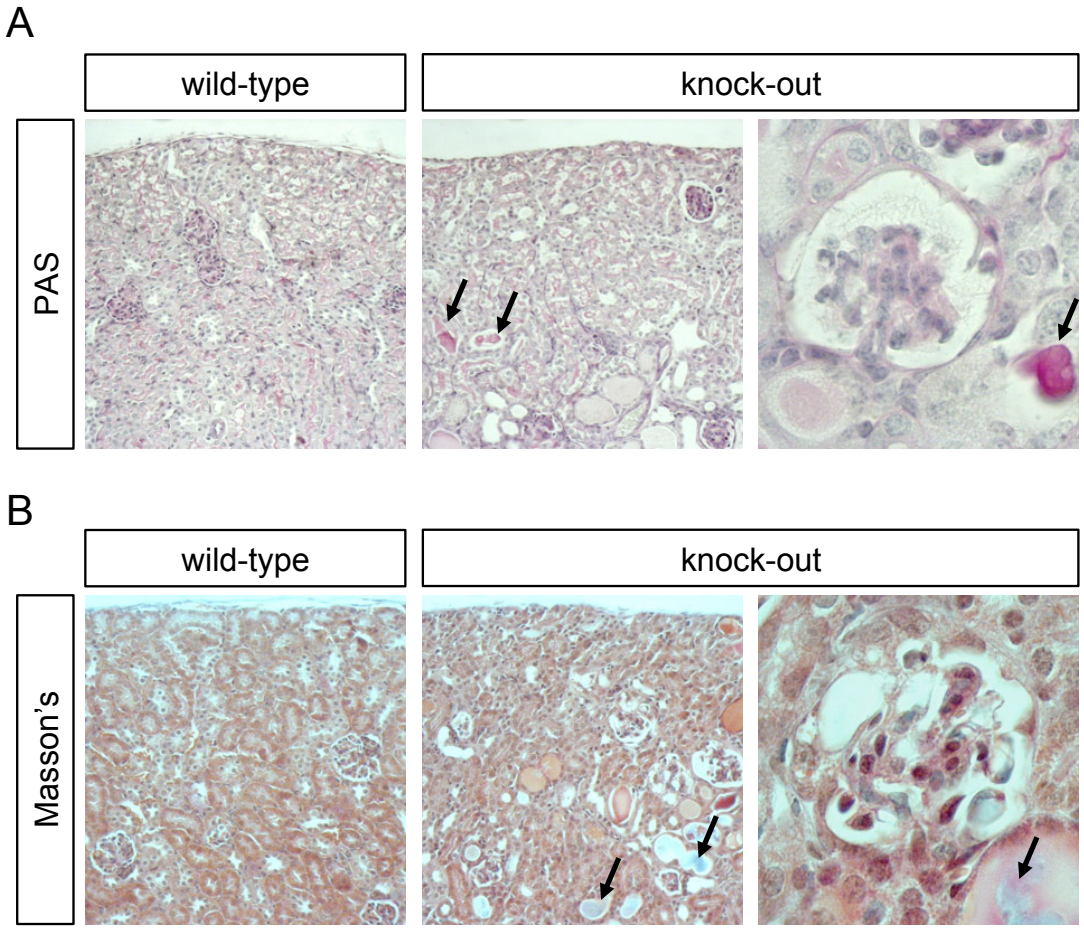

Figure 3.22 Kidney histopathology of *Slitl2*-deficient mice
Periodic acid-Schiff (PAS) and Masson's trichrome staining
A. Overview (left and middle; magnification 20×); higher magnification of a glomerulus (right; magnification 100×); only tubular proteinaceous casts showed magenta color characteristic of PAS staining (arrows). **B**. Overview (left and middle; magnification 20×); higher magnification of a glomerulus (right; magnification 100×); only tubular proteinaceous casts showed blue color characteristic of Masson's trichrome staining (arrows).

Kidney sections of newborn *Slitl2* null mutants did not yet reveal any of the above described pathological changes and were indistinguishable from that of wild-type littermates. The age at which signs of histological anomalies first became apparent was variable. Some of the mutants analyzed at postnatal day 10 already showed some minor alterations. By the age of two weeks, all examined *Slitl2*$^{-/-}$ kidneys displayed initial lesions. The progression of these changes at this stage, however, differed among the specimens analyzed. The severity – as estimated by the number and size of dilated tubules – progressed with age, and kidneys of moribund *Slitl2*-deficient mice consistently showed severe anomalies including numerous dilated tubules and atrophic glomerular tufts.

3.3.2.2 Immunohistochemical examination

The glomerulus is composed of four major cell types: endothelial cells of the capillary loop, mesangial cells that mechanically support the capillary wall, parietal epithelial cells lining the Bowman's capsule, and visceral epithelial cells, i.e., podocytes which coat the glomerular capillary tuft. The different cells can be discriminated by immunohistochemical staining using marker antibodies that specifically detect one cell type. Anti-Wilms' tumor antibody (α-WT1) labels podocytes and parietal epithelial cells, whereas anti-Desmin antibody (α-Desmin) is specific for mesangial cells. Endothelial cells are stained by anti-platelet/endothelial cell adhesion molecule antibody (α-PECAM-1) (Figure 3.23 A).

To assess the glomerular structure in *Slitl2*$^{-/-}$ kidneys, tissue sections were stained with all three antibodies. The organization of unaffected glomeruli in mutant kidneys was similar to that of control animals. All components were uniformly labeled with the respective markers and showed a normal structure (Figure 3.23 B and C). In affected glomeruli displaying ectatic capillaries and intracytoplasmic vacuoles, all major cell types could still be detected despite the disorganized morphology (Figure 3.23 D).

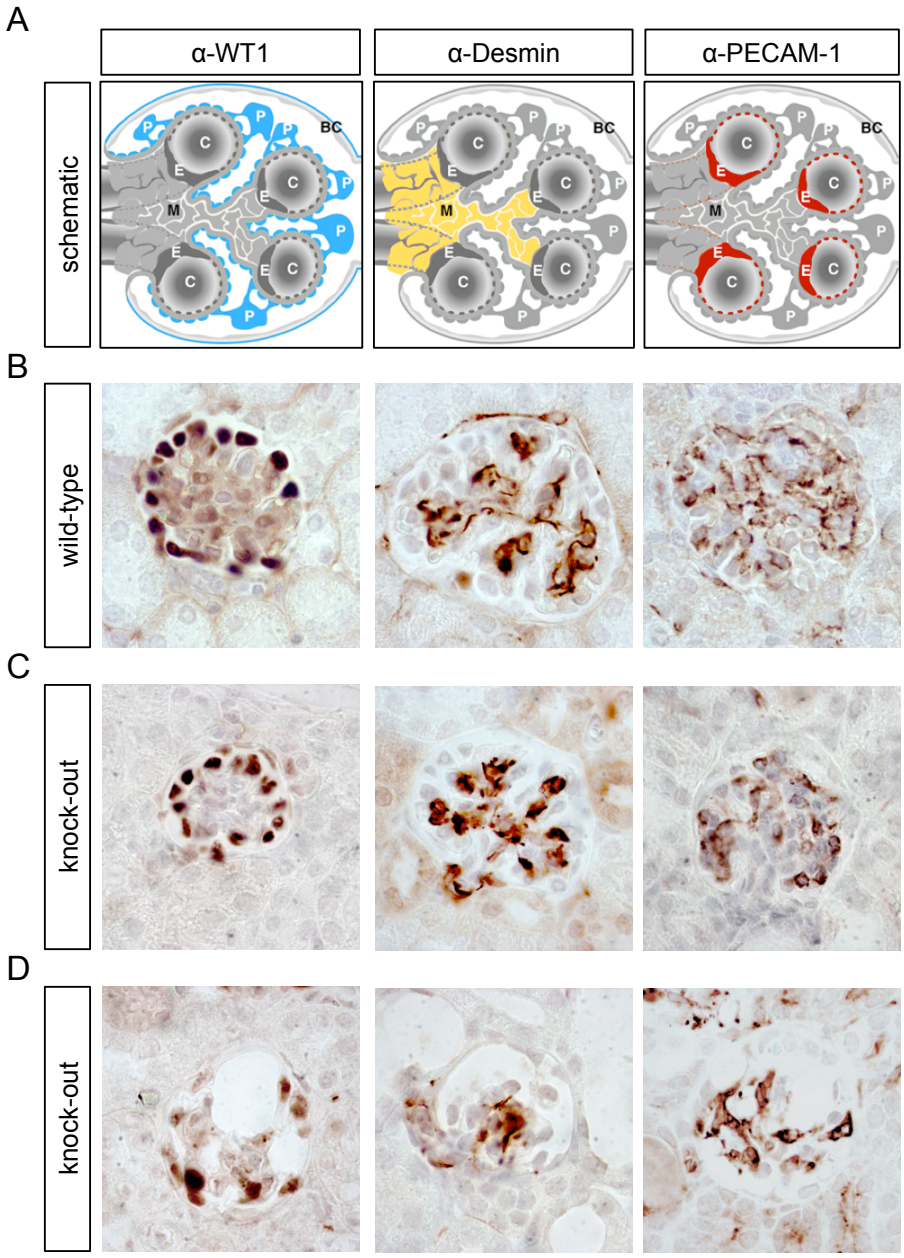

Figure 3.23 Glomerular marker analysis
A. Schematic view; podocytes (P) and parietal epithelial cells (gray) lining the Bowman's capsule (BC) are labeled by α-Wilms' tumor (WT1) antibody (left). Mesangial cells (M) are labeled by α-Desmin antibody (middle). Fenestrated endothelial cells (E) of the capillary loops (C) are labeled by α-PECAM-1 antibody (right). Modified after [Quaggin and Kreidberg, 2008] **B**. Staining pattern with the respective antibodies in wild-type glomeruli **C**. Staining pattern with the respective antibodies in unaffected glomeruli of *Slitl2*$^{-/-}$ kidneys **D**. Staining pattern with the respective antibodies in affected glomeruli of *Slitl2*$^{-/-}$ kidneys (Magnification 100$\times$ in panels **B**–**D**)

3.3.2.3 Transmission electron microscopic examination

In order to evaluate ultrastructural changes within affected mutant glomeruli, kidneys of *Slitl2*-deficient mice were subjected to transmission electron microscopic (TEM) examination. At low magnification, wild-type and unaffected mutant glomeruli showed a normal structure with capillaries, podocytes, and mesangial cells distinguishable within the Bowman's capsule. Initial changes, however, could be evidenced by the presence of multiple erythrocytes within ectatic capillaries of the mutant glomeruli. In contrast, affected glomeruli of *Slitl2*-deficient mice revealed marked changes already at low magnification. The entire glomeruli were abundantly filled with mostly electron-dense material. This equally involved the capillary lumen as well as the Bowman's space (Figure 3.24 A). At higher magnification, wild-type glomeruli displayed a regular structure of the glomerular basement membrane (GBM) and a normal podocyte architecture with well-defined foot processes. Slit-like openings on both sides of the GBM were apparent: fenestrated endothelial cells on the one side and filtration slits between adjacent foot processes on the other. In affected glomeruli of *Slitl2*-deficient animals, however, massive podocyte foot process effacement could be observed. In fact, most of the foot processes had fused to form a dense layer on top of the GBM, resulting in a complete loss of slit diaphragms (Figure 3.24 B).

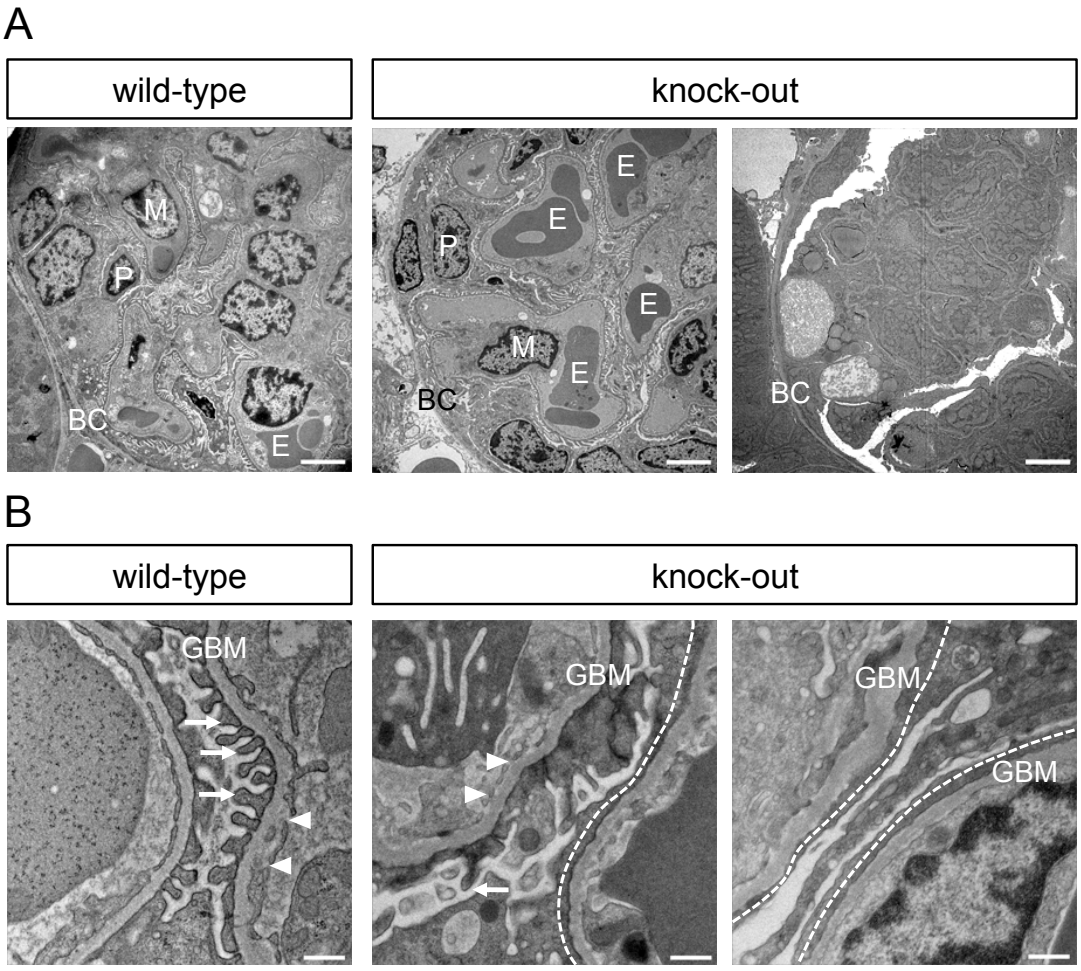

Figure 3.24 Transmission electron microscopic (TEM) examination of kidneys
A. Low magnification; wild-type and unaffected glomeruli of *Slitl2*-deficient mice showed a comparable structure (left and middle, respectively), while affected glomeruli of *Slitl2*-deficient mice were abundantly filled with mostly electron-dense material (right). BC, Bowman's capsule; E, erythrocyte; M, mesangial cell; P, podocyte (Scale bar: 3500 nm) **B**. High magnification; wild-type glomerulus showing fenestrated endothelium and podocyte foot processes (left); affected glomeruli of *Slitl2*-deficient mice displayed massive podocyte foot process effacement (middle and right). GBM, glomerular basement membrane; arrows indicate foot processes; arrowheads indicate fenestrated endothelium; dashed lines indicate foot process effacement. (Scale bar: 500 nm)

3.3.2.4 SDS-PAGE urinalysis

Glomerular diseases are known to be associated with protein leakage into the urine. In the healthy kidney, the glomerular basement membrane functions as a size-selective filtration barrier that retains albumin and other plasma proteins in the circulation. To evaluate to what extent the compromised integrity of the *Slitl2*$^{-/-}$ glomeruli affected protein permeability, the amount of urinary proteins at various stages of postnatal development was visualized by sodium dodecyl sulfate polyacrylamide gel electrophoresis (SDS-PAGE) and subsequent staining with PageBlue™ Protein Staining Solution (Fermentas). One week after birth, a faint protein band of approximately 55 kDa was detected in all samples analyzed irrespective of the genotype (Figure 3.25 A). At postnatal day 10, this band was no longer apparent in most cases. It only persisted in some, but not all, null mutants and was already more pronounced in a subset of these. Two weeks after birth, this assay revealed several protein bands for all *Slitl2*$^{-/-}$ mice, whereas all lanes of control animals were virtually devoid of such bands (Figure 3.25 B). Thus, by this stage, it was already possible to discriminate null mutants from wild-type or heterozygous littermates solely based on this analysis. The amount and composition of urinary protein, mainly consisting of albumin, further increased, reaching extremely high levels in moribund *Slitl2*-deficient mice (Figure 3.25 C).

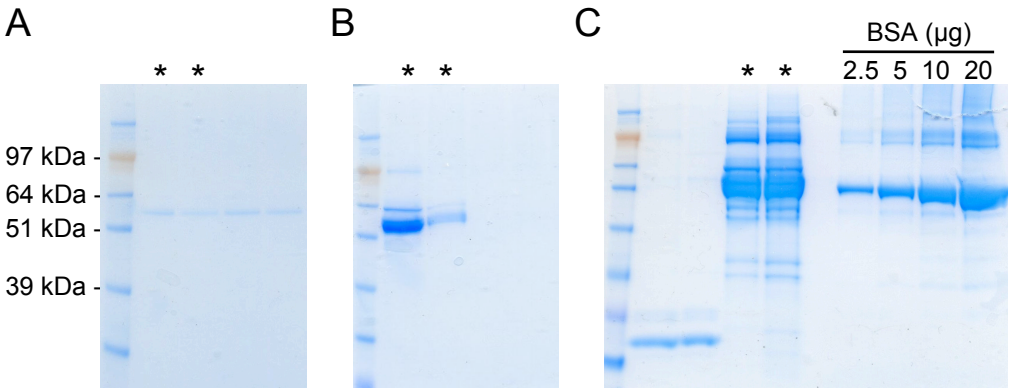

Figure 3.25 Progressive proteinuria in *Slitl2*-deficient mice
A. SDS-PAGE urinalysis revealed no difference between *Slitl2*-deficient mice (*) and control mice at postnatal day 7. **B**. By postnatal day 14, the samples from *Slitl2*-deficient mice (*) showed varying amounts of protein. No bands were detected in the urine of control mice. **C**. Massive proteinuria, mainly consisting of albumin, was observed in moribund *Slitl2*-deficient mice (*) at postnatal day 25. Albumin standards (BSA) were loaded as control.

3.3.2.5 Biochemical parameters of kidney function

Urinary albumin/creatinine ratio To estimate the glomerular filtration rate (GFR) and to compensate for variations in urine concentration when assessing urinary protein excretion in randomly collected samples, urinary creatinine and albumin levels were evaluated using commercially available kits (Parameter™ (R&D Systems) and AssayMax Mouse Albumin ELISA Kit (Assaypro), respectively). Creatinine is a metabolic waste product of creatine phosphate in the muscle. It is mainly excreted by glomerular filtration without being reabsorbed along the tubular system and is usually produced at rather constant rates depending on the body muscle mass. It therefore provides a rough estimate of the glomerular filtration rate in randomly collected urine samples.

The median creatinine concentration in 17- to 24-day-old *Slitl2*-deficient mice (n=14) was decreased to less than 50% in comparison to that of their wild-type littermates (n=14), corresponding to 10.50 mg/dl and 21.30 mg/dl, respectively (Figure 3.26 A). The median albumin concentration, on the other hand, determined in the same samples that were used for the creatinine assay, exceeded the control level by far. In fact, despite a 100-fold dilution, the levels of the *Slitl2* mutants were above the detection limit of the test, i.e., above the highest standard, and could therefore not be evaluated exactly due to saturation of the test. Thus, while the median urinary albumin concentration for the wild-type controls was 9.86 μg/ml, the level in the *Slitl2*-deficient mice exceeded 40 μg/ml (Figure 3.26 B). Accordingly, the urinary albumin/creatinine concentration in the mutants could not be calculated precisely. Nonetheless, an increase of more than 5.6-fold in comparison to the wild-type controls (61.79 μg/mg) could be stated for the *Slitl2*-deficient mice (Figure 3.26 C).

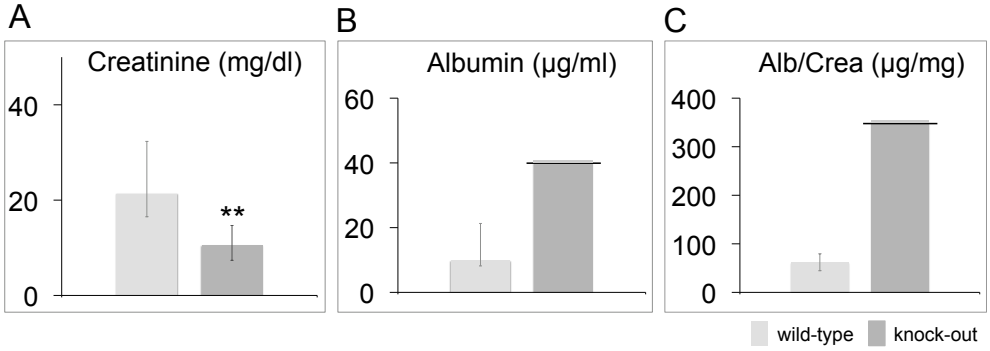

Figure 3.26 Urinary albumin/creatinine ratio
A. The median urinary creatinine concentration in *Slitl2*-deficient mice was decreased to less than 50% of that of wild-type controls. **B**. The median urinary albumin concentration was increased more than 4-fold in *Slitl2*-deficient mice in comparison to wild-type controls. **C**. The median urinary albumin/creatinine ratio was increased more than 5.6-fold in *Slitl2*-deficient mice in comparison to wild-type controls (n=14). Error bars indicate ±IQR. ** *P*-value of < 0.01; horizontal line in **B** and **C** indicates that detection limit was exceeded for the albumin test.

Serum albumin In order to evaluate to what extent serum albumin was affected by proteinuria in *Slitl2*-deficient mice, serum albumin levels were measured via a competitive sandwich enzyme immunoassay (AssayMax Mouse Albumin ELISA Kit; Assaypro). Severe hypalbuminemia was detected in 23-day-old null mutants (n=8). Their median serum albumin level was decreased to approximately 33% of that of the wild-type controls (n=8), accounting for 8.02 mg/ml and 24.19 mg/ml, respectively (Figure 3.27).

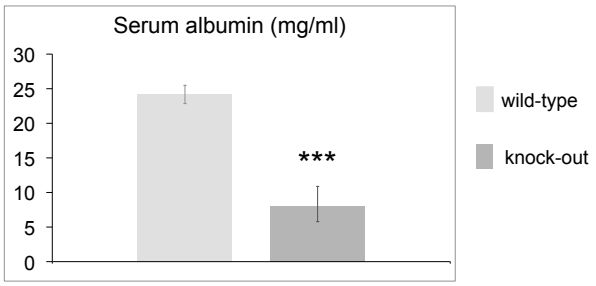

Figure 3.27 Serum albumin concentration
The median serum albumin concentration in *Slitl2*-deficient mice was decreased to approximately 33% of that of the controls (n=8). Error bars indicate ±IQR. *** *P*-value of < 0.001

Serum urea Due to a reduced filtration rate, glomerular diseases interfere with the clearance of metabolic waste products, thus they begin to build up in the circulation. Urea originates from protein catabolism and is eliminated from the body via the kidney under healthy conditions. Elevated serum urea levels therefore indicate the presence of renal insufficiency. Serum urea concentrations of 19- to 23-day-old *Slitl2*$^{-/-}$ mice (n=8) and control littermates (n=8) were evaluated with an automated blood analyzer. The median level was increased more than 2-fold in the *Slitl2*-deficient animals in comparison to the controls, corresponding to 97.00 mg/dl and 47.50 mg/dl, respectively (Figure 3.28).

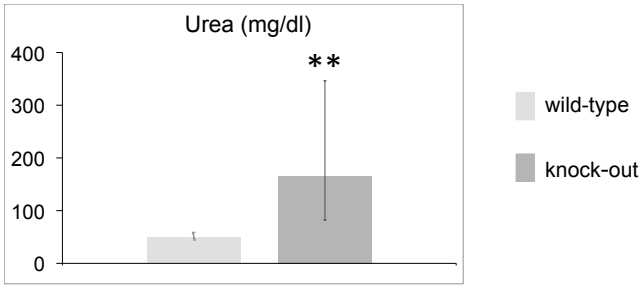

Figure 3.28 Serum urea concentration
The median serum urea concentration was increased over 2-fold in *Slitl2*-deficient mice compared to control littermates (n=8). Error bars indicate ±IQR. ** *P*-value of < 0.01

3.3.3 Bone phenotype of *Slitl2*-deficient mice

3.3.3.1 Skeleton staining

The analysis in *Slitl2-LacZ* as well as in *Slitl2-Venus* mice revealed strong reporter gene expression in the developing skeletal system from embryonic day 12.5 onwards, and this expression persisted to the adult stage (subsection 3.1.2 and subsection 3.1.3). This, in conjunction with the consistently smaller stature of *Slitl2*-deficient mice, prompted a more detailed analysis of the skeletal system in these animals. Therefore, bone and cartilage tissue was stained with alizarin red and alcian blue, respectively. Whole-mount specimens showed a proportionately reduced size yet normal overall anatomy of *Slitl2*$^{-/-}$ skeletons in comparison to that of wild-type littermates (Figure 3.29).

Figure 3.29 Comparison of skeletons
Bones and cartilage of 21-day-old mice were stained with alizarin red and alcian blue, respectively. The skeleton of the *Slitl2*-deficient mouse (bottom) showed a reduced size but normal overall anatomy in comparison to a wild-type littermate.

3.3.3.2 Micro-computed tomography

Under physiological conditions, bone formation and bone resorption are two tightly coupled processes. In a growing skeleton, mineralized bone formation exceeds bone resorption, whereas in the mature bones of a healthy young adult, bone loss and bone formation are equivalent, thereby preserving the structural integrity of the bone. Reduced bone formation or excessive bone resorption thus induce net loss of bone mass and increase the risk of bone fractures.

The above listed findings strongly suggested an altered bone metabolism in *Slitl2*-deficient mice. Initial micro-computed tomography (μCT) scans of femurs collected from 25-day-old male *Slitl2-null* mice further substantiated this presumption. In comparison to an age- and gender-matched wild-type femur, less trabecular bone was detected in the epi- and metaphyseal region of the homozygous *Slitl2*$^{-/-}$ bone (Figure 3.30 A). In addition, the three-dimensional (3D) reconstructions revealed anomalies of the shaft region, i.e., the diaphysis. The mutant bone clearly exhibited a thinner cortex as well as a reduced diameter (Figure 3.30 B).

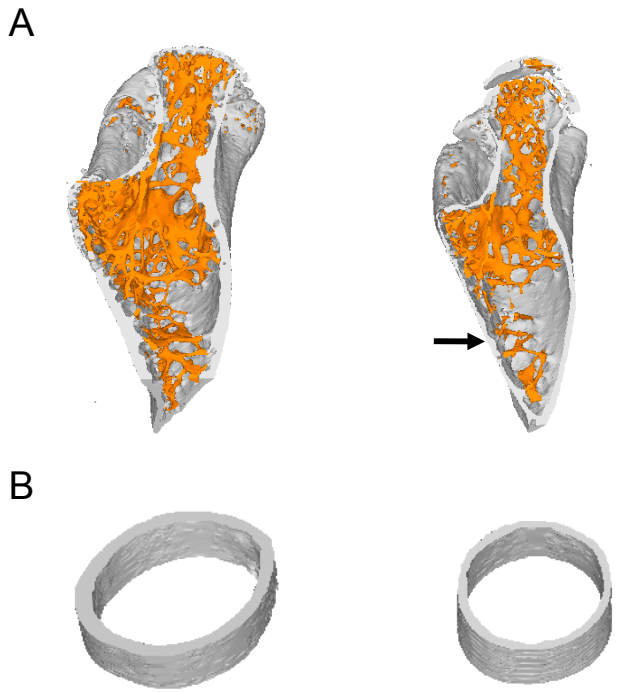

Figure 3.30 3D reconstruction of micro-computed tomography (μCT) of femurs
A. Cross section of proximal femur showing less trabecular bone (orange) and a thinner cortex (arrow) in the *Slitl2*-deficient mouse (right) in comparison to that of an age- and gender-matched wild-type mouse (left). **B**. Cross section of diaphysis showing reduced diameter and thinner cortical bone in the *Slitl2* mutant (right) in comparison to the wild-type control (left). (Image courtesy of Dr. Marco Eijken)

3.3.3.3 Biochemical parameters of calcium homeostasis

Bones largely consist of an inorganic component, namely hydroxyapatite crystals, which themselves are composed of phosphate and calcium. Almost all body calcium is stored in the bones. Serum calcium only represents about 1% of total body calcium and exists in two forms, namely ionized and unionized, protein-bound calcium. The serum calcium level is usually maintained within a very narrow range and is adjusted via a hormonal control loop. If serum calcium levels drop, parathormone (PTH) is released from the parathyroid glands. PTH exerts multiple functions to restore calcium homeostasis in the blood. It activates osteoclasts, thereby causing the release of calcium from the bones, and increases calcium reabsorption in the kidneys. It also indirectly enhances calcium absorption in the intestine by stimulating the activation of vitamin D in the kidneys, which is required for intestinal calcium uptake.

Serum calcium levels The results from the micro-computed tomography indicated a disturbed calcium metabolism in *Slitl2*-deficient mice. Indeed, the median ionized serum calcium level – evaluated by an automated blood analyzer – was significantly decreased in 19- to 23-day-old mutant mice (n=5), corresponding to 1.83 mmol/l as opposed to 2.78 mmol/l in the control animals (n=5) (Figure 3.31 A).

Urinary calcium levels In order to assess whether serum calcium levels were decreased due to excessive urinary loss owing to the observed kidney defects in *Slitl2*-deficient mice, urinary calcium levels were determined using the commercially available Quantichrom Calcium Assay Kit (Gentaur). The median urinary calcium level in 20- to 26-day-old null mutants was decreased to approximately 24% of that of the wild-type controls, reaching only 5.76 mg/dl (n=12) compared to 23.71 mg/dl (n=12), respectively (Figure 3.31 B).

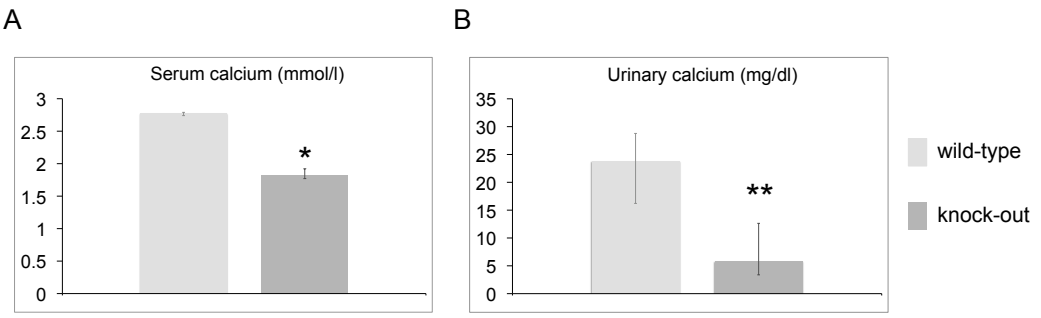

Figure 3.31 Serum and urinary calcium concentrations
A. The median serum calcium concentration in *Slitl2*-deficient mice was decreased to approximately 65% of that of the controls (n=5). **B**. The median urinary calcium concentration in *Slitl2*-deficient mice was decreased to about 24% of that of the wild-type controls (n=12). Error bars indicate ±IQR.
* *P*-value of < 0.05 ** *P*-value of < 0.01

Serum vitamin D Both the serum and the urinary calcium levels were found to be decreased in *Slitl2*-deficient mice. As bioactive vitamin D, i.e., 1,25-dihydroxycholecalciferol, is needed for efficient intestinal absorption of dietary calcium, its serum levels were measured using a commercially available radioimmunoassay kit (Gamma-B 1,25-Dihydroxy Vitamin D RIA Kit; IDS, Boldon, UK). In 24- to 26-day-old *Slitl2*-deficient mice, the median serum level of active vitamin D was decreased to 17% of that of the wild-type controls, accounting for 43.00 pmol/l (n=9) and 243.00 pmol/l (n=9), respectively (Figure 3.32).

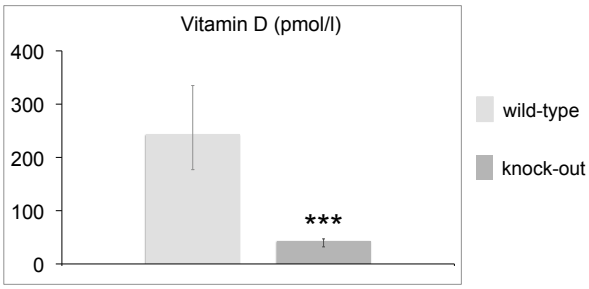

Figure 3.32 Serum vitamin D concentration
The median serum concentration of bioactive vitamin D (1,25-dihydroxcholecalciferol) in *Slitl2*-deficient mice was decreased to about 17% of that of the wild-type controls (n=9). Error bars indicate ±IQR.
*** *P*-value of < 0.001

3.3.4 Thymus and spleen phenotype of *Slitl2*-deficient mice

3.3.4.1 Histological examination

At dissection, all moribund *Slitl2*-deficient mice exhibited disproportionally small thymi and spleens (Figure 3.20). Histological examination of tissue sections stained with hematoxylin and eosin (H&E) revealed hypocellularity of both organs from terminally ill *Slitl2*-deficient mice.

In wild-type thymi, the cortical and medullary regions were readily distinguishable after H&E staining. The peripheral cortex harbors a large number of immature T cells and therefore stains darker than the less densly populated central medulla. In contrast, thymi of moribund *Slitl2*-deficient mice revealed an inverse staining pattern with a lighter stained cortical region, indicating a marked depletion of lymphocytes in this area (Figure 3.33 A).

The spleens of wild-type control animals showed a normal parenchymal architecture with its two major compartments, namely the red pulp and the white pulp. The red pulp is predominantely composed of blood-filled sinuses, whereas the white pulp is formed by lymphoid tissue. The white pulp regions are located around central arterioles and comprise both T- and B-cell rich areas. These darkly stained regions of concentrated lymphocytes were evenly distributed and clearly recognizable in control organs but appeared extremely disorganized in the spleens of moribund *Slitl2*$^{-/-}$ mice (Figure 3.33 B).

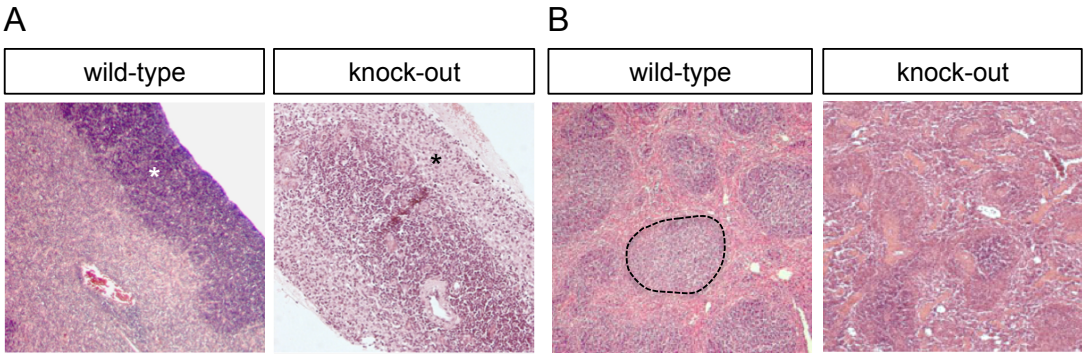

Figure 3.33 Thymus and spleen histopathology of *Slitl2*-deficient mice; H&E staining **A**. The cortical region (asterisks) was largely depleted in the thymus of a moribund *Slitl2*-deficient mouse (right; magnification 20×) in comparison to that of a wild-type control animal (left; magnification 5×). **B**. Spleen of a moribund *Slitl2*-deficient mouse (right; magnification 20×) showing a disrupted tissue organization in comparison to that of a wild-type mouse (left; magnification 5×). Dashed circle exemplifies white pulp region.

3.3.4.2 Complete blood counts

To assess whether the alterations observed in the histology of the lymphoid organs of moribund *Slitl2*-deficient mice were also reflected in the composition of the peripheral blood, samples were collected by puncture of the retroorbital sinus. Complete blood counts of 22- to 23-day-old mice showed a normal red blood cell (RBC) count in *Slitl2*$^{-/-}$ mice (n=7) in comparison to their wild-type littermates (n=7). The total white blood cell (WBC) counts, however, were dramatically different. The blood of wild-type mice contained approximately 8,000 leukocytes/μl on average as opposed to only 1,400 cells/μl in the moribund mutants. The differential WBC count displayed the changes in more detail. In wild-type samples, lymphocytes constituted by far the largest fraction of all leukocytes (87%), followed by neutrophils (10%). Monocytes, basophils, and eosinophils were virtually absent. In contrast, neutrophils and lymphocytes accounted for 43% and 36% of all white blood cells in *Slitl2*$^{-/-}$ mice, respectively. Also, the basophilic and eosinophilic fractions were relatively elevated, with the latter in fact exceeding that of wild-type samples in absolute numbers despite the strongly reduced total WBC count in the mutants (Table 3.1). Moreover, the mean number of thrombocytes was increased in *Slitl2*-deficient mice ($987 \times 10^3/\mu$l) in comparison to the wild-type controls ($659 \times 10^3/\mu$l).

	RBC	**WBC**	**differential WBC count** (cells/μl)				
	($1\times10^6/\mu$l)	($1\times10^3/\mu$l)	lymphocytes	neutrophils	monocytes	basophils	eosinophils
wild-type	6.98	8.09	7065	794	103	118	6
(n=7)			87%	10%	1%	2%	0%
knock-out	7.01	1.40	952	363	44	13	28
(n=7)			43%	36%	7%	3%	11%

Table 3.1 Blood counts of wild-type and *Slitl2*-deficient mice (RBC: red blood cells; WBC: white blood cells)

3.3.4.3 Flow cytometry

In order to study the onset and nature of the decreased lymphocyte counts in *Slitl2*-deficient mice, isolated lymphocytes were subjected to flow cytometric analysis. For this method, cells of interest are incubated with fluorochrome-labeled

marker antibodies before analyzing them with a flow cytometer. This machine detects how cells scatter incident laser light and emit fluorescence of specific wavelengths corresponding to the fluorochrome labels of the coupled antibodies. Thus, subpopulations of cells expressing defined combinations of marker proteins can be identified.

Two 19-day-old *Slitl2*$^{-/-}$ mice without apparent atrophy of spleen and thymus and two 24-day-old mutants with marked reduction in splenic and thymic size were each analyzed in conjunction with two wild-type littermates. Thymocytes, splenocytes, and bone marrow cells were harvested and stained with a combination of fluorochrome-labeled antibodies that allowed for discrimination of various cell subpopulations of the respective tissue. The fluorescent signals were analyzed with a FACSCalibur™ Flow Cytometer (BD Biosciences), and the collected data were processed with the FlowJo software (Tree Star).

In addition, total thymic and splenic cell numbers in the 24-day-old mice were evaluated using a conventional hemocytometer. The mean total thymocyte number in the wild-type and the knock-out mice was 138×10^6 and 2.3×10^6, respectively. The mean total splenic cell number showed an equally high difference, accounting for 44×10^6 and 0.7×10^6 in the wild-type and the *Slitl2*$^{-/-}$ mice, respectively. This corresponded to a reduction of more than 98% in total cell numbers for both organs in the mutant mice in comparison to the wild-type controls.

T lymphocytes T-cell development occurs in the thymus. Lymphoid progenitors migrate from the bone marrow to the thymus where they complete their maturation. During this process, thymocytes pass through a series of distinct stages which are classified according to the expression of various cell surface markers including the coreceptors CD4 and CD8. T-cell precursors are initially negative for both markers (CD4$^-$/CD8$^-$ T cells), then express both simultaneously (CD4$^+$/CD8$^+$ T cells), while mature T cells either express CD4 or CD8 (CD4$^+$ or CD8$^+$ T cells). The CD4$^+$/CD8$^+$ subpopulation usually constitutes the vast majority of all thymocytes as was the case for the wild-type and the 19-day-old *Slitl2*$^{-/-}$ mice. In these animals, more than 76% of all thymocytes expressed both markers. In the 24-day-old *Slitl2*-deficient mice, however, this subpopulation was almost completely absent, accounting for only 4% of all cells in the representative sample (Figure 3.34 A).

Early in T-cell development, two distinct lineages are formed which express

different types of T-cell receptors (TCR). In the majority of T lymphocytes, this receptor is composed of an α- and a β-glycoprotein chain. $CD4^+/CD8^+$ cells initially lack TCR expression. As they mature into $CD4^+$ or $CD8^+$ T cells, TCR expression is increased stepwise from intermediate to high levels. During this development, the cells transiently express the early activation marker CD69. In general, the major part of $CD4^+/CD8^+$ T cells is characterized by low to intermediate TCR expression levels and does not yet express CD69. Over 65% of total thymocytes belonged to this subpopulation in the wild-type as well as the unaffected *Slitl2*-deficient thymi. In contrast, this population was largely depleted in the 24-day-old moribund *Slitl2*$^{-/-}$ mice, comprising less than 8% in the representative sample (Figure 3.34 B).

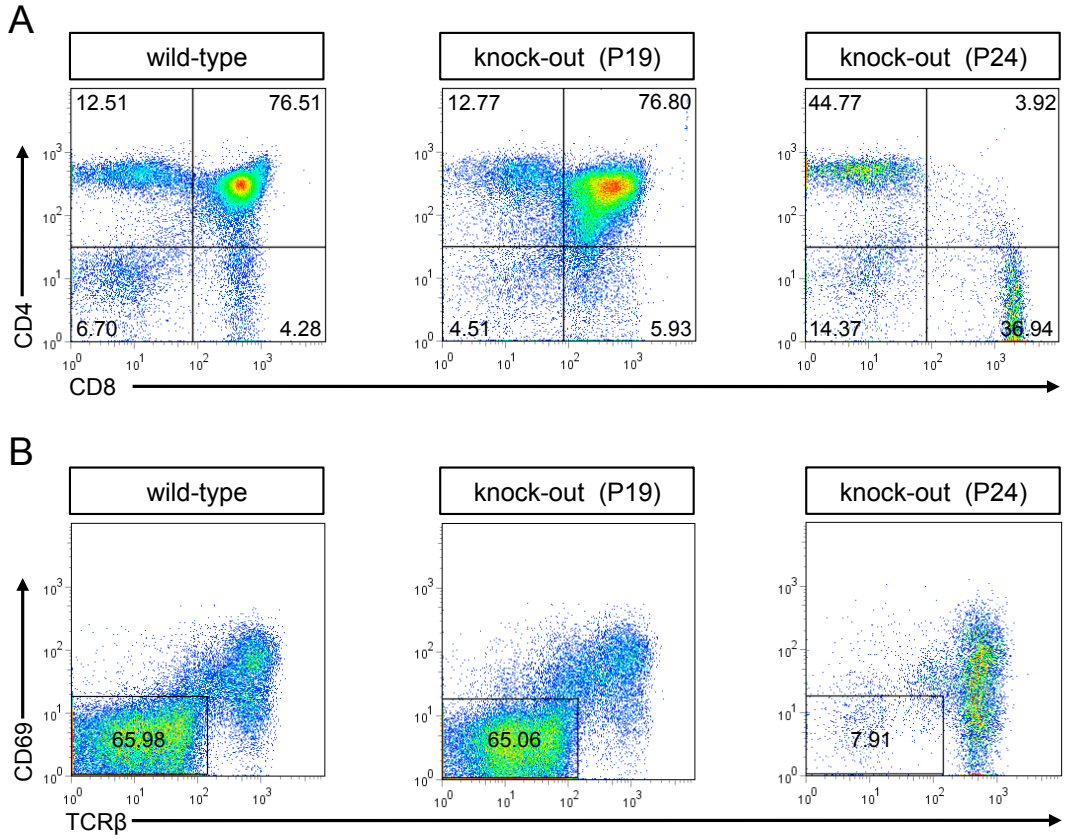

Figure 3.34 Flow cytometric analysis of T cells; representative data
A. $CD4^+/CD8^+$ T cells (upper right quadrant) were largely depleted in 24-day-old *Slitl2*-deficient mice (P24; right) in comparison to wild-type (left) and 19-day-old *Slitl2*-deficient mice (P19; middle). **B**. The $CD69^-/TCR^{-/int}$ subpopulation of $CD4^+/CD8^+$ T cells (inset) was largely absent in 24-day-old *Slitl2*-deficient mice (right) in comparison to wild-type (left) and 19-day-old *Slitl2*-deficient mice (middle). Numbers represent percentage of total cells.

B lymphocytes B-cell development begins in the fetal liver and continues in the bone marrow throughout adult life. B220 is one of the first identifiable B-cell lineage markers. It is continuously expressed from the pro-B-cell stage onwards. At the subsequent pre-B-cell stage, the cells start to express a pre-B-cell receptor which is composed of intact heavy chains and surrogate light chains. At this phase, the receptor is mainly expressed intracellularly, thus it can not yet be detected on the cell surface by fluorochrome-labeled antibodies. Once complete immunoglobulin (IgM) receptor molecules appear at the cell surface, the cells are defined as immature B lymphocytes. The flow cytometric profiles of the wild-type and 19-day-old *Slitl2*-mutant mice exhibited both pro-/pre-B as well as immature B cells in the bone marrow, while in the older mutants, the pro-/pre-B-cell subpopulation was almost completely absent, constituting less than 2% in the representative sample. (Figure 3.35 A).

Immature B cells leave the bone marrow to complete their development in peripheral lymphoid tissues. The cells undergo further differentiation and now express surface IgD in addition to IgM molecules. Mature B lymphocytes can be subdivided based on the expression of two cell surface markers, namely CD21 and CD23. Follicular B cells from the splenic white pulp regions are characterized by high expression levels of both proteins. They could be clearly demarcated as a distinct population in the control animals but were reduced by more than 50% in the representative sample of the 24-day-old *Slitl2*-mutant mice (Figure 3.35 B).

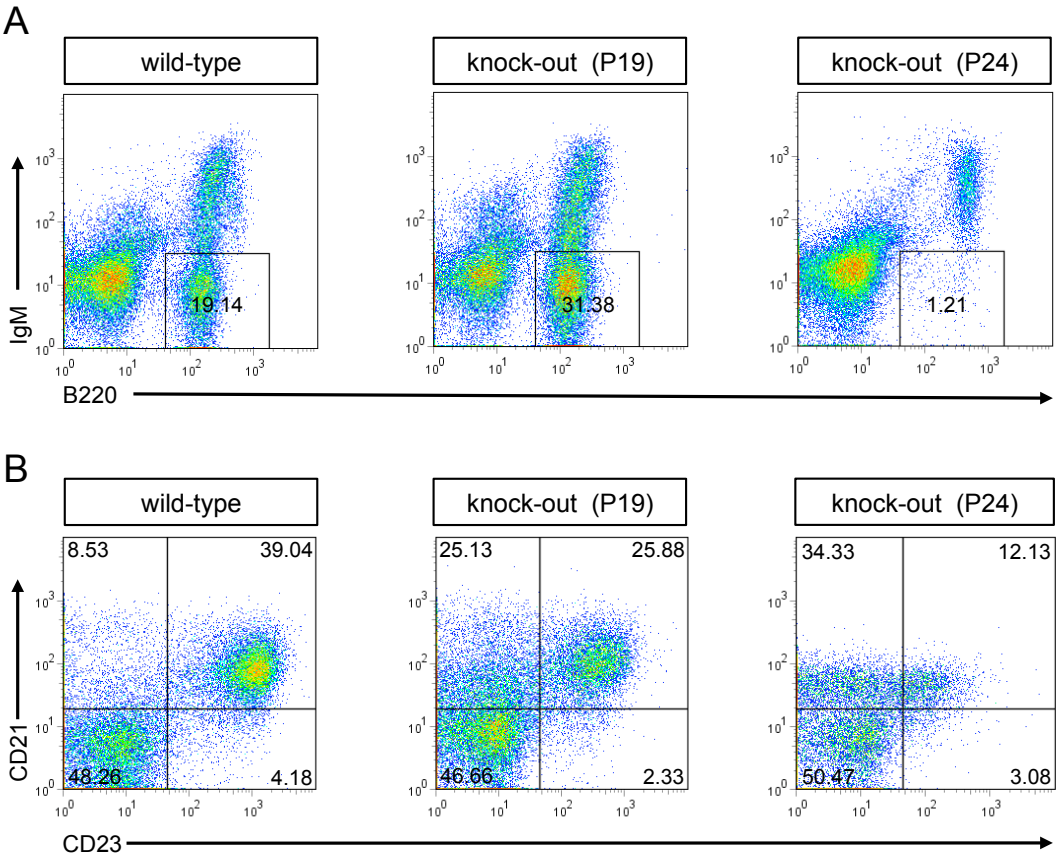

Figure 3.35 Flow cytometric analysis of B cells; representative data
A. In the bone marrow, the pro-/pre-B-cell subpopulation ($B220^{lo}/IgM^{-}$, inset) was almost completely absent in 24-day-old *Slitl2*-deficient mice (P24; right) in comparison to wild-type (left) and 19-day-old *Slitl2*-deficient mice (P19; middle). **B**. In the spleen, follicular B cells ($CD21^{++}/CD23^{++}$, upper right quadrant) were largely depleted in 24-day-old *Slitl2*-deficient mice (right) in comparison to wild-type (left) and 19-day-old *Slitl2*-deficient mice (middle). Numbers represent percentage of total cells.

3.3.4.4 Serum corticosterone

It has been reported that elevated levels of corticosterone can cause apoptosis of lymphocytes. Indeed, both the B- and the T-cell lineage are known to be affected by this stress-related hormone [Barone et al., 1993] [Laakko and Fraker, 2002]. The release of this hormone is governed by the hypothalamic-pituitary-adrenal (HPA) axis. The paraventricular nucleus of the hypothalamus secretes cortico-tropin-releasing hormone (CRH) which stimulates the release of adreno-corticotropic hormone (ACTH) from the anterior lobe of the pituitary gland. ACTH, in turn, acts on the adrenal cortices by inducing the production of gluco-corticoid hormones, which is mainly corticosterone in rodents. The levels of this hormone show a circadian rhythm and rise instantaneously in response to stress.

To minimize these influences when assessing corticosterone levels in 25-day-old *Slitl2-null* mice, all animals were put in individual cages the afternoon before blood sampling the next morning. No longer than three minutes passed between first handling the cage and collecting the sample. Serum corticosterone levels were then measured using a commercially available corticosterone ELISA kit (IBL). The median corticosterone level in the *Slitl2*-deficient animals was 214.32 ng/ml (n=5), while reaching only 9.98 ng/ml in the wild-type controls (n=5). This corresponded to an increase of more than 21-fold in the mutant mice (Figure 3.36).

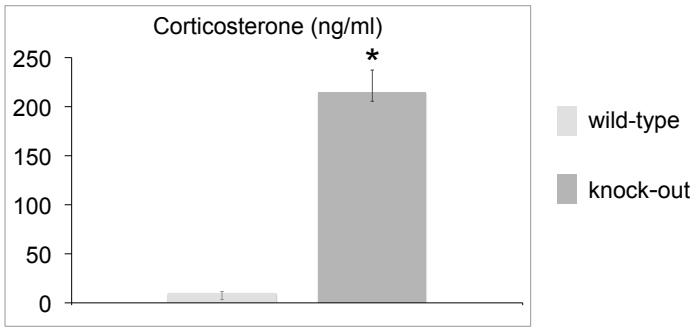

Figure 3.36 Serum corticosterone concentration
The median serum corticosterone concentration in *Slitl2*-deficient mice was increased 21-fold in comparison to the wild-type controls (n=5). Error bars indicate ±IQR. * *P*-value of < 0.05

3.4 Gene expression profiling

3.4.1 cDNA microarray analysis

To identify and characterize gene expression changes associated with *Slitl2* inactivation, genome-wide expression patterns in tissues from *Slitl2*$^{-/-}$ and wild-type littermates were compared by cDNA microarray analysis. This method involves the isolation of RNA from a tissue of interest, which is converted into a fluorescently labeled cRNA target. It is then hybridized to probe DNA, i.e., short sequences corresponding to specific genes, that have been attached, in a known configuration, onto microscopic spots. Binding of the target to its complementary probe is quantified by detection of the fluorescent label, reflecting the relative abundance of a particular sequence in the sample. Comparison of hybridization patterns from different samples thus allows identification of differentially expressed genes.

For this study, total RNA was extracted from thymi and spleens of 22- to 23-day-old *Slitl2*-deficient mice and from kidneys of 15-day-old *Slitl2*-deficient mice and their wild-type littermates to produce biotinylated cRNA, which was then hybridized to Illumina MouseRef-8 BeadChips. All tissues were analyzed in biological quadruplicates, i.e., the data of four mutant and four wild-type samples were combined.

3.4.1.1 Cluster analysis dendrograms

After normalization of the data, they were clustered to depict the average linkage between the different samples of a respective tissue. If one was to expect great overall differences in gene expression between the wild-type and the knock-out samples, the biological replicates should cluster together as was the case for the thymus samples analyzed. Here, they formed two distinct groups in which the four wild-type and the four *Slitl2*$^{-/-}$ replicates were highly similar among themselves but as a group only distantly related to the other one (Figure 3.37 A). The same analysis for the spleen samples revealed that the expression pattern of one of the four knock-out replicates was more similar to the wild-type replicates, which nevertheless were most similar among themselves (Figure 3.37 B). For the kidney samples, however, no clear distinction was apparent between control and knock-out samples. Two *Slitl2*$^{-/-}$ replicates each clustered together in pairs with one forming a group with three linked wild-type samples and the other pair showing an

expression pattern more similar to the remaining control replicate (Figure 3.37 C).

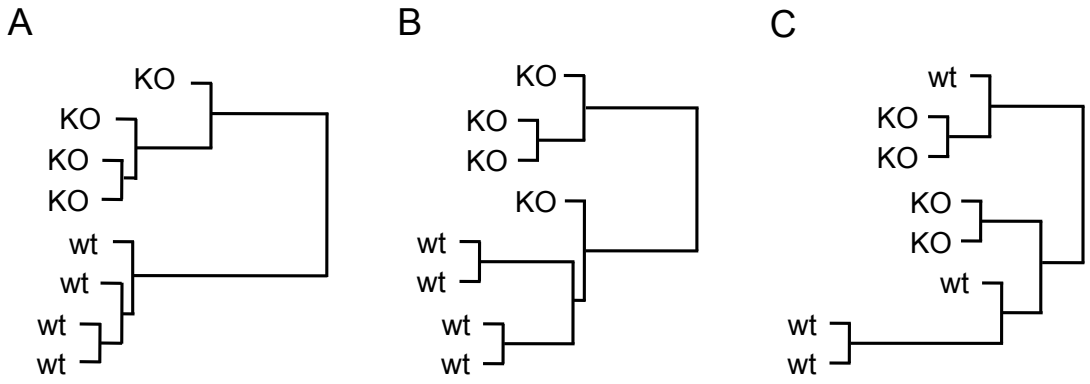

Figure 3.37 Cluster analysis dendrograms of cDNA microarray analyses
A. Thymus microarray **B**. Spleen microarray **C**. Kidney microarray
Dendrograms depict average linkage between the different replicates of *Slitl2*-deficient mice (KO) and wild-type littermates (wt).

3.4.1.2 Deregulated genes

Relative gene expression values in knock-out compared to wild-type samples were calculated from the cDNA microarray experiments applying quantile normalization and an adjusted P-value according to the method of Benjamini and Hochberg [Benjamini and Hochberg, 1995]. The number of significantly deregulated genes in the *Slitl2*$^{-/-}$ tissues were determined based on different thresholds. For the spleen and the kidney microarray data, an adjusted P-value of < 0.01 was used as initial cut-off. For the analysis of the thymus microarray data, a more stringent adjusted P-value of < 0.001 was applied given that a vast amount of genes was still classified as deregulated using this cut-off. The gene lists were then sorted according to the fold change in the knock-out relative to the control samples. In the *Slitl2*-deficient thymi, a great number of genes was detected that were either up- or downregulated at least 2-fold. After gradual increase of the threshold to 5-fold, 37 and 51 genes were still rated as up- and downregulated, respectively. When applying the 2-fold threshold for the spleen samples, 78 genes were detected as upregulated and 101 genes as downregulated in the knock outs. Using a 5-fold cut-off, both groups were narrowed down to only two genes, with *Slitl2* being one of the two downregulated genes. Compared to these two tissues, the *Slitl2*-deficient kidneys showed considerably less deregulated genes relative to the control group. Only 17 genes in total met the criterion of being upregulated more than 2-fold. Merely two genes remained when increasing the threshold to

more than 5-fold. Interestingly, only a single gene was significantly downregulated in the *Slitl2*$^{-/-}$ kidneys, namely *Slitl2* itself. Table 3.2 lists the number of deregulated genes when applying different fold-change thresholds.

Tissue	**adj.*P*-value**	**Fold change**	**upregulated**	**downregulated**
thymus	< 0.001	≥ 2	743	493
		≥ 3	262	185
		≥ 4	87	85
		≥ 5	37	51
spleen	< 0.01	≥ 2	78	101
		≥ 3	10	18
		≥ 4	6	6
		≥ 5	2	2
kidney	< 0.01	≥ 2	17	1
		≥ 3	7	1
		≥ 4	4	1
		≥ 5	2	1

Table 3.2 Numbers of significantly deregulated genes from cDNA mircoarray analyses

When collating the data for *Slitl2* from the three cDNA microarray experiments, marked variations in the degree of deregulation became apparent. Even though the adjusted P-value was < 0.001 in all tissues, it was comparatively high in the thymus microarray. This difference was also reflected in the fold change. *Slitl2* was only downregulated approximately 1.5-fold in the thymus, while showing a fold change of 5.2 in the mutant spleens. The extent of deregulation was even more pronounced in the knock-out kidneys. Here, *Slitl2* was downregulated more than 24-fold (Table 3.3).

Tissue	adj.*P*-value	Fold change
thymus	0.000737	1.5
spleen	0.000006	5.2
kidney	0.000001	24.1

Table 3.3 Degree of *Slitl2* deregulation from cDNA microarray analyses

3.4.1.3 Functional annotation clustering

To understand the biological meaning of the gene lists generated by the DNA microarray experiments, they were analyzed with the online available DAVID (Database for Annotation, Visualization, and Integrated Discovery) tool. Genes with a fold change of > 5 in the thymus microarray and of > 2 in the spleen microarray were used in this analysis. For the kidney microarray, all upregulated genes (n=19) with an adjusted P-value of < 0.01 were incorporated, including two genes with a fold change of only 1.8, namely *Trib3* (tribbles homolog 3) and *Areg* (amphiregulin). The lists were individually uploaded and subsequently analyzed with the functional annotation clustering module using the predefined high classification stringency. Annotation clusters with an enrichment score of > 3 along with an adjusted enrichment P-value (Benjamini) of < 0.05 were rated as relevant groups.

In the *Slitl2*-deficient thymi, the upregulated genes clustering according to the predefined classification were associated with the terms 'secreted' and 'extracellular space', while the downregulated genes constituting significant clusters were related to 'M phase', 'cytoskeleton', 'non-membrane bound organelle', 'microtubule', and 'nucleus'. When annotating the 78 genes upregulated more than 2-fold in the *Slitl2*$^{-/-}$ spleens, no significant clusters were formed. The downregulated genes in this tissue were associated with similar terms as in the mutant thymi. Most of the 101 genes were classified as 'intracellular', followed by 'metabolic process' and 'mitosis'. In the knock-out kidneys, two relevant clusters were defined despite the limited number of significantly deregulated genes. Four of the 19 genes were linked to 'MHC class II antigen processing and presentation', while five other genes were related to 'inflammatory response'. A list of all genes along with their annotated functional terms can be found from page 146 onwards.

3.4.2 Quantitative real-time PCR

To validate the results obtained from the cDNA microarray experiments, the expression levels of selected deregulated genes, namely *Bmp4* (bone morphogenetic protein 4), *Ctgf* (connective tissue growth factor), and *Flt1* (FMS-like tyrosine kinase 1) from the spleen microarray and *Areg* (amphiregulin), *Timp1* (tissue inhibitor of metalloproteinase 1), and *Tnfrsf12a* (tumor necrosis factor receptor superfamily, member 12a) from the kidney microarray, were reassessed by quantitative real-time PCR. The same RNA samples that had been used for the microarray assays served as template for this experiment. The RNA was first transcribed into cDNA using the SuperScript™ III First-Strand Synthesis System for RT-PCR (Invitrogen). Quantitative real-time PCR was performed with the Power SYBR® Green PCR Master Mix (Applied Biosystems), and the results were analyzed with the StepOnePlus™ Software. The housekeeping gene *Gapdh* (glyceraldehyde-3-phosphate dehydrogenase) was used for normalization of each sample. The results of three biological wild-type and knock-out samples, each run in technical triplicates, were combined to calculate relative quantity of gene expression in the *Slitl2*$^{-/-}$ tissues in comparison to the wild-type control group. The expression levels of all six selected genes were assayed in both the spleen and the kidney RNA samples.

In the *Slitl2*$^{-/-}$ spleen samples, all three genes that had been classified as upregulated in the spleen microarray (*Bmp4*, *Ctgf*, *Flt1*) showed increased expression levels in comparison to the control group, with *Ctgf* upregulated approximately 5-fold and *Bmp4* as well as *Flt1* upregulated more than 2-fold. Two of the three genes that had been selected due to deregulation in the kidney microarray, namely *Timp1* and *Tnfrsf12a*, also exhibited upregulation in the *Slitl2* knock-out spleens when assessed by quantitative real-time PCR. This increase, however, was rather moderate in both cases, not exceeding the 2-fold threshold. Expression of the remaining gene, *Areg*, was neither detected in the wild-type nor in the knock-out spleen samples. In contrast, none of the three genes selected from the spleen microarray displayed upregulation the *Slitl2*$^{-/-}$ kidney samples in comparison to the controls. Here, *Areg* showed the most pronounced increase of more than 6-fold, followed by *Timp1* ($>$ 5-fold) and *Tnfrsf12a* ($>$ 2.5-fold).

A

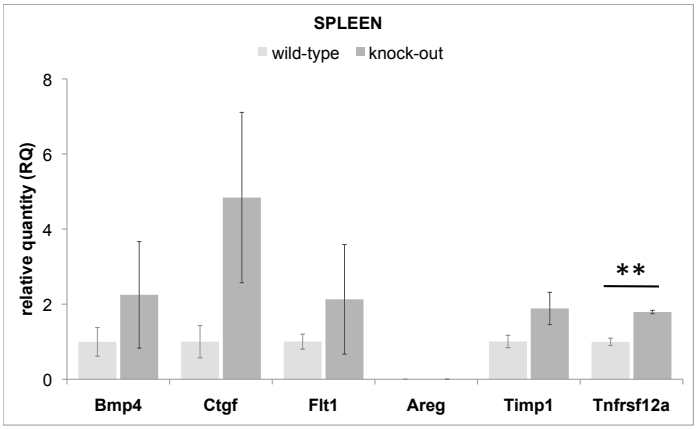

B

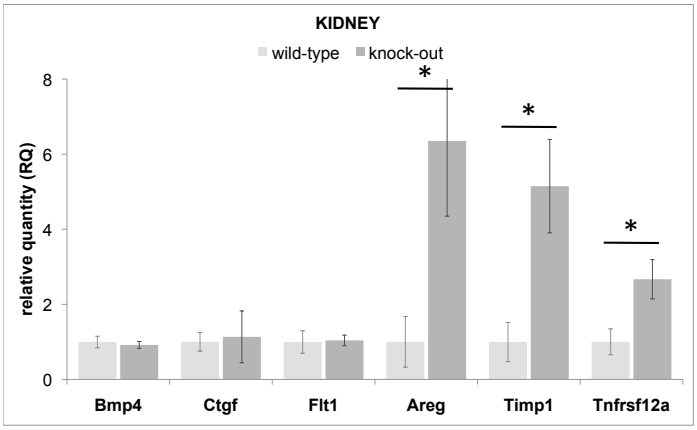

Figure 3.38 Quantitative real-time PCR

A. Relative quantity (RQ) of mRNA expression of the indicated genes relative to mRNA expression of the housekeeping gene *Gapdh* in wild-type and *Slitl2*-deficient spleens. **B**. Relative quantity (RQ) of mRNA expression of the indicated genes relative to mRNA expression of the housekeeping gene *Gapdh* in wild-type and *Slitl2*-deficient kidneys. Columns represent mean of three biological replicates. Error bars indicate ±SD (standard deviation). * *P*-value of < 0.05 ** *P*-value of < 0.01 (according to *t*-test with unequal variances)

4 Discussion

Expression pattern of *Slitl2* suggests multiple roles

This study provides a first extensive description of the Slit-like 2 (*Slitl2*) expression pattern in the mouse. Various strategies were adopted in order to obtain a comprehensive picture. An initial Northern blot analysis demonstrated *Slitl2* expression from early developmental through to adult stages and prompted a more detailed analysis. Expression of *Slitl2* at midgestation stages of mouse embryogenesis was verified by whole-mount *in situ* hybridization (WISH), a strategy, with which defined expression domains could first be identified. In order to evaluate endogenous *Slitl2* expression not only on the RNA, but also on the protein level, a rabbit polyclonal antibody was generated against its carboxy-terminal sequence. The affinity-purified anti-Slitl2 (α-Slitl2) antibody was able to discriminate between heterozygous *Slitl2*$^{+/-}$ and homozygous *Slitl2*$^{-/-}$ mouse primary embryonic fibroblast (MEF) cell lines in a Western blot assay conducted on lysates derived from these cells, thereby confirming the absence of Slitl2 protein in *Slitl2*-deficient cells. However, despite its predicted high binding capacity, it failed to render unambiguous results when employing it for immunocytochemical analysis of the subcellular localization of Slitl2 protein in MEF cells. Here, background staining could also be observed in *Slitl2*-deficient MEFs due to non-specific binding of the antibody.

To circumvent the limitations associated with studying endogenous *Slitl2* expression, two diverse approaches were chosen for the generation of two different reporter strains, namely *Slitl2-LacZ* knock-in and *Slitl2-Venus* transgenic mice. The *Slitl2-LacZ* strain was successfully employed to provide a comprehensive temporospatial expression pattern. This analysis not only confirmed the results from the WISH experiment, but also allowed for a more precise description down to a single-cell level. Ultimately, the expression of Venus, a variant of the yellow fluorescent protein (YFP) [Rekas et al., 2002], in *Slitl2-Venus* transgenic mice reflected and thus further corroborated the previous findings. Moreover, this strain allowed for localization of reporter gene expression in *Slitl2-Venus* transgenic kidneys. YFP and its variants are common reporter proteins, and well-working

antibodies are available for their detection, which provides an elegant way to evade the lack of a good α-Slitl2 antibody. In addition, transgene expression in *Slitl2-Venus* mice will serve as a useful tool for the isolation of Venus-positive cells from tissues of interest via fluorescence-activated cell sorting (FACS) for subsequent *in vitro* functional studies.

Taken together, all three approaches yielded consistent, therefore reliable results. The expression analyses presented in this work already suggested several roles for *Slitl2* in the development and/or homeostasis of various mouse tissues with prominent expression (e.g., the skeletal system, the lung, and the kidney), part of which were indeed confirmed by the phenotypic description of *Slitl2*-deficient mice. Of note, *Slitl2* expression was also observed in the floor plate of the spinal cord, a structure involved in the guidance of axons, a well-characterized function of the eponymous Slit proteins.

Renal failure causes early death of *Slitl2*-deficient mice

For the second part of this study, *Slitl2*-deficient mice were generated via targeting of the *Slitl2* locus in murine embryonic stem (ES) cells. Subsequent deletion of the modified, *loxP*-flanked conditional gene was achieved both *in vitro* via transient expression of Cre recombinase in targeted ES cells and *in vivo* by crossing homozygous *Slitl2-floxed* mice with Cre recombinase-expressing transgenic mice. The two adopted approaches ultimately provoked the same phenotype in the derived *Slitl2*-deficient mice.

The detailed analysis of the mutant phenotype was conducted on offspring from matings of heterozygous *Slitl2-null* mice. These matings yielded homozygous *Slitl2*$^{-/-}$ pups at the expected Mendelian ratio, demonstrating that complete absence of *Slitl2* gene function does not cause embryonic lethality. However, while heterozygous *Slitl2*$^{+/-}$ mice were normal in size, viable, and fertile, homozygous null mutants failed to thrive to adulthood and succumbed to a progressive illness by the age of 3-4 weeks on average. The variations observed in the penetrance of the phenotype were possibly due to the mixed genetic background of the *Slitl2-null* mouse strain. Postmortem dissection revealed pale kidneys in moribund *Slitl2*-deficient mice, and histological examination confirmed multiple abnormalities. Severe glomerular lesions including ectatic capillaries, intracytoplasmic vacuoles, and atrophic capillary tufts were evident by light microscopy. Ultrastructural evaluation demonstrated the disruption of the glomerular filtration barrier with severe podocyte effacement within affected glomeruli, and SDS-PAGE urinaly-

sis as well as a sharply increased urinary albumin/creatinine ratio in moribund *Slitl2* null mutants confirmed massive proteinuria, a pathognomonic symptom for a defective glomerular filtration barrier. Due to excess protein leakage into the primary urine, hyaline droplet nephropathy of proximal tubular epithelial cells as well as widespread tubular protein deposits throughout the cortical and the medullary regions of the kidney were observed. Nephrotic syndrome in *Slitl2*-deficient mice after onset of wasting was further evidenced by severe hypalbuminemia. The decreased oncotic pressure caused severe subcutaneous edema, hydrothorax, and ascites. Moreover, uremia in the null mutants verified the kidney's inability to perform its physiological functions.

Expression analysis of *Slitl2-LacZ* knock-in mice revealed β-galactosidase activity in metanephric blastema cells already at the onset of nephrogenesis. Strong glomerular expression – mainly in podocytes – persisted throughout development and was also confirmed by immunohistochemical analysis of adult *Slitl2-Venus* transgenic kidneys. Collectively, these data indicated that the primary pathogenic lesions responsible for the early death of *Slitl2*-deficient mice occurred in the glomeruli.

The glomerulus is a highly specialized structure, and it is well known that not only proper development is essential for its function, but that it also requires maintenance throughout life in order to prevent serious disease conditions [Quaggin and Kreidberg, 2008]. For example, vascular endothelial growth factor A (VEGF-A), a major regulator of angiogenesis, is produced in large amounts in developing podocytes during fetal development, and its production continues in fully differentiated podocytes. As heterozygous and homozygous *Vegfa*-mutant mice die early during embryogenesis prior to the onset of kidney development, mice were generated with podocyte-specific alterations. While complete ablation of *Vegfa* gene function in these cells results in perinatal lethality with glomeruli devoid of endothelial cells, mice heterozygous for *Vegfa* in podocytes show a normal glomerular histology at birth and only develop end-stage renal failure characterized by necrotic endothelial cells and podocytes effacement by 9-12 weeks of age. These experiments not only demonstrated a dosage sensitivity for VEGF-A, but also emphasized its requirement for maintenance of glomerular integrity. Moreover, they confirmed the paradigm that a crosstalk between podocytes and endothelial cells in the mature glomerulus is essential for preservation of its function [Eremina et al., 2003].

It has not yet been elucidated whether the glomerular lesions in *Slitl2*-deficient

mice reflect developmental abnormalities that are not obvious but nevertheless induce pathological changes, or whether *Slitl2* regulates the expression of genes that are required to maintain a normal glomerular structure postnatally. While the early developmental expression of *Slitl2* argues in favor of the former theory, it is also conceivable to assume the latter. Molecular marker analysis suggested that the glomerular structure and composition in *Slitl2* null mutants is initially similar to that of wild-type glomeruli. All four major cells types, namely parietal epithelial cells, podocytes, mesangial cells, and endothelial cells were detected and displayed a regular arrangement in unaffected glomeruli. In support of this was the observation that the characteristic histological lesions and the associated pathophysiological effects were absent in newborn *Slitl2*-deficient mice. Thus, expression of *Slitl2* in podocytes might be essential to sustain glomerular integrity by interacting with glomerular endothelial cells, thereby preventing atrophy of the capillary tuft.

The essential role of podocytes in maintaining an intact glomerular filtration barrier has been demonstrated by a wide variety of studies involving genetic manipulations of podocyte-specific genes. Podocin, i.e., nephrosis 2 (*Neph2*) is a prominent representative, which is exclusively expressed in podocytes within the kidney [Roselli et al., 2002]. Similar to what was observed in *Slitl2*-deficient mice, podocin-deficient mice are indistinguishable from their wild-type littermates at birth, display postnatal growth retardation, and die within the first five weeks of life. In *Neph2*$^{-/-}$ mice, however, proteinuria is already present at birth. Kidney development appears grossly normal in these mice, but podocyte foot processes can only be detected occasionally already at embryonic day 16.5. Postnatally, the disease progresses rapidly, causing end-stage renal failure characterized by diffuse mesangial sclerosis (DMS) due to massive accumulation of extracellular matrix proteins [Roselli et al., 2004]. Interestingly, mutations of podocin in humans are associated with the development of focal and segmental glomerulosclerosis (FSGS), in which only a subpopulation of glomeruli exhibit segmental sclerotic lesions [Boute et al., 2000]. In humans, diffuse mesangial sclerosis is mainly seen in patients with mutations of another podocyte-specific gene, namely Wilms' tumor 1 (*WT1*) [Jeanpierre et al., 1998], which are related to diseases such as Denys-Drash syndrome and Frasier syndrome. The critical role of *Wt1* for the development of the kidney has been demonstrated in *Wt1*-deficient mice. Complete ablation of *Wt1* gene function causes embryonic lethality due to failure of kidney and gonad development [Kreidberg et al., 1993], while heterozyous *Wt1*$^{+/-}$

mice develop adult-onset mesangial sclerosis [Guo et al., 2002]. In order to elucidate the role of *Slitl2* in podocyte function, homozygous *Slitl2-floxed* mice will be crossed with transgenic mice expressing Cre recombinase under control of the human podocin (NPHS2) promoter (a kind gift from Dr. Marcus Möller, RWTH Aachen, Germany; [Moeller et al., 2003]). These matings will yield offspring with podocyte-specific excision of the conditional *Slitl2* gene. This strategy will clarify whether podocyte damage is the primary, eventually lethal defect in *Slitl2*-deficient mice.

Ikeda *et al.* have shown that the human homolog of *Slitl2*, vasorin (*VASN*), can bind TGF-β1 *in vitro* and attenuate its effect *in vivo* [Ikeda et al., 2004]. It is therefore reasonable to believe that *Slitl2* has similar functions in the mouse, even more so when considering the high sequence similarity of over 80% between the two homologous proteins. However, several observations argue against this theory. First, during embryonic development and in the adult mouse, *Tgfb1* is not expressed within glomeruli but only in the tubular system [Thompson et al., 1989] [Pelton et al., 1991]. Secondly, if one was to adopt the model suggested by Ikeda *et al.*, *Slitl2* would block TGF-β1 signaling at the extracellular and/or cell surface level. Consequently, *Slitl2*-deficiency in mice would lead to an increase in TGF-β1 downstream signaling. In transgenic mice expressing *Tgfb1* exclusively in the liver under control of the murine albumin (Alb) promoter, elevated serum levels of the transgene have been reported to cause glomerulosclerosis and interstitial fibrosis due to accumulation of extracellular matrix protein [Kopp et al., 1996]. Yet, such deposits were neither detected by periodic-acid Schiff (PAS) nor by Masson's trichrome staining in the kidneys of moribund *Slitl2* null mutants. Conversely, if *Slitl2* served as coreceptor for TGF-β1, thus transducing its signal, ablation of *Slitl2* gene function would reduce or even abolish TGF-β1 activity in the affected cell types. *Tgfb1*-deficient mice die approximately three weeks after birth due to massive inflammation of multiple organs, including the kidney [Shull et al., 1992]. Prior to inflammatory cell infiltration, expression of major histocompatibility complex (MHC) class I and class II molecules is elevated in *Tgfb1* null mutants [Geiser et al., 1993]. cDNA microarray analysis indeed revealed a significant upregulation of MHC class II molecules in *Slitl2*-deficient kidneys, but inflammatory infiltrates were never detected in the organs of moribund *Slitl2* mutants. The absence of such infiltrates was to be expected with regard to the results from the blood count and flow cytometric analysis, which demonstrated a strongly reduced total number of leukocytes with predominant depletion of

lymphocytes in the *Slitl2* mutants. At the same time, this observation made an inflammatory process as fatal event – as seen in the *Tgfb1*-deficient mice – rather unlikely. Presumably, an underlying primary pathogenic mechanism triggered an inflammatory response, thereby inducing the expression of several chemokines, which, in turn, induced the expression of MHC class II molecules in the *Slitl2*-deficient kidneys (see page 152). Cytokine-mediated upregulation of MHC class II expression has, in fact, been reported previously for glomerular mesangial cells and renal tubular epithelial cells [Martin et al., 1989] [Banu et al., 2002]. It has to be taken into account in this context that whole tissue samples rather than microdissected glomeruli were used for the isolation of RNA for the microarray experiment. Thus, if the primary pathogenic lesions do occur in the glomeruli, the genetic alterations directly linked to the inactivation of *Slitl2* might be masked by those provoked by the inflammatory response mechanisms. Nonetheless, the results derived from the microarray analysis were verified by the detected high degree of *Slitl2* downregulation in the mutant kidneys.

Interestingly, the gene showing the highest degree of upregulation in *Slitl2*-deficient kidneys, namely *Havcr1* (hepatitis A virus cellular receptor 1), is also known as kidney injury molecule 1 (*Kim1*). It has been reported that this type 1 membrane protein is upregulated in proliferating and dedifferentiated tubular cells after renal ischemia [Kuehn et al., 2002]. This condition was reflected by the pale appearance of the *Slitl2*-deficient kidneys at dissection. Moreover, expression of *Timp1* (tissue inhibitor of metalloproteinase 1) was found to be upregulated. Overexpression of this gene has previously been linked to renal hypoxic conditions [Norman et al., 1999]. Based on the observation that *Slitl2* shows strong expression in vascular smooth muscle cells (VSMCs), it is tempting to speculate that a decreased perfusion rate is responsible for initiating the renal damages. Ikeda *et al.* have shown that neointimal formation after vascular injury was accompanied by decreased levels of vasorin expression [Ikeda et al., 2004]. Therefore, ablation of *Slitl2* gene function might induce phenotypic modulation of quiescent VSMCs, and, as a result, induce excess neointimal formation, thereby causing tissue hypoxia via obliteration of the renal microvasculature.

The bone phenotype could be primary or secondary

Growth retardation is another prominent feature of *Slitl2*-deficient mice. It was evident as early as two weeks after birth and became increasingly more pronounced until the time of death of the mutants. The overall anatomy of *Slitl2*-deficient skeletons seemed unaltered, but micro-computed tomography (μCT) scans of long bones from *Slitl2* null mutants and age- and gender-matched control mice revealed abnormalities of the bone structure. Reduced cortical as well as trabecular bone indicated that inactivation of *Slitl2* gene function has a major effect on normal bone architecture.

An impaired bone metabolism is a common side effect of renal insufficiency as was, for example, also observed in mice lacking the transcription factor AP-2β [Moser et al., 2003]. Indeed, numerous data suggest that the skeletal abnormalities of *Slitl2*-mutant mice are caused by kidney failure. First of all, the serum calcium level is usually maintained within a very narrow range to ensure normal neuromuscular conduction and metabolic functions. Serum calcium levels in *Slitl2*-deficient mice, however, were markedly decreased in comparison to wild-type control animals, hinting at an imbalanced hormonal control mechanism. Vitamin D, which is responsible for calcium absorption in the small intestine, is converted to its bioactive form, 1,25-dihydroxycholecalciferol, in the kidney by the enzyme 1-α-hydroxylase. Impaired renal function entails reduced enzyme activity, leading to decreased activation of vitamin D. Evaluation of serum vitamin D levels revealed a strong reduction of its active form in *Slitl2*-deficient mice, which is consistent with renal insufficiency in these animals. Inadequate activation of vitamin D was also reflected by decreased urinary calcium levels in *Slitl2*-deficient mice, demonstrating that the reduced serum calcium levels were not induced by excess urinary excretion but rather by insufficient intestinal absorption.

Besides vitamin D, the hormonal control loop also involves parathormone (PTH), which is produced by the parathyroid glands. It is, in fact, the most important hormone in controlling calcium homeostasis in the blood. Its release is triggered by lowered serum calcium levels and it exerts multiple functions to revert blood calcium levels back to normal. It stimulates calcium release from the bones via osteoclast activation, it enhances calcium reabsorption in the kidney, and indirectly increases its absorption by intestinal mucosal cells via stimulation of vitamin D activation. Even though serum PTH levels could not yet be measured in *Slitl2* null mutants due to technical restraints, amphiregulin (*Areg*) was found to be upregulated in *Slitl2*-mutant kidneys. The expression of this gene is known

to be induced by high levels of PTH [Qin et al., 2005]. It is therefore easily conceivable that excess levels of PTH are released in the *Slitl2* null mutants in order to restore a normal blood calcium concentration, a condition known as secondary hyperparathyroidism.

However, the marked expression of *Slitl2* in the murine skeletal system suggests not only a prominent role during embryonic development and adult bone homeostasis, but also a direct involvement of *Slitl2*-deficiency in the observed defects independent of any other detrimental effect. For instance, bone morphogenetic proteins (BMPs) of the TGF-β superfamily are also expressed in the developing skeletal system [Ducy and Karsenty, 2000], and homozygous deletion of *Bmp3*, for example, results in bone defects. While *Bmp3*-deficient mouse embryos and newborns do not yet reveal any abnormalities, femurs collected from 5-week-old mutants display an increased trabecular bone density [Daluiski et al., 2001].

The absence of *Slitl2* gene function could directly interfere with a balanced osteoblast and/or osteoclast activity. Recent findings support this assumption. P1NP (procollagen type I amino-terminal propeptide), a marker for osteoblast activity, and TRAP (tartrate-resistant acid phosphatase), a marker for osteoclast activity, were both found to be highly downregulated in the serum of *Slitl2*-deficient mice in comparison to wild-type control animals (Dr. Marco Eijken, Erasmus Medical Center, Rotterdam, The Netherlands; personal communication). This is in contrast to renal insufficiency associated with high levels of PTH, which usually leads to high bone turnover with increased expression of both markers [Fukagawa et al., 2002], and therefore argues against a secondary bone phenotype in *Slitl2*-deficient mice.

Postnatal growth retardation has also been reported for *Tgfb1*-deficient mice [Kulkarni et al., 1995]. Histomorphometric analyses on long bones of ~3.5-week-old *Tgfb1*$^{-/-}$ mice revealed a significant reduction of both the growth plate width and the longitudinal growth rate in comparison to heterozygous and wild-type controls [Geiser et al., 1998]. It has been shown that active TGF-β1 is released during bone resorption and induces the migration of bone mesenchymal stem cells (BMSCs) *in vitro*. This process was demonstrated to be mediated by the Smad downstream signaling pathway. In order to determine the role of TGF-β1-induced BMSC migration during bone remodeling in the adult mouse *in vivo*, *Tgfb1*$^{-/-}$ mice were crossed with immunodeficient *Rag2*$^{-/-}$ mice to prevent early death of the *Tgfb1* mutants due to autoimmune disease. 3-month-old double-deficient mice exhibited a significant loss of trabecular bone volume and thickness with

significantly less osteoblasts dispersed on the bone surface. Collectively, these observations indicated a role for TGF-β1 in coupling bone resorption with bone formation in the adult mouse [Tang et al., 2009]. With regard to the findings obtained from the μCT analysis of *Slitl2*-deficient bones and a potential involvement of *Slitl2* in TGF-β signaling, these results further suggest a direct role for *Slitl2* in bone development and/or homeostasis.

The spleen and thymus phenotype is secondary

The most striking finding at necropsy of all moribund *Slitl2*-deficient mice was the dramatic atrophy of two major lymphoid organs, namely the spleen and the thymus. Histological analysis revealed a marked disruption of the physiological tissue organization, and flow cytometric analysis further substantiated this observation. Flow cytometry showed a sharp reduction in the total cell number of the affected organs with a predominant depletion of both the B and T cell precursor pool. The depletion of lymphocytes can be induced by high serum levels of corticosterone and is known to be a common finding in severely stressed or terminally ill mice [Barone et al., 1993] [Laakko and Fraker, 2002]. Therefore, serum corticosterone levels were measured in moribund *Slitl2* null mutants and were found to be elevated more than 25-fold in comparison to that of wild-type littermates. The marked overall difference in global gene expression compared to wild-type controls could be explained in this context with regard to an almost complete absence of certain cell subpopulations in the respective tissues of *Slitl2*-deficient animals. This loss of actively dividing cells was additionally reflected by the terms derived from the functional annotation clustering analysis (see page 146 onwards). The detected degree of *Slitl2* downregulation in the spleen and especially in the thymus was extremely moderate compared to that of *Slitl2*-deficient kidneys, arguing for a more indirect involvement of *Slitl2*-deficiency in the genesis of these alterations. This assumption was further corroborated by the fact that the abnormalities in thymic and splenic tissue organization were not observed prior to the onset of overt illness in *Slitl2* null mutants. Conclusively, the collected data suggested that the thymic and splenic atrophy in moribund *Slitl2*-deficient mice can be attributed to the sharp increase of the stress-related hormone corticosterone and consequently be considered a secondary phenotype.

Interestingly, the atrophy of spleen and thymus was also observed in mice deficient for latent transforming growth factor binding protein 3 (Ltbp3), a protein associated with TGF-β signaling. These defects were also shown to be caused by

elevated serum levels of corticosterone and could be reversed by administration of aminoglutethimide (AMG), an inhibitor of steroid synthesis. This treatment, however, did not avert death of an as yet unidentified cause in the severely affected *Ltbp3*-deficient mice, which succumb at an age similar to that of the *Slitl2* null mutants [Chen et al., 2003]. Administration of this drug could therefore further clarify whether elevated corticosterone levels are indeed responsible for the splenic and thymic atrophy in *Slitl2*-deficient mice.

Conclusion

The data presented in this thesis demonstrate that *Slitl2*-deficiency in mice causes early death due to renal failure. Future studies will have to analyze the exact nature of the glomerular lesions. Conditional *Slitl2* mice will be crossed with NPHS2-Cre mice for podocyte-specific deletion of the gene. Previous attempts to colocalize reporter protein in the kidneys of transgenic *Slitl2-Venus* mice with glomerular marker proteins will be repeated. Future experiments will have to decipher whether the bone phenotype in *Slitl2*-deficient mice is a primary defect or whether it is secondary due to kidney insufficiency. Therefore, rescue experiments will be conducted by replacement therapy with vitamin D or by feeding a high calcium diet [Dardenne et al., 2004]. Furthermore, Venus-expressing cells will be isolated from *Slitl2-Venus* mice on a *Slitl2*-mutant and wild-type background for subsequent *in vitro* functional analyses in order to elucidate the affected signaling pathway in *Slitl2*-deficient mice.

5 Summary

The murine Slit-like 2 (*Slitl2*) gene was first identified in 2002, and so far, no reports have been published on it. This thesis aimed at answering two basic questions when first analyzing the function of a gene: a) Where is the gene expressed? and b) What happens if the gene function is abolished?

A comprehensive temporospatial expression pattern was provided by describing not only endogenous *Slitl2* expression, but also reporter gene expression in *Slitl2-LacZ* knock-in and in *Slitl2-Venus* transgenic mice. All three approaches rendered consistent results and revealed widespread expression from early developmental stages onwards. Prominent expression was observed in the developing as well as the adult skeletal system. Likewise, vascular smooth muscle cells and glomeruli exhibited strong expression throughout all stages of development. Moderate expression was, for example, seen in the adult lung epithelium and pancreatic islets of Langerhans. Collectively, the findings from the expression analysis indicated important roles for *Slitl2* in the mouse.

Non-redundant functions of *Slitl2* could indeed be demonstrated by the generation of *Slitl2*-deficient mice via classical gene targeting in embryonic stem cells. *Slitl2*-mutant mice are phenotypically indistinguishable from their wild-type littermates at birth but develop a progressive illness and succumb to renal failure by 3-4 weeks of age. Prenatal kidney development appears unimpaired, and defects only emerge after birth. Renal insufficiency in these mice is characterized by severe glomerular lesions with massive podocyte effacement, capillary ectasia or even complete atrophy of the capillary tufts. *Slitl2*-deficient mice develop nephrotic syndrome with massive proteinuria and severe hypalbuminemia, which ultimately causes hyaline droplet nephropathy as well as subcutaneous edema, hydrothorax, and ascites. In addition, moribund null mutants are uremic, which further reflects renal failure in these animals.

Despite the fact that kidney failure inevitably entails a perturbed bone metabolism, the decreased bone density in conjunction with a low bone turnover in *Slitl2*-deficient mice could also be a direct cause of the gene inactivation with regard to the distinct expression of *Slitl2* in the skeletal system already at embryonic stages. The marked splenic and thymic atrophy in moribund *Slitl2*-deficient mice,

on the other hand, could be attributed to increased serum levels of corticosterone and are therefore considered to be secondary effects.

This thesis has laid the groundwork for future studies which will have to address the exact mechanism of the glomerular defects of the *Slitl2* mutants and elucidate the underlying signaling pathway. With millions of people affected with kidney disease, this mouse model may serve as a valuable tool for *in vivo* studies and for testing potential therapeutic modalities.

6 Zusammenfassung

Analyse des Expressionsmusters und Knock-out Phänotyps des Gens Slit-like 2 (*Slitl2*) in der Maus

Das Gen Slit-like 2 (*Slitl2*) der Maus wurde erstmals im Jahr 2002 identifiziert. Bis dato gibt es noch keine Veröffentlichungen diesbezüglich. Mit der vorliegenden Arbeit sollten zwei grundlegende Fragen geklärt werden, die im Zusammenhang mit einem neu identifizierten Gen auftreten: a) Wo ist das Gen exprimiert? und b) Was passiert, wenn das Gen ausgeschaltet wird?

Die Analyse des Expressionsmusters erfolgte anhand der Beschreibung sowohl der endogenen *Slitl2* Expression, als auch der Reportergenexpression in *Slitl2-LacZ* knock-in und *Slitl2-Venus*-transgenen Mäusen. Alle drei Herangehensweisen lieferten übereinstimmende Ergebnisse und zeigten verbreitete *Slitl2*-Expression bereits in frühen Phasen der Embryonalentwicklung. Besonders ausgeprägte Expression wurde sowohl im sich entwickelnden wie auch im erwachsenen Skelett beobachtet. Gleichermaßen zeigten glatte Gefäßmuskelzellen sowie Glomeruli starke Expression in allen Stadien der Entwicklung. Mäßige Expression wurde u.a. in den Lungenepithelzellen und den Langerhansschen Inselzellen des Pankreas der adulten Maus festgestellt. Insgesamt ließen die Ergebnisse der Expressionsanalyse bereits eine wichtige Rolle für das Gen in der Maus vermuten.

Essentielle Funktionen des Gens *Slitl2* konnten durch die Erzeugung *Slitl2*-defizienter Mäuse mit Hilfe der Inaktivierung des Gens in embryonalen Stammzellen nachgewiesen werden. Anfänglich sind die Mausmutanten nicht von ihren Wildtyp-Wurfgeschwistern zu unterscheiden, erkranken aber zunehmend und sterben schließlich an Nierenversagen im Alter von 3-4 Wochen. Die pränatale Nierenentwicklung scheint nicht beeinträchtig zu sein, treten doch die Schädigungen erst nachgeburtlich auf. Die Niereninsuffizienz dieser Tiere wird durch schwere Läsionen der Glomeruli ausgelöst, welche durch Verschmelzung der Podozyten-Fußfortsätze und Kapillarektasie bis hin zur Atrophie des Kapillarknäuels gekennzeichnet sind. *Slitl2*-defiziente Mäuse entwickeln ein nephrotisches Syndrom mit

massiver Proteinurie und hochgradiger Hypalbuminämie. Eine hyalintropfige Speicherungsnephrose sowie subkutane Ödeme, Hydrothorax und Ascites sind die Folge. Das Nierenversagen zeigt sich zudem in Form einer ausgeprägten Urämie.

Niereninsuffizienz zieht unausweichlich eine Beeinträchtigung des Knochenstoffwechsels nach sich. Dennoch könnte es sich bei der reduzierten Knochendichte der *Slitl2*-defizienten Tieren, die mit einem reduzierten Knochenumsatz vergesellschaftet ist, auch um eine direkte Auswirkung der Geninaktivierung handeln, berücksichtigt man die starke Expression von *Slitl2* in den Knochen schon ab embryonalen Phasen der Entwicklung. Im Gegensatz dazu stellen die ausgeprägte Atrophie von Milz und Thymus bei moribunden *Slitl2*-defizienten Mäusen möglicherweise einen Sekundäreffekt dar, ausgelöst durch erhöhte Corticosteronwerte im Serum.

Diese Arbeit hat die Grundlagen für zukünftige Untersuchungen geschaffen, die sich mit dem genauen Mechanismus der glomerulären Läsionen befassen und den zugrunde liegenden Signaltransduktionsweg identifizieren sollten. Weltweit sind Millionen von Menschen von Nierenerkrankungen betroffen. *Slitl2*-defiziente Mäuse könnten somit als wertvolles Tiermodell für *in vivo*-Studien und zur Erforschung neuer Therapieansätze dienen.

References

Abbondanzo, S. J., Gadi, I., and Stewart, C. L. (1993). Derivation of embryonic stem cell lines. *Methods Enzymol*, *225*, 803–823.

Anselmo, M. A., Dalvin, S., Prodhan, P., Komatsuzaki, K., Aidlen, J. T., Schnitzer, J. J., Wu, J. Y., and Kinane, T. B. (2003). Slit and robo: expression patterns in lung development. *Gene Expr Patterns*, *3*(1), 13–19.

Bagri, A., Marin, O., Plump, A. S., Mak, J., Pleasure, S. J., Rubenstein, J. L. R., and Tessier-Lavigne, M. (2002). Slit proteins prevent midline crossing and determine the dorsoventral position of major axonal pathways in the mammalian forebrain. *Neuron*, *33*(2), 233–248.

Banu, N., Mozes, M. M., Kopp, J. B., Ziyadeh, F. N., and Meyers, C. M. (2002). Regulation of inducible class II MHC, costimulatory molecules, and cytokine expression in TGF-beta1 knockout renal epithelial cells: effect of exogenous TGF-beta1. *Exp Nephrol*, *10*(5-6), 320–331.

Barone, K. S., O'Brien, P. C., and Stevenson, J. R. (1993). Characterization and mechanisms of thymic atrophy in protein-malnourished mice: role of corticosterone. *Cell Immunol*, *148*(1), 226–233.

Benjamini, Y., and Hochberg, Y. (1995). Controlling the False Discovery Rate: A Practical and Powerful Approach to Multiple Testing. *Journal of the Royal Statistical Society. Series B (Methodological)*, *57*(1), 289–300.

Boivin, G. P., O'Toole, B. A., Orsmby, I. E., Diebold, R. J., Eis, M. J., Doetschman, T., and Kier, A. B. (1995). Onset and progression of pathological lesions in transforming growth factor-beta 1-deficient mice. *Am J Pathol*, *146*(1), 276–288.

Boute, N., Gribouval, O., Roselli, S., Benessy, F., Lee, H., Fuchshuber, A., Dahan, K., Gubler, M. C., Niaudet, P., and Antignac, C. (2000). NPHS2, encoding the glomerular protein podocin, is mutated in autosomal recessive steroid-resistant nephrotic syndrome. *Nat Genet*, *24*(4), 349–354.

Brose, K., Bland, K. S., Wang, K. H., Arnott, D., Henzel, W., Goodman, C. S., Tessier-Lavigne, M., and Kidd, T. (1999). Slit proteins bind Robo receptors and have an evolutionarily conserved role in repulsive axon guidance. *Cell*, *96*(6), 795–806.

Burdsal, C. A., Damsky, C. H., and Pedersen, R. A. (1993). The role of E-cadherin and integrins in mesoderm differentiation and migration at the mammalian primitive streak. *Development*, *118*(3), 829–844.

Chen, L., Yao, J.-h., Zhang, S.-h., Wang, L., Song, H.-d., and Xue, J.-l. (2005). Slit-like 2, a novel zebrafish slit homologue that might involve in zebrafish central neural and vascular morphogenesis. *Biochem Biophys Res Commun*, *336*(1), 364–371.

Chen, Y., Dabovic, B., Colarossi, C., Santori, F. R., Lilic, M., Vukmanovic, S., and Rifkin, D. B. (2003). Growth retardation as well as spleen and thymus involution in latent TGF-beta binding protein (Ltbp)-3 null mice. *J Cell Physiol*, *196*(2), 319–325.

Christ, M., McCartney-Francis, N. L., Kulkarni, A. B., Ward, J. M., Mizel, D. E., Mackall, C. L., Gress, R. E., Hines, K. L., Tian, H., and Karlsson, S. (1994). Immune dysregulation in TGF-beta 1-deficient mice. *J Immunol*, *153*(5), 1936–1946.

Copeland, N. G., Jenkins, N. A., and Court, D. L. (2001). Recombineering: a powerful new tool for mouse functional genomics. *Nat Rev Genet*, *2*(10), 769–779.

Dallol, A., Da Silva, N. F., Viacava, P., Minna, J. D., Bieche, I., Maher, E. R., and Latif, F. (2002). SLIT2, a human homologue of the Drosophila Slit2 gene, has tumor suppressor activity and is frequently inactivated in lung and breast cancers. *Cancer Res*, *62*(20), 5874–5880.

Dallol, A., Morton, D., Maher, E. R., and Latif, F. (2003). SLIT2 axon guidance molecule is frequently inactivated in colorectal cancer and suppresses growth of colorectal carcinoma cells. *Cancer Res*, *63*(5), 1054–1058.

Daluiski, A., Engstrand, T., Bahamonde, M. E., Gamer, L. W., Agius, E., Stevenson, S. L., Cox, K., Rosen, V., and Lyons, K. M. (2001). Bone morphogenetic protein-3 is a negative regulator of bone density. *Nat Genet*, *27*(1), 84–88.

Dardenne, O., Prud'homme, J., Glorieux, F. H., and St-Arnaud, R. (2004). Rescue of the phenotype of CYP27B1 (1alpha-hydroxylase)-deficient mice. *J Steroid Biochem Mol Biol*, *89-90*(1-5), 327–330.

Datto, M. B., Frederick, J. P., Pan, L., Borton, A. J., Zhuang, Y., and Wang, X. F. (1999). Targeted disruption of Smad3 reveals an essential role in transforming growth factor beta-mediated signal transduction. *Mol Cell Biol*, *19*(4), 2495–2504.

Datto, M. B., Li, Y., Panus, J. F., Howe, D. J., Xiong, Y., and Wang, X. F. (1995). Transforming growth factor beta induces the cyclin-dependent kinase inhibitor p21 through a p53-independent mechanism. *Proc Natl Acad Sci U S A*, *92*(12), 5545–5549.

Davies, J. A., and Bard, J. B. (1996). Inductive interactions between the mesenchyme and the ureteric bud. *Exp Nephrol*, *4*(2), 77–85.

Dickson, M. C., Martin, J. S., Cousins, F. M., Kulkarni, A. B., Karlsson, S., and Akhurst, R. J. (1995). Defective haematopoiesis and vasculogenesis in transforming growth factor-beta 1 knock out mice. *Development*, *121*(6), 1845–1854.

Dkhissi, F., Raynal, S., Jullien, P., and Lawrence, D. A. (1999). Growth stimulation of murine fibroblasts by TGF-beta1 depends on the expression of a functional p53 protein. *Oncogene*, *18*(3), 703–711.

Ducy, P., and Karsenty, G. (2000). The family of bone morphogenetic proteins. *Kidney Int*, *57*(6), 2207–2214.

Eremina, V., Sood, M., Haigh, J., Nagy, A., Lajoie, G., Ferrara, N., Gerber, H.-P., Kikkawa, Y., Miner, J. H., and Quaggin, S. E. (2003). Glomerular-specific alterations of VEGF-A expression lead to distinct congenital and acquired renal diseases. *J Clin Invest*, *111*(5), 707–716.

Erskine, L., Williams, S. E., Brose, K., Kidd, T., Rachel, R. A., Goodman, C. S., Tessier-Lavigne, M., and Mason, C. A. (2000). Retinal ganglion cell axon guidance in the mouse optic chiasm: expression and function of robos and slits. *J Neurosci*, *20*(13), 4975–4982.

Fourney, R. M., Miyakoshi, J., Day III, R. S., and Paterson, M. C. (1988). Northern Blotting: Efficient RNA Staining and Transfer. *Bethesda Res Lab Focus*, *10*, 5–6.

Fowlis, D. J., Cui, W., Johnson, S. A., Balmain, A., and Akhurst, R. J. (1996). Altered epidermal cell growth control in vivo by inducible expression of transforming growth factor beta 1 in the skin of transgenic mice. *Cell Growth Differ*, *7*(5), 679–687.

Fukagawa, M., Kazama, J. J., and Kurokawa, K. (2002). Renal osteodystrophy and secondary hyperparathyroidism. *Nephrol Dial Transplant*, *17 Suppl 10*, 2–5.

Galbreath, E., Kim, S. J., Park, K., Brenner, M., and Messing, A. (1995). Overexpression of TGF-beta 1 in the central nervous system of transgenic mice results in hydrocephalus. *J Neuropathol Exp Neurol*, *54*(3), 339–349.

Geiser, A. G., Letterio, J. J., Kulkarni, A. B., Karlsson, S., Roberts, A. B., and Sporn, M. B. (1993). Transforming growth factor beta 1 (TGF-beta 1) controls expression of major histocompatibility genes in the postnatal mouse: aberrant histocompatibility antigen expression in the pathogenesis of the TGF-beta 1 null mouse phenotype. *Proc Natl Acad Sci U S A*, *90*(21), 9944–9948.

Geiser, A. G., Zeng, Q. Q., Sato, M., Helvering, L. M., Hirano, T., and Turner, C. H. (1998). Decreased bone mass and bone elasticity in mice lacking the transforming growth factor-beta1 gene. *Bone*, *23*(2), 87–93.

George, J., Roulot, D., Koteliansky, V. E., and Bissell, D. M. (1999). In vivo inhibition of rat stellate cell activation by soluble transforming growth factor beta type II receptor: a potential new therapy for hepatic fibrosis. *Proc Natl Acad Sci U S A*, *96*(22), 12719–12724.

George, S. H. L., Gertsenstein, M., Vintersten, K., Korets-Smith, E., Murphy, J., Stevens, M. E., Haigh, J. J., and Nagy, A. (2007). Developmental and adult phenotyping directly from mutant embryonic stem cells. *Proc Natl Acad Sci U S A*, *104*(11), 4455–4460.

Gilbert, S. F. (2006). *Developmental biology* (8th ed.). Sunderland, Mass.: Sinauer Associates, Inc. Publishers.

Gorelik, L., and Flavell, R. A. (2001). Immune-mediated eradication of tumors through the blockade of transforming growth factor-beta signaling in T cells. *Nat Med*, *7*(10), 1118–1122.

Greenberg, J. M., Thompson, F. Y., Brooks, S. K., Shannon, J. M., and Akeson, A. L. (2004). Slit and robo expression in the developing mouse lung. *Dev Dyn*, *230*(2), 350–360.

Grieshammer, U., Plump, A. S., Wang, F., Tessier-Lavigne, M., and Martin, G. R. (2004). SLIT2-mediated ROBO2 signaling restricts kidney induction to a single site. *Dev Cell*, *6*(5), 709–717.

Guo, J.-K., Menke, A. L., Gubler, M.-C., Clarke, A. R., Harrison, D., Hammes, A., Hastie, N. D., and Schedl, A. (2002). WT1 is a key regulator of podocyte function: reduced expression levels cause crescentic glomerulonephritis and mesangial sclerosis. *Hum Mol Genet*, *11*(6), 651–659.

Hedrich, H. J., and Bullock, G. R. (2004). *The Laboratory Mouse (Handbook of Experimental Animals)* (1st ed.). Amsterdam: Elsevier Academic Press.

Hellmich, H. L., Kos, L., Cho, E. S., Mahon, K. A., and Zimmer, A. (1996). Embryonic expression of glial cell-line derived neurotrophic factor (GDNF) suggests multiple developmental roles in neural differentiation and epithelial-mesenchymal interactions. *Mech Dev*, *54*(1), 95–105.

Holmes, G. P., Negus, K., Burridge, L., Raman, S., Algar, E., Yamada, T., and Little, M. H. (1998). Distinct but overlapping expression patterns of two vertebrate slit homologs implies functional roles in CNS development and organogenesis. *Mech Dev*, *79*(1-2), 57–72.

Ikeda, Y., Imai, Y., Kumagai, H., Nosaka, T., Morikawa, Y., Hisaoka, T., Manabe, I., Maemura, K., Nakaoka, T., Imamura, T., Miyazono, K., Komuro, I.,

Nagai, R., and Kitamura, T. (2004). Vasorin, a transforming growth factor beta-binding protein expressed in vascular smooth muscle cells, modulates the arterial response to injury in vivo. *Proc Natl Acad Sci U S A*, *101*(29), 10732–10737.

Itoh, A., Miyabayashi, T., Ohno, M., and Sakano, S. (1998). Cloning and expressions of three mammalian homologues of Drosophila slit suggest possible roles for Slit in the formation and maintenance of the nervous system. *Brain Res Mol Brain Res*, *62*(2), 175–186.

Janda, E., Lehmann, K., Killisch, I., Jechlinger, M., Herzig, M., Downward, J., Beug, H., and Grunert, S. (2002). Ras and TGFβ cooperatively regulate epithelial cell plasticity and metastasis: dissection of Ras signaling pathways. *J Cell Biol*, *156*(2), 299–313.

Jeanpierre, C., Denamur, E., Henry, I., Cabanis, M. O., Luce, S., Cecille, A., Elion, J., Peuchmaur, M., Loirat, C., Niaudet, P., Gubler, M. C., and Junien, C. (1998). Identification of constitutional WT1 mutations, in patients with isolated diffuse mesangial sclerosis, and analysis of genotype/phenotype correlations by use of a computerized mutation database. *Am J Hum Genet*, *62*(4), 824–833.

Kessel, M., Balling, R., and Gruss, P. (1990). Variations of cervical vertebrae after expression of a Hox-1.1 transgene in mice. *Cell*, *61*(2), 301–308.

Kidd, T., Bland, K. S., and Goodman, C. S. (1999). Slit is the midline repellent for the robo receptor in Drosophila. *Cell*, *96*(6), 785–794.

Kim, H. K., Zhang, H., Li, H., Wu, T.-T., Swisher, S., He, D., Wu, L., Xu, J., Elmets, C. A., Athar, M., Xu, X.-c., and Xu, H. (2008). Slit2 inhibits growth and metastasis of fibrosarcoma and squamous cell carcinoma. *Neoplasia*, *10*(12), 1411–1420.

Kopp, J. B., Factor, V. M., Mozes, M., Nagy, P., Sanderson, N., Bottinger, E. P., Klotman, P. E., and Thorgeirsson, S. S. (1996). Transgenic mice with increased plasma levels of TGF-beta 1 develop progressive renal disease. *Lab Invest*, *74*(6), 991–1003.

Kramer, S. G., Kidd, T., Simpson, J. H., and Goodman, C. S. (2001). Switching repulsion to attraction: changing responses to slit during transition in mesoderm migration. *Science*, *292*(5517), 737–740.

Kreidberg, J. A., Sariola, H., Loring, J. M., Maeda, M., Pelletier, J., Housman, D., and Jaenisch, R. (1993). WT-1 is required for early kidney development. *Cell*, *74*(4), 679–691.

Kuehn, E. W., Park, K. M., Somlo, S., and Bonventre, J. V. (2002). Kidney injury molecule-1 expression in murine polycystic kidney disease. *Am J Physiol Renal Physiol*, *283*(6), F1326–36.

Kuhn, C., and McDonald, J. A. (1991). The roles of the myofibroblast in idiopathic pulmonary fibrosis. Ultrastructural and immunohistochemical features of sites of active extracellular matrix synthesis. *Am J Pathol*, *138*(5), 1257–1265.

Kulkarni, A. B., Huh, C. G., Becker, D., Geiser, A., Lyght, M., Flanders, K. C., Roberts, A. B., Sporn, M. B., Ward, J. M., and Karlsson, S. (1993). Transforming growth factor beta 1 null mutation in mice causes excessive inflammatory response and early death. *Proc Natl Acad Sci U S A*, *90*(2), 770–774.

Kulkarni, A. B., Ward, J. M., Yaswen, L., Mackall, C. L., Bauer, S. R., Huh, C. G., Gress, R. E., and Karlsson, S. (1995). Transforming growth factor-beta 1 null mice. An animal model for inflammatory disorders. *Am J Pathol*, *146*(1), 264–275.

Laakko, T., and Fraker, P. (2002). Rapid changes in the lymphopoietic and granulopoietic compartments of the marrow caused by stress levels of corticosterone. *Immunology*, *105*(1), 111–119.

Laird, P. W., Zijderveld, A., Linders, K., Rudnicki, M. A., Jaenisch, R., and Berns, A. (1991). Simplified mammalian DNA isolation procedure. *Nucleic Acids Res*, *19*(15), 4293.

Lee, C. G., Homer, R. J., Zhu, Z., Lanone, S., Wang, X., Koteliansky, V., Shipley, J. M., Gotwals, P., Noble, P., Chen, Q., Senior, R. M., and Elias, J. A. (2001). Interleukin-13 induces tissue fibrosis by selectively stimulating and activating transforming growth factor beta(1). *J Exp Med*, *194*(6), 809–821.

Letterio, J. J., Geiser, A. G., Kulkarni, A. B., Dang, H., Kong, L., Nakabayashi, T., Mackall, C. L., Gress, R. E., and Roberts, A. B. (1996). Autoimmunity associated with TGF-beta1-deficiency in mice is dependent on MHC class II antigen expression. *J Clin Invest*, *98*(9), 2109–2119.

Liu, J., Zhang, L., Wang, D., Shen, H., Jiang, M., Mei, P., Hayden, P. S., Sedor, J. R., and Hu, H. (2003). Congenital diaphragmatic hernia, kidney agenesis and cardiac defects associated with Slit3-deficiency in mice. *Mech Dev*, *120*(9), 1059–1070.

Liu, P., Jenkins, N. A., and Copeland, N. G. (2003). A highly efficient recombineering-based method for generating conditional knockout mutations. *Genome Res*, *13*(3), 476–484.

Long, H., Sabatier, C., Ma, L., Plump, A., Yuan, W., Ornitz, D. M., Tamada, A., Murakami, F., Goodman, C. S., and Tessier-Lavigne, M. (2004). Conserved roles for Slit and Robo proteins in midline commissural axon guidance. *Neuron*, *42*(2), 213–223.

Mambetisaeva, E. T., Andrews, W., Camurri, L., Annan, A., and Sundaresan, V. (2005). Robo family of proteins exhibit differential expression in mouse spinal

cord and Robo-Slit interaction is required for midline crossing in vertebrate spinal cord. *Dev Dyn*, *233*(1), 41–51.

Martin, M., Schwinzer, R., Schellekens, H., and Resch, K. (1989). Glomerular mesangial cells in local inflammation. Induction of the expression of MHC class II antigens by IFN-gamma. *J Immunol*, *142*(6), 1887–1894.

Massague, J., and Gomis, R. R. (2006). The logic of TGFbeta signaling. *FEBS Lett*, *580*(12), 2811–2820.

McCormick, L. L., Zhang, Y., Tootell, E., and Gilliam, A. C. (1999). Anti-TGF-beta treatment prevents skin and lung fibrosis in murine scleroderma-tous graft-versus-host disease: a model for human scleroderma. *J Immunol*, *163*(10), 5693–5699.

Meyers, E. N., Lewandoski, M., and Martin, G. R. (1998). An Fgf8 mutant allelic series generated by Cre- and Flp-mediated recombination. *Nat Genet*, *18*(2), 136–141.

Moeller, M. J., Sanden, S. K., Soofi, A., Wiggins, R. C., and Holzman, L. B. (2003). Podocyte-specific expression of cre recombinase in transgenic mice. *Genesis*, *35*(1), 39–42.

Moser, M., Dahmen, S., Kluge, R., Grone, H., Dahmen, J., Kunz, D., Schorle, H., and Buettner, R. (2003). Terminal renal failure in mice lacking transcription factor AP-2 beta. *Lab Invest*, *83*(4), 571–578.

Moses, H. L., Yang, E. Y., and Pietenpol, J. A. (1991). Regulation of epithelial proliferation by TGF-beta. *Ciba Found Symp*, *157*, 66–74.

Nagy, A. (2003). *Manipulating the Mouse Embryo - A Laboratory Manual* (3rd ed.). Cold Spring Harbor, N.Y.: Cold Spring Harbor Laboratory Press.

Nakayama, M., Nakajima, D., Nagase, T., Nomura, N., Seki, N., and Ohara, O. (1998). Identification of high-molecular-weight proteins with multiple EGF-like motifs by motif-trap screening. *Genomics*, *51*(1), 27–34.

Narayan, G., Goparaju, C., Arias-Pulido, H., Kaufmann, A. M., Schneider, A., Durst, M., Mansukhani, M., Pothuri, B., and Murty, V. V. (2006). Promoter hypermethylation-mediated inactivation of multiple Slit-Robo pathway genes in cervical cancer progression. *Mol Cancer*, *5*, 16.

Norman, J. T., Clark, I. M., and Garcia, P. L. (1999). Regulation of TIMP-1 expression by hypoxia in kidney fibroblasts. *Ann N Y Acad Sci*, *878*, 503–505.

Oft, M., Akhurst, R. J., and Balmain, A. (2002). Metastasis is driven by sequen-tial elevation of H-ras and Smad2 levels. *Nat Cell Biol*, *4*(7), 487–494.

Pelaia, G., Gallelli, L., D'Agostino, B., Vatrella, A., Cuda, G., Fratto, D., Renda, T., Galderisi, U., Piegari, E., Crimi, N., Rossi, F., Caputi, M., Costanzo, F. S., Vancheri, C., Maselli, R., and Marsico, S. A. (2007). Effects of TGF-beta and glucocorticoids on map kinase phosphorylation, IL-6/IL-11 secretion and cell proliferation in primary cultures of human lung fibroblasts. *J Cell Physiol*, *210*(2), 489–497.

Pelton, R. W., Saxena, B., Jones, M., Moses, H. L., and Gold, L. I. (1991). Immunohistochemical localization of TGF beta 1, TGF beta 2, and TGF beta 3 in the mouse embryo: expression patterns suggest multiple roles during embryonic development. *J Cell Biol*, *115*(4), 1091–1105.

Piper, M., Georgas, K., Yamada, T., and Little, M. (2000). Expression of the vertebrate Slit gene family and their putative receptors, the Robo genes, in the developing murine kidney. *Mech Dev*, *94*(1-2), 213–217.

Plump, A. S., Erskine, L., Sabatier, C., Brose, K., Epstein, C. J., Goodman, C. S., Mason, C. A., and Tessier-Lavigne, M. (2002). Slit1 and Slit2 cooperate to prevent premature midline crossing of retinal axons in the mouse visual system. *Neuron*, *33*(2), 219–232.

Qi, W., Chen, X., Poronnik, P., and Pollock, C. A. (2006). The renal cortical fibroblast in renal tubulointerstitial fibrosis. *Int J Biochem Cell Biol*, *38*(1), 1–5.

Qin, L., Tamasi, J., Raggatt, L., Li, X., Feyen, J. H. M., Lee, D. C., Dicicco-Bloom, E., and Partridge, N. C. (2005). Amphiregulin is a novel growth factor involved in normal bone development and in the cellular response to parathyroid hormone stimulation. *J Biol Chem*, *280*(5), 3974–3981.

Quaggin, S. E., and Kreidberg, J. A. (2008). Development of the renal glomerulus: good neighbors and good fences. *Development*, *135*(4), 609–620.

Ramirez-Solis, R., Davis, A. C., and Bradley, A. (1993). Gene targeting in embryonic stem cells. *Methods Enzymol*, *225*, 855–878.

Rekas, A., Alattia, J.-R., Nagai, T., Miyawaki, A., and Ikura, M. (2002). Crystal structure of venus, a yellow fluorescent protein with improved maturation and reduced environmental sensitivity. *J Biol Chem*, *277*(52), 50573–50578.

Reynisdottir, I., Polyak, K., Iavarone, A., and Massague, J. (1995). Kip/Cip and Ink4 Cdk inhibitors cooperate to induce cell cycle arrest in response to TGF-beta. *Genes Dev*, *9*(15), 1831–1845.

Roselli, S., Gribouval, O., Boute, N., Sich, M., Benessy, F., Attie, T., Gubler, M.-C., and Antignac, C. (2002). Podocin localizes in the kidney to the slit diaphragm area. *Am J Pathol*, *160*(1), 131–139.

Roselli, S., Heidet, L., Sich, M., Henger, A., Kretzler, M., Gubler, M.-C., and Antignac, C. (2004). Early glomerular filtration defect and severe renal disease in podocin-deficient mice. *Mol Cell Biol*, *24*(2), 550–560.

Rothberg, J. M., Hartley, D. A., Walther, Z., and Artavanis-Tsakonas, S. (1988). slit: an EGF-homologous locus of D. melanogaster involved in the development of the embryonic central nervous system. *Cell*, *55*(6), 1047–1059.

Sabatier, C., Plump, A. S., Brose, K., Tamada, A., Murakami, F., Lee, E. Y.-H. P., and Tessier-Lavigne, M. (2004). The divergent Robo family protein Rig-1/Robo3 is a negative regulator of slit responsiveness required for midline crossing by commissural axons. *Cell*, *117*(2), 157–169.

Saharinen, J., Hyytiainen, M., Taipale, J., and Keski-Oja, J. (1999). Latent transforming growth factor-beta binding proteins (LTBPs)–structural extracellular matrix proteins for targeting TGF-beta action. *Cytokine Growth Factor Rev*, *10*(2), 99–117.

Sanderson, N., Factor, V., Nagy, P., Kopp, J., Kondaiah, P., Wakefield, L., Roberts, A. B., Sporn, M. B., and Thorgeirsson, S. S. (1995). Hepatic expression of mature transforming growth factor beta 1 in transgenic mice results in multiple tissue lesions. *Proc Natl Acad Sci U S A*, *92*(7), 2572–2576.

Schlondorff, D. (1987). The glomerular mesangial cell: an expanding role for a specialized pericyte. *FASEB J*, *1*(4), 272–281.

Schwenk, F., Baron, U., and Rajewsky, K. (1995). A cre-transgenic mouse strain for the ubiquitous deletion of loxP-flanked gene segments including deletion in germ cells. *Nucleic Acids Res*, *23*(24), 5080–5081.

Shull, M. M., Ormsby, I., Kier, A. B., Pawlowski, S., Diebold, R. J., Yin, M., Allen, R., Sidman, C., Proetzel, G., and Calvin, D. (1992). Targeted disruption of the mouse transforming growth factor-beta 1 gene results in multifocal inflammatory disease. *Nature*, *359*(6397), 693–699.

Silberstein, G. B., Flanders, K. C., Roberts, A. B., and Daniel, C. W. (1992). Regulation of mammary morphogenesis: evidence for extracellular matrix-mediated inhibition of ductal budding by transforming growth factor-beta 1. *Dev Biol*, *152*(2), 354–362.

Sime, P. J., Xing, Z., Graham, F. L., Csaky, K. G., and Gauldie, J. (1997). Adenovector-mediated gene transfer of active transforming growth factor-beta1 induces prolonged severe fibrosis in rat lung. *J Clin Invest*, *100*(4), 768–776.

Snow, M. H., and Bennett, D. (1978). Gastrulation in the mouse: assessment of cell populations in the epiblast of tw18/tw18 embryos. *J Embryol Exp Morphol*, *47*, 39–52.

Strutz, F., Zeisberg, M., Renziehausen, A., Raschke, B., Becker, V., van Kooten, C., and Muller, G. (2001). TGF-beta 1 induces proliferation in human renal fibroblasts via induction of basic fibroblast growth factor (FGF-2). *Kidney Int*, *59*(2), 579–592.

Stuart, R. O., Bush, K. T., and Nigam, S. K. (2003). Changes in gene expression patterns in the ureteric bud and metanephric mesenchyme in models of kidney development. *Kidney Int*, *64*(6), 1997–2008.

Suvanto, P., Hiltunen, J. O., Arumae, U., Moshnyakov, M., Sariola, H., Sainio, K., and Saarma, M. (1996). Localization of glial cell line-derived neurotrophic factor (GDNF) mRNA in embryonic rat by in situ hybridization. *Eur J Neurosci*, *8*(4), 816–822.

Tang, Y., Wu, X., Lei, W., Pang, L., Wan, C., Shi, Z., Zhao, L., Nagy, T. R., Peng, X., Hu, J., Feng, X., Van Hul, W., Wan, M., and Cao, X. (2009). TGF-beta1-induced migration of bone mesenchymal stem cells couples bone resorption with formation. *Nat Med*, *15*(7), 757–765.

Thompson, N. L., Flanders, K. C., Smith, J. M., Ellingsworth, L. R., Roberts, A. B., and Sporn, M. B. (1989). Expression of transforming growth factor-beta 1 in specific cells and tissues of adult and neonatal mice. *J Cell Biol*, *108*(2), 661–669.

Torre-Amione, G., Beauchamp, R. D., Koeppen, H., Park, B. H., Schreiber, H., Moses, H. L., and Rowley, D. A. (1990). A highly immunogenic tumor transfected with a murine transforming growth factor type beta 1 cDNA escapes immune surveillance. *Proc Natl Acad Sci U S A*, *87*(4), 1486–1490.

Warming, S., Costantino, N., Court, D. L., Jenkins, N. A., and Copeland, N. G. (2005). Simple and highly efficient BAC recombineering using galK selection. *Nucleic Acids Res*, *33*(4), e36.

Wong, K., Ren, X. R., Huang, Y. Z., Xie, Y., Liu, G., Saito, H., Tang, H., Wen, L., Brady-Kalnay, S. M., Mei, L., Wu, J. Y., Xiong, W. C., and Rao, Y. (2001). Signal transduction in neuronal migration: roles of GTPase activating proteins and the small GTPase Cdc42 in the Slit-Robo pathway. *Cell*, *107*(2), 209–221.

Wu, J. Y., Feng, L., Park, H. T., Havlioglu, N., Wen, L., Tang, H., Bacon, K. B., and Rao, Y. (2001). The neuronal repellent Slit inhibits leukocyte chemotaxis induced by chemotactic factors. *Nature*, *410*(6831), 948–952.

Wyss-Coray, T., Feng, L., Masliah, E., Ruppe, M. D., Lee, H. S., Toggas, S. M., Rockenstein, E. M., and Mucke, L. (1995). Increased central nervous system production of extracellular matrix components and development of hydrocephalus in transgenic mice overexpressing transforming growth factor-beta 1. *Am J Pathol*, *147*(1), 53–67.

Yamanaka, N. (1988). Development of the glomerular mesangium. *Pediatr Nephrol*, *2*(1), 85–91.

Yaswen, L., Kulkarni, A. B., Fredrickson, T., Mittleman, B., Schiffman, R., Payne, S., Longenecker, G., Mozes, E., and Karlsson, S. (1996). Autoimmune manifestations in the transforming growth factor-beta 1 knockout mouse. *Blood*, *87*(4), 1439–1445.

Yiin, J., Hu, B., Jarzynka, M., Feng, H., Liu, K., Wu, J., Ma, H., and Cheng, S. (2009). Slit2 inhibits glioma cell invasion in the brain by suppression of Cdc42 activity. *Neuro Oncol*.

Yuan, W., Zhou, L., Chen, J. H., Wu, J. Y., Rao, Y., and Ornitz, D. M. (1999). The mouse SLIT family: secreted ligands for ROBO expressed in patterns that suggest a role in morphogenesis and axon guidance. *Dev Biol*, *212*(2), 290–306.

List of Figures

List of Tables

Appendices

List of primers

Primer	Sequence
109	GCTTTCAGTCACCACCCTCC
110	AGATGAGACCCAGCCCAGAG
274	TGGGAAGACAATAGCAGGCATGC
277	GACACGCTGAACTTGTGGCCG
278	GATCACATGGTCCTGCTGGAG
292	ATGTGGAATGTGTGCGAGGCCAG
326	GACCTGACTCACACGTTCTGGG
327	CACTGTGTCAGGTGGCACGTCTCG
379	GCGTTGGCAATTTAACCGCC
380	CAGTTTACCCGCTCTGCTAC
407	GACATTTAGGTGACACTATAG
408	TAATACGACTCACTATAAGGG
409	CAGAGGCAGGCGAATTTCTA
410	GGTGCCTCACACCTTGATTT
388	CACATGGCTGAATATCGACGG
442	GGCAACTTCTACAGCTCAGG
635	AGGTGGAGTTTGTGGTCTGG
638	ACCTGCCTCACATTTGTTCC
779	AGATTGGCTCCCAAGAATCA
780	GCCTCCTAGCAGGACTTGG
787	CAACCGCAAGATCGGAGT
788	TTTGCAGCTGCTTTGGAAG
795	CTTGCTGGGCATAAAGCAGT
796	GATAGAGAGGTGGGCTTGGA
801	CCATCATCCTCGCAGCTATT
802	TGTCGAAGCCTCCTTCTTTC
805	GCGTACTCTGAGCCCTGCT
806	TCACTCTCCAGTTTGCAAGG
809	GACCTCGACAAGTGCATGG
810	GGCCACAGTAGCCTGAAGTG
Gapdh5'	TCAAGAAGGTGGTGAAGCAG
Gapdh3'	ACCACCCTGTTGCTGTAGCC

Lists of cDNA microarray results

Upregulated genes in *Slitl2*-deficient thymi

List of genes that were upregulated in *Slitl2*-deficient thymi in comparison to wild-type controls with an adjusted P-value of < 0.001 and a fold change of ≥ 5. Annotated terms were derived from functional annotation clustering using the online available DAVID Bioinformatics Database (http://david.abcc.ncifcrf.gov/).
(1) Secreted
(2) Extracellular space

			Annotated terms	
Gene symbol	**Fold change**	**adj.*P*-value**	**1**	**2**
Gpx3	18.07	3.16E-008	x	x
8430408G22Rik	14.31	4.64E-006		
9930017A07Rik	12.43	1.12E-007		
Serpina3n	11.73	7.04E-04	x	x
BC011468	11.10	7.98E-007		
Spink3	9.64	1.48E-006	x	x
Lox	8.94	9.24E-007	x	x
Edn1	8.86	1.48E-006		
Igfbp5	8.27	1.02E-005		
Eppk1	8.07	3.89E-006		
Ctgf	7.58	2.06E-006	x	x
Gpr83	6.60	2.11E-006		x
Krt1-14	6.55	2.66E-006		
Foxq1	6.28	1.67E-006		
A2bp1	6.24	2.71E-006		
Zfp312	6.00	4.96E-006		
Cyp2a5	5.87	2.66E-006		
Slfn1	5.84	1.48E-006		
Krt1-23	5.78	5.06E-006		
Sftpd	5.75	2.86E-005	x	x
Ccl21a	5.72	6.00E-006		
Rgs4	5.55	2.95E-005		
Ccl21b	5.49	1.02E-005	x	x
Mglap	5.46	1.24E-04		
Rptn	5.39	1.72E-006	x	
Ltbp2	5.36	3.14E-007		
Guca2b	5.30	1.53E-005	x	x
Crp	5.24	7.57E-006	x	x
Cyp2f2	5.22	3.76E-006		x
Nupr1	5.20	1.72E-007		
Hspb1	5.19	3.38E-006		
Pdk4	5.15	3.80E-005		
Cldn11	5.13	4.01E-006		
Vwf	5.12	6.86E-006	x	x
Il7r	5.08	8.89E-006		
Fscn1	5.05	1.56E-006		
1190003J15Rik	5.01	1.72E-007		

Downregulated genes in *Slitl2*-deficient thymi

List of genes that were downregulated in *Slitl2*-deficient thymi in comparison to wild-type controls with an adjusted P-value of < 0.001 and a fold change of ≥ 5. Annotated terms were derived from functional annotation clustering using the online available DAVID Bioinformatics Database (http://david.abcc.ncifcrf.gov/).
(1) M phase
(2) Cytoskeleton
(3) Non-membrane bound organelle
(4) Microtubule
(5) Nucleus

			Annotated terms				
Gene symbol	**Fold change**	**adj.*P*-value**	**1**	**2**	**3**	**4**	**5**
Aqp11	17.00	1.10E-005					
Ppp1r1c	15.32	5.53E-006					
Dntt	12.65	1.12E-007					
Mns1	9.80	1.05E-005	x	x	x		x
0710001E13Rik	9.77	4.07E-006					
Cdc20	9.70	2.99E-005	x				
Birc5	9.58	1.20E-005	x	x	x	x	x
Top2a	8.39	9.19E-005			x		x
Rrm2	8.07	1.78E-005					
Lyt-2	7.78	1.78E-006					
Cdca7	7.74	1.43E-005					x
Pp11r	7.64	1.08E-04					
Chrna9	7.54	4.70E-005					
2810417H13Rik	7.47	6.81E-005					
Rag1	7.36	2.77E-006					x
Cdc2a	7.08	3.15E-005	x	x	x	x	x
Hist1h2ah	7.05	3.84E-04			x		x
Bub1b	6.89	2.24E-005					
E2f2	6.82	1.48E-006					x
Rorc	6.76	1.25E-005					x
Cdca3	6.72	2.30E-005	x				
Ccnb1	6.69	2.42E-006	x				x
G22p1	6.62	4.65E-006					
Plk1	6.30	1.21E-005	x	x	x		x
2410030K01Rik	6.18	2.02E-005					
BC028975	6.16	1.17E-006					
Brrn1	6.14	2.34E-005					
Ap3s1	6.13	1.42E-006					
Nusap1	6.01	2.56E-006	x	x	x	x	x
Sh2d1a	5.95	2.39E-006					
2610318C08Rik	5.94	1.43E-005					
1700022C02Rik	5.88	3.07E-006					
6720460F02Rik	5.83	5.53E-006					
Anln	5.83	4.90E-006	x	x	x		x
2610318N02Rik	5.79	3.35E-006					
Mki67	5.76	5.86E-006	x		x		x
Stk6	5.73	7.76E-006					
P2rx1	5.65	1.44E-005					
1110007A06Rik	5.62	4.65E-006					

			Annotated terms				
Gene symbol	**Fold change**	**adj.*P*-value**	**1**	**2**	**3**	**4**	**5**
Uhrf1	5.35	2.81E-006					x
Sgol2	5.35	1.45E-005			x		x
AI449441	5.33	4.75E-006					
Kif2c	5.32	5.41E-006		x	x	x	x
Tube1	5.26	3.75E-006		x	x	x	
3000004C01Rik	5.18	1.05E-005		x	x	x	
Clspn	5.17	4.14E-006			x		x
Cd8b	5.17	9.24E-007					
2510015F01Rik	5.15	2.97E-006					
Kif22	5.12	3.24E-006		x	x	x	x
Hist1h3b	5.07	8.28E-006					
Kif4	5.06	1.66E-005		x	x	x	x

Upregulated genes in *Slitl2*-deficient spleens

List of genes that were upregulated in *Slitl2*-deficient spleens in comparison to wild-type controls with an adjusted P-value of < 0.01 and a fold change of ≥ 2. No annotated terms were derived from functional annotation clustering using the online available DAVID Bioinformatics Database (http://david.abcc.ncifcrf.gov/).

Gene symbol	**Fold change**	**adj.*P*-value**
Pdk4	5.37	5.33E-03
Edn1	5.28	1.66E-03
Mglap	4.82	4.44E-03
Gpx3	4.43	4.48E-03
Fkbp5	4.07	4.48E-03
Lox	4.00	6.73E-03
Ctgf	3.89	4.48E-03
1300002F13Rik	3.68	9.49E-03
Cygb	3.08	2.99E-03
Fosl2	3.03	5.59E-03
Fbln2	2.88	9.89E-03
Pex11a	2.82	2.99E-03
Ptpn8	2.77	6.38E-03
Lims2	2.75	8.77E-03
Map3k6	2.74	8.01E-03
Dkk3	2.72	5.34E-03
Cdkn1c	2.70	4.48E-03
Hmox1	2.68	4.04E-03
Cd14	2.68	7.05E-03
Pkp4	2.67	5.34E-03
Grasp	2.65	5.33E-03
Itih3	2.61	7.31E-03
Sema3f	2.59	8.66E-03
Sult1a1	2.57	8.51E-03
Thsd1	2.54	8.51E-03
1500004A08Rik	2.53	8.15E-03
Gata2	2.48	8.23E-03

Gene symbol	Fold change	adj.*P*-value
CRG-L1	2.45	9.64E-03
Cyp26b1	2.45	4.04E-03
Sox17	2.45	3.84E-03
Pald	2.40	9.87E-03
BC011468	2.38	7.31E-03
Plat	2.36	4.64E-03
Fbxo32	2.35	6.90E-03
Rapgef5	2.35	6.90E-03
Fcgr3	2.32	4.44E-03
Esam1	2.29	9.71E-03
Centa2	2.28	4.64E-03
Pdlim4	2.27	5.97E-03
Flt1	2.27	4.44E-03
Aebp1	2.26	5.97E-03
Neurl	2.25	7.36E-03
Sema6b	2.25	5.11E-03
Cirbp	2.25	3.84E-03
BC004728	2.22	3.84E-03
Mmp14	2.21	8.77E-03
Il11ra2	2.21	8.78E-03
Epn2	2.20	3.84E-03
Nfic	2.19	4.64E-03
Itm2c	2.16	3.84E-03
Cdkn1a	2.15	7.97E-03
Rgs1	2.14	4.64E-03
Gas6	2.14	5.33E-03
Fcrl3	2.13	5.59E-03
Il11ra1	2.12	6.93E-03
Lzts2	2.12	9.11E-03
Rora	2.11	6.76E-03
Mcam	2.11	9.87E-03
Ror2	2.09	7.44E-03
Pla2g7	2.09	5.09E-03
Ng23	2.08	6.99E-03
Ccl9	2.08	5.16E-03
Hap1	2.07	8.77E-03
Tef	2.07	5.11E-03
Scarf2	2.07	5.33E-03
Slc6a8	2.06	6.03E-03
Ankrd2	2.06	7.05E-03
4930486L24Rik	2.06	8.78E-03
Sgk	2.05	5.37E-03
B930041F14Rik	2.05	4.64E-03
AA960558	2.03	8.81E-03
Gstm1	2.03	8.01E-03
Bmf	2.03	4.64E-03
Amotl1	2.02	5.97E-03
Adam15	2.02	9.71E-03
Hmgcs2	2.02	7.20E-03
Pld1	2.02	5.70E-03
Bmp4	2.01	6.90E-03

Downregulated genes in *Slitl2*-deficient spleens

List of genes that were downregulated in *Slitl2*-deficient spleens in comparison to wild-type controls with an adjusted P-value of < 0.01 and a fold change of ≥ 2. Annotated terms were derived from functional annotation clustering using the online available DAVID Bioinformatics Database (http://david.abcc.ncifcrf.gov/).
(1) Intracellular
(2) Metabolic process
(3) Mitosis

			Annotated terms		
Gene symbol	**Fold change**	**adj.*P*-value**	**1**	**2**	**3**
Pdip	6.76	8.77E-03			
Slitl2	5.23	6.44E-06			
Rrm2	4.45	8.91E-03	x	x	
Uros	4.44	8.45E-03		x	
Kntc1	4.04	6.20E-03	x		x
1190007F08Rik	4.02	7.06E-03			
Ccne1	3.91	5.06E-03	x	x	
Cdc6	3.66	7.77E-03	x	x	x
Arrb1	3.53	8.72E-03	x		
Fignl1	3.53	6.52E-03			
Ptdss2	3.45	9.87E-03	x	x	
Clspn	3.39	6.90E-03	x	x	
Sec14l2	3.24	3.84E-03	x	x	
Stk6	3.13	8.97E-03			
Tpx2	3.12	7.31E-03	x		
Rad54l	3.11	4.75E-03	x	x	
1110007C05Rik	3.09	5.37E-03			
Mcm2	3.02	5.37E-03	x	x	
Solt	2.99	5.93E-03			
Uhrf1	2.97	5.11E-03	x	x	
Ccrn4l	2.94	9.12E-03			
Tcf19	2.90	5.16E-03	x	x	
Mcm10	2.90	5.59E-03	x	x	
Hist1h2bm	2.88	9.20E-03	x	x	
Ifrd2	2.84	8.01E-03			
E2f1	2.84	8.44E-03	x	x	
Rgs12	2.84	4.64E-03			
Pfkm	2.83	9.42E-03	x	x	
Chtf18	2.81	3.84E-03			
Rfc4	2.77	5.34E-03	x	x	
Rrm1	2.77	8.31E-03	x	x	
Dusp8	2.74	8.39E-03	x	x	
Mcm5	2.73	6.87E-03	x	x	
2810418N01Rik	2.71	7.07E-03			
Ubadc1	2.69	6.35E-03			
Chaf1a	2.69	4.64E-03	x	x	
AI256775	2.66	4.64E-03			
2610318C08Rik	2.64	7.72E-03			
Hist1h3i	2.60	9.32E-03	x	x	
Recql4	2.57	5.33E-03	x	x	
Lig1	2.56	4.44E-03	x	x	

			Annotated terms		
Gene symbol	**Fold change**	**adj.*P*-value**	**1**	**2**	**3**
Minpp1	2.56	8.35E-03	x		
Cldn13	2.55	8.39E-03			
Chaf1b	2.54	8.77E-03	x	x	
Ammecr1	2.53	6.99E-03			
Psmc3ip	2.51	6.74E-03	x		
Arhgdig	2.49	9.64E-03	x		
4930547N16Rik	2.49	6.99E-03	x		
Dutp	2.48	3.84E-03			
Mcm7	2.48	7.97E-03	x	x	
Cenph	2.48	3.84E-03	x		x
Pcyt1b	2.46	8.35E-03	x	x	
Scoc	2.44	4.44E-03			
1110025F24Rik	2.42	7.04E-03			
Cdca5	2.40	8.01E-03	x		x
Mcm3	2.39	6.75E-03	x	x	
Xkh	2.39	8.57E-03			
Calmbp1	2.38	7.00E-03			
Siah1b	2.38	8.53E-03	x	x	
Hist2h3b	2.37	8.51E-03			
Foxm1	2.35	5.16E-03	x	x	
Fen1	2.33	7.04E-03	x	x	
Pbk	2.33	4.48E-03		x	
2410004L22Rik	2.33	2.99E-03			
Orc6l	2.32	9.32E-03	x	x	
Mcm4	2.29	4.48E-03	x	x	
Pole3	2.27	7.07E-03	x		
Hrbl	2.26	3.84E-03			
Sqle	2.24	9.87E-03	x	x	
Mthfd2	2.23	7.04E-03	x	x	
4430402O11Rik	2.22	4.48E-03			
E130016E03Rik	2.21	4.44E-03	x	x	
LOC432879	2.19	6.03E-03			
Traf4	2.19	4.44E-03	x		
2600005O03Rik	2.18	2.99E-03			
Fancd2	2.18	7.46E-03	x	x	
6330503K22Rik	2.16	9.58E-03	x		
2810027O19Rik	2.16	7.72E-03			
Tmem14c	2.16	4.44E-03	x		
2610019I03Rik	2.15	6.87E-03			
2610510J17Rik	2.15	7.04E-03			
5830426I05Rik	2.14	5.09E-03			
2700029M09Rik	2.13	5.11E-03			
Cdc25a	2.12	4.48E-03	x	x	x
Hist1h1a	2.12	5.34E-03	x	x	
4930542G03Rik	2.12	6.48E-03			
Incenp	2.11	9.04E-03	x		x
Plk4	2.08	6.07E-03		x	
1110004B13Rik	2.07	4.44E-03			
BC028450	2.07	9.94E-03			
Rpa3	2.05	8.23E-03	x	x	
Mylpf	2.05	8.39E-03	x		

			Annotated terms		
Gene symbol	**Fold change**	**adj.*P*-value**	**1**	**2**	**3**
4930430F08Rik	2.05	6.90E-03			
Brip1	2.04	4.44E-03	x	x	
F730047E07Rik	2.04	4.44E-03			
Cdca2	2.03	7.20E-03	x		x
Sfrs7	2.02	4.64E-03	x	x	
A430005L14Rik	2.02	4.44E-03			
Nme3	2.00	4.48E-03		x	
Csda	2.00	5.09E-03	x	x	
2600001J17Rik	2.00	8.01E-03			

Upregulated genes in *Slitl2*-deficient kidneys

List of genes that were upregulated in *Slitl2*-deficient kidneys in comparison to wild-type controls with an adjusted P-value of < 0.01 and a fold change of > 1.86. Annotated terms were derived from functional annotation clustering using the online available DAVID Bioinformatics Database (http://david.abcc.ncifcrf.gov/).
(1) MHC class II antigen presentation
(2) Inflammatory response

			Annotated terms	
Gene symbol	**Fold change**	**adj.*P*-value**	**1**	**2**
Havcr1	13.38	9.84E-06		
C3	10.84	1.96E-03		x
Cxcl1	4.72	6.91E-04		x
Ccl5	4.40	5.08E-04		x
Krt20	3.55	3.14E-03		
Timp1	3.29	3.44E-03		
Abp1	3.08	5.08E-04		
H2-Aa	2.89	9.13E-03	x	
H2-Eb1	2.86	2.76E-03	x	
LOC641240	2.75	6.49E-04		
H2-Ab1	2.70	5.08E-04	x	
Cd74	2.69	3.04E-03	x	x
Egr2	2.59	5.08E-04		
Cxcl10	2.57	1.55E-03		x
Socs3	2.44	1.96E-03		
Tlr2	2.40	1.55E-03		x
Tnfrsf12a	2.32	2.67E-03		
Trib3	1.88	9.13E-03		
Areg	1.87	5.65E-03		

List of suppliers

Ambion	*part of Invitrogen*
Amersham	*part of GE Healthcare*
Applied Biosystems	*part of Invitrogen*
Baxter Deutschland GmbH	Unterschleißheim, Germany
BD Biosciences	Heidelberg, Germany
Binder GmbH	Tuttlingen, Germany
Bio-Rad Laboratories GmbH	Munich, Germany
Chemicon	*part of Millipore*
Clontech Europe	*part of BD Biosciences*
Corning Life Sciences	Amsterdam, The Netherlands
Eppendorf AG	Hamburg, Germany
Fermentas GmbH	St. Leon-Rot, Germany
Fluka Chemie GmbH	*part of Sigma-Aldrich*
GE Healthcare Europe GmbH	Freiburg, Germany
Gibco	*part of Invitrogen*
Greiner Bio-One	Frickenhausen, Germany
Hamilton Thorne, Inc.	Beverly, MA, USA
Heraeus	*part of Thermo Scientific*
IBL International GmbH	Hamburg, Germany
IKA Werke GmbH	Staufen, Germany
Implen GmbH	Munich, Germany
Invitrogen GmbH	Karlsruhe, Germany
Jackson ImmunoResearch Europe Ltd.	Newmarket, UK
KABE Labortechnik GmbH	Nümbrecht-Elsenroth, Germany
Leica Microsystems GmbH	Wetzlar, Germany
Menzel Gläser	*part of Thermo Scientific*
Merck KGaA	Darmstadt, Germany
Microm GmbH	Walldorf, Germany
Millipore GmbH	Schwalbach, Germany
Miltenyi Biotec GmbH	Bergisch Gladbach, Germany
MJ Research	*part of Thermo Scientific*
MWG (Eurofins MWG Operon)	Ebersberg, Germany
NEB (New England Biolabs GmbH)	Frankfurt/Main, Germany
Peqlab GmbH	Erlangen, Germany
Perkin Elmer LAS GmbH	Rodgau-Jügesheim, Germany
Polysciences Europe GmbH	Eppelheim, Germany
Promega GmbH	Mannheim, Germany
Qiagen GmbH	Hilden, Germany
Roche Diagnostics GmbH	Mannheim, Germany
Roth GmbH	Karlsruhe, Germany
Schleicher&Schuell GmbH	Dassel, Germany
SERVA Electrophoresis GmbH	Heidelberg, Germany
Sigma-Aldrich Biochemie GmbH	Steinheim, Germany
Stratagene Europe	Amsterdam, The Netherlands
Thermo Scientific	Karlsruhe, Germany
Tree Star, Inc.	Ashland, OR, USA
Vector Laboratories Ltd.	Peterborough, UK
Zeiss AG	Oberkochen, Germany

Presentations

Parts of this thesis have been presented previously as posters.

'Slit-like 2 (*Slitl2*)-deficient mice show
growth retardation and involuted thymi and spleens.'
Mayer M., Schrewe H.
XX International Congress of Genetics,
Berlin, Germany (July 12-17, 2008)

'Functional analysis on the role of Slit-like 2 (*Slitl2*) in the mouse.'
Michaela Mayer, Heinrich Schrewe
18th Scientific Meeting of the German Society for Developmental Biology,
Hannover, Germany (March 25-28, 2009)

Acknowledgments

First and foremost, I thank Dr. Heinrich Schrewe for his open mind and for introducing me to the exciting field of genetic research. I want to thank Prof. Achim Gruber from the Institute of Veterinary Pathology for serving as my doctoral advisor at the Freie Universität Berlin. I thank Prof. Bernhard Herrmann from the Max Planck Institute for Molecular Genetics for supporting me as a Ph.D. student in his department.

Many thanks to the members of the Schrewe lab: Manuela Scholze, an outstanding technician, who taught me so much, Bärbel Kosiol for her endless efforts concerning the expression analysis, and my colleague Pedro Rocha for sharing his knowledge. I want to thank all the members of the Department of Developmental Genetics, especially – in alphabetical order – Dr. Phillip Grote, Karol Macura, Dr. Markus Morkel, Dr. Ralf Spörle, and Dr. Martin Werber.

This work would not have been possible without the help of so many dedicated people at the Max Planck Institute. I thank Dr. Ludger Hartmann from the Animal Facility and his team, in particular Sonja Banko, Mirjam Peetz, Kristin Schulze, and Ingo Voigt. I also want to thank Beatrix Fauler from the Microscopy Unit and Katrin Ullrich from the Photo Unit.

I want to express my gratitude to our collaborators for combining their efforts with our own. I thank Dr. Marc Ehlers and Susanne Eiglmeier from the Laboratory of Tolerance and Autoimmunity at the DRFZ Berlin as well as Prof. Hermann-Josef Gröne and Dr. Zoran Popovic from the DKFZ in Heidelberg. I would like to thank Prof. Hans van Leuuwen and especially Dr. Marco Eijken from the Erasmus Medical Center in Rotterdam.

Last but not least, I thank my families (sic) and my friends, because all is nothing without them.

Candidate's declaration

Selbständigkeitserklärung

Hiermit bestätige ich, dass ich die vorliegende Arbeit selbständig angefertigt habe. Ich versichere, dass ich ausschließlich die angegebenen Quellen und Hilfen in Anspruch genommen habe.

Berlin, den 16. Oktober 2009

Michaela Mayer